Supplementary Materials for

Differential Diffusivity of Nodal and Lefty Underlies a Reaction-Diffusion Patterning System

Patrick Müller*, Katherine W. Rogers, Ben M. Jordan, Joon S. Lee,
Drew Robson, Sharad Ramanathan and Alexander F. Schier*

*To whom correspondence should be addressed. pmueller@fas.harvard.edu (P.M.),
schier@fas.harvard.edu (A.F.S.)

This PDF file includes:

Text S1 to S8
Tables S1 to S8
Figs. S1 to S26
Caption for Movie S1

Other Supplementary Material for this manuscript includes the following:

Movie S1

Supplementary Materials for "Differential Diffusivity of Nodal and Lefty Underlies a Reaction-Diffusion Patterning System"

Patrick Müller[1,†], Katherine W. Rogers[1], Ben M. Jordan[2,*], Joon S. Lee[1,*], Drew Robson[1], Sharad Ramanathan[3] and Alexander F. Schier[1,3,†]

[1]Department of Molecular and Cellular Biology, Harvard University, Cambridge, USA
[2]Department of Organismic and Evolutionary Biology, Harvard University, Cambridge, USA
[3]FAS Center for Systems Biology and Harvard Stem Cell Institute, Harvard University, Cambridge, USA
[*]These authors contributed equally to this work
[†]To whom correspondence should be addressed. E-mail: pmueller@fas.harvard.edu (P.M.) schier@fas.harvard.edu (A.F.S.)

Our study measures the distribution, diffusivity and clearance kinetics of the two Nodal signals Squint and Cyclops and the two Lefty proteins Lefty1 and Lefty2 in living zebrafish embryos. This supplementary document is divided into eight sections and contains detailed methods and discussions regarding 1) the influence of clearance and diffusion on pattern formation in reaction-diffusion systems, 2) Nodal and Lefty as a reaction-diffusion patterning system, 3) the generation and characterization of active fusion proteins, 4) measurements of distribution profiles, 5) measurements of clearance rate constants, 6) measurements of effective diffusion coefficients, 7) modeling of gradient formation, and 8) comparison of the Nodal/Lefty system to other reaction-diffusion systems.

Contents

1 Influence of Clearance and Diffusion on Pattern Formation in Reaction-Diffusion Systems 3

2 Nodal and Lefty as a Reaction-Diffusion Patterning System 8

3 Generation and Characterization of Fluorescent Nodal and Lefty Proteins 10
3.1 Rationale and summary . . . 10
3.2 Cloning of fusion constructs . . . 10
3.3 mRNA synthesis, embryo injections and *in situ* hybridization . . . 11
3.4 Preparation of extracellular protein fractions for western blots . . . 12
3.5 Analysis of fusion protein activity . . . 13
3.6 Analysis of fusion protein activity range . . . 14
3.7 Assessment of fusion proteins . . . 14

4 Measurement of Distribution Profiles 16
4.1 Rationale and summary . . . 16
4.2 Experimental setup . . . 16
4.3 Image analysis . . . 17

5 Measurement of Clearance Rate Constants 18
5.1 Rationale and summary . . . 18
5.2 Experimental setup . . . 18
5.3 Image analysis . . . 19
5.4 Data fitting . . . 20
5.5 Statistical tests . . . 22
5.6 Controls for clearance assay . . . 22

6 Measurement of Effective Diffusion Coefficients 24
6.1 Rationale and summary . . . 24
6.2 Experimental setup . . . 24
6.3 Image analysis . . . 25
6.4 Mathematical modeling of FRAP experiments . . . 25
6.5 Potential mechanisms underlying differential effective diffusivity . . . 35

7 Modeling of the Distribution Profiles 38
7.1 Rationale and summary . . . 38
7.2 Mathematical modeling . . . 38
7.3 Data fitting . . . 39

8 Comparison of the Nodal/Lefty System to Other Reaction-Diffusion Systems 41

9 List of Frequently Used Abbreviations and Variables 44

1 Influence of Clearance and Diffusion on Pattern Formation in Reaction-Diffusion Systems

Summary

Classical reaction-diffusion models postulate that spatial patterning can be mediated by short-range activators and long-range inhibitors. One of the central tenets of reaction-diffusion models is that pattern formation depends critically on the relative diffusivities of the activator and inhibitor: the activator must be several fold less diffusive than the inhibitor for patterning to occur. Here, we illustrate the contributions of diffusivity and clearance on pattern formation using the Meinhardt-Gierer activator/inhibitor system as an example. Differential diffusivity, not clearance, of activator and inhibitor is absolutely required for pattern formation to occur, but both diffusion and clearance can influence the probability of patterning.

Reaction-diffusion models describe how chemical reactions and dispersal by diffusion lead to spatial and temporal concentration changes (*1-3, 31*). The ability of a reaction-diffusion system to generate a spatial pattern depends on the parameter values of the system. These parameters include activator and inhibitor diffusion coefficients, clearance rates, cross-reaction kinetics, a measure of the geometry, as well as initial and boundary conditions (*32, 33*). Murray stated that " [...] *it is the orchestration of several effects which produce pattern, not just one, since we can move into the pattern formation regime by varying one of several parameters. Clearly we can arrive at a specific point in the space by one of several paths. The concept of equivalent effects, via parameter variation, producing the same pattern is an important one in the interpretation and design of relevant experiments associated with any model. It is not a widely appreciated concept in biology.*" (*32*). In particular, it has been demonstrated that the values of the diffusion coefficients and clearance rate coefficients both strongly affect the ability of a reaction-diffusion system to generate patterns (*27, 34, 35*).

The general two-component reaction-diffusion system is described by

$$\frac{\partial U}{\partial t} = D_U \nabla^2 U + F(U,V) \tag{1}$$

$$\frac{\partial V}{\partial t} = D_V \nabla^2 V + G(U,V) \tag{2}$$

Several biologically reasonable reaction systems have been considered, including the Schnakenberg (*36*), Thomas (*37*) and Meinhardt-Gierer (*2, 27, 34*) systems. Here, we consider the classical Meinhardt-Gierer activator/inhibitor system. Note that this is one of many reaction-diffusion systems (e.g. (*8, 16, 28-30, 38*)), and the domains in parameter space in which patterns are obtained depend on the equations that describe the reactions. However, all systems absolutely require differential diffusivity of activator and inhibitor for pattern formation, as demonstrated below. The reactions in the classical Meinhardt-Gierer system are described by the equations

$$F(U,V) = \rho_U \frac{U^2}{V} - k_U U + \sigma_U \tag{3}$$

$$G(U,V) = \rho_V U^2 - k_V V \tag{4}$$

where k_U and k_V are the clearance rate coefficients and ρ_U and ρ_V are the cross-reaction coefficients of the activator U and the inhibitor V. σ_U is a constant production term for the activator.

In order to determine which conditions lead to patterns, we consider the one-dimensional system with no-flux boundary conditions and some initial conditions. We non-dimensionalize the system following the analysis by Koch and Meinhardt (*34*). By forming dimensionless groups, we define the new dimensionless variables:

$$\begin{aligned}
\tilde{t} &= k_U t \\
u &= \frac{k_U \rho_V}{k_V \rho_U} U \\
v &= \frac{k_U^2 \rho_V}{k_V \rho_U^2} V \\
\tilde{l} &= \sqrt{(k_U/D_V)} l
\end{aligned}$$

Substituting these into the original equations gives the dimensionless form of the system

$$\begin{aligned}
\frac{\partial u}{\partial \tilde{t}} &= D\tilde{\nabla}^2 u + f(u,v) \\
\frac{\partial v}{\partial \tilde{t}} &= \tilde{\nabla}^2 v + g(u,v)
\end{aligned}$$

where

$$f(u,v) = \frac{u^2}{v} - u + \sigma \tag{5}$$

$$g(u,v) = k(u^2 - v) \tag{6}$$

with $D = \frac{D_U}{D_V}$, $k = \frac{k_V}{k_U}$, $\sigma = \frac{\rho_V \sigma_U}{k_V \rho_U}$, and $\tilde{\nabla}^2 = \frac{\partial^2}{\partial \tilde{x}^2}$.

If we ignore diffusion and only consider the reactions, the system reaches a steady state with uniform concentrations of the two species. The system has a single steady state (u_0, v_0) at

$$\begin{aligned}
u_0 &= 1 + \sigma \\
v_0 &= (1+\sigma)^2 = u_0^2
\end{aligned}$$

To determine its stability, we linearize the system about the steady state. The steady state is stable when the real part of the eigenvalues λ of the linearized system is less than zero, i.e. $Re(\lambda) < 0$. Given the form of the characteristic polynomial of the system and the requirement that it be equal to zero

$$\lambda^2 - (f_u + g_v)\lambda + (f_u g_v - f_v g_u) = 0$$

the steady state is guaranteed to be stable when

$$tr(\mathbf{J}) = f_u + g_v \quad < 0 \tag{7}$$

$$det(\mathbf{J}) = f_u g_v - f_v g_u \quad > 0 \tag{8}$$

where the Jacobian is

$$\mathbf{J} = \begin{bmatrix} \frac{\partial f}{\partial u} & \frac{\partial f}{\partial v} \\ \frac{\partial g}{\partial u} & \frac{\partial g}{\partial v} \end{bmatrix} = \begin{bmatrix} f_u & f_v \\ g_u & g_v \end{bmatrix}$$

For our choice of reaction system in Equations 5 and 6, the components of the Jacobian are

$$\begin{aligned} f_u &= \frac{2u}{v} - 1 \\ f_v &= -\frac{u^2}{v^2} \\ g_u &= 2ku \\ g_v &= -k \end{aligned}$$

and the stability conditions from Equations 7 and 8 become

$$\begin{aligned} tr(\mathbf{J}) &= \frac{2u}{v} - k - 1 && < 0 \\ det(\mathbf{J}) &= \frac{k(-2vu + v^2 + 2u^3)}{v^2} && > 0 \end{aligned}$$

Turing demonstrated that spatially inhomogenous patterns can arise from diffusion-driven instabilities (*1*). The conditions which give rise to these instabilities are determined by considering the full linearized reaction-diffusion system. For the reactions only, we determined the stability of the system when $Re(\lambda) < 0$. For spatial patterns caused by diffusive instabilities, we need to find $Re(\lambda) > 0$ for the full system. Here, $\lambda = \lambda(q)$, where q is any of the wavenumbers of the eigenfunctions on the domain, implying that certain modes can drive diffusive instabilities. The modes that do so are found by computing when the determinant of the linearized system is equal to zero. Given the requirement on the characteristic polynomial of the system

$$\lambda(q)^2 + \lambda(q)[q^2(1+D) - f_u - g_v] + [Dq^4 - (f_u + Dg_v)q^2 + f_u g_v - f_v g_u] = 0$$

instabilities arise if either of the following conditions are true:

$$\begin{aligned} q^2(1+D) - f_u - g_v &< 0 \\ h(q^2) = Dq^4 - (f_u + Dg_v)q^2 + f_u g_v - f_v g_u &< 0 \end{aligned}$$

where $q \neq 0$. Given Equations 7 and 8 and the positive values of D and q, the first of these two conditions cannot be satisified. Thus, the only way that $Re(\lambda(q)) > 0$ for some q is if the second of these conditions is satisfied, which is only possible if

$$f_u + Dg_v > 0 \tag{9}$$

In conjunction with Equation 7, it follows that is necessary that $D < 1$ for this to be satisfied. Thus, the diffusivity D_V of the inhibitor must be greater than the diffusivity D_U of the activator. This difference in activator and inhibitor diffusivities is a necessary but not sufficient condition

for pattern formation; in addition, the minimum of $h(q^2)$ must be negative. This minimum is obtained by differentiating $h(q^2)$ and setting it equal to zero. Solving for q^2, we find that

$$q^2 = \frac{f_u + Dg_v}{2D}$$

which substituted into the original expression for $h(q^2)$ gives the minimum h at

$$f_u g_v - f_v g_u - \frac{(f_u + Dg_v)^2}{4D}$$

For the above minimum of h to be negative

$$f_u g_v - f_v g_u < \frac{(f_u + Dg_v)^2}{4D} \tag{10}$$

In summary, from Equations 7, 8, 9 and 10, the four conditions that have to be fulfilled by a reaction-diffusion system to give rise to patterns are thus (*32*):

$$f_u + g_v < 0 \tag{11}$$

$$f_u g_v - f_v g_u > 0 \tag{12}$$

$$f_u + Dg_v > 0 \tag{13}$$

$$\frac{(f_u + Dg_v)^2}{4D} - (f_u g_v - f_v g_u) > 0 \tag{14}$$

Written in terms of the dimensionless Meinhardt-Gierer system that we consider, we have

$$\frac{2u}{v} - 1 - k < 0$$

$$\frac{k(-2uv + v^2 + 2u^3)}{v^2} > 0$$

$$\frac{2u - v}{Dv} - k > 0$$

$$\left(\frac{2u - v}{Dv} - k\right)^2 - \frac{4k(-2uv + v^2 + 2u^3)}{Dv^2} > 0$$

Evaluated at the steady state (u_0, v_0), these conditions become

$$\frac{2}{1+\sigma} - k - 1 < 0 \tag{15}$$

$$k > 0 \tag{16}$$

$$\frac{2 - (1+\sigma)}{D(1+\sigma)} - k > 0 \tag{17}$$

$$\left(\frac{2 - (1+\sigma)}{D(1+\sigma)} - k\right)^2 - \frac{4k}{D} > 0 \tag{18}$$

Pattern formation can occur for values of the parameters D, k and σ that satisfy the above conditions. Using the dimensionless groups defined above, D is the ratio of the diffusion coefficients and k is the ratio of the clearance rate constants, whereas σ is a more complicated ratio

involving the cross-reaction kinetics, the production of the activator, and the degradation of the inhibitor. Given the complexity of σ and the unknown values of the quantities it involves, we chose to explore the pattern forming capacity of D and k over reasonable ranges of values. To do so, we tested the above four conditions (Equations 15, 16, 17 and 18) over a linearly spaced sampling of floating point values of parameter space of D, k, and σ. The positive (=1) or negative (=0) outcome of the testing of these conditions at each value triplet was averaged over all values of σ, and projected into a two dimensional representation of parameter space, interpreted as a probability of pattern forming capacity of the system (fig. S1). Importantly, patterns in this system cannot be formed with equal diffusivities of activator and inhibitor; the inhibitor must be at least ∼6-fold more diffusive than the activator. As the ratio of D decreases, the probability that a system is capable of pattern formation increases. This probability also increases as the ratio of k approaches unity (assuming $D \lesssim 0.2$). Interestingly, even a system with a very low D value may not form a Turing pattern if the value of k is very high or very low.

In conclusion, the ability of a reaction-diffusion system to form patterns is absolutely dependent on an inhibitor that is more diffusive than the activator, but both diffusion and clearance can influence the probability of patterning. To test the central tenet of reaction-diffusion models postulating differential diffusivity, we measured both the diffusion coefficients of the activator and inhibitor as well as the clearance rate constants. We found that the inhibitor Lefty has a much higher diffusion coefficient than the activator Nodal, whereas clearance is similar for both activator and inhibitor. Our findings therefore experimentally support the mathematical predictions of reaction-diffusion models of pattern formation.

2 Nodal and Lefty as a Reaction-Diffusion Patterning System

Summary

Reaction-diffusion systems involving auto-regulatory short-range activators and activator-induced long-range inhibitors can generate patterns ranging from simple gradients to stripes and spots depending on initial conditions, parameter values and boundary conditions (*2, 3, 39*). In this section, we describe the previously identified properties of the Nodal/Lefty system that have led to its designation as a reaction-diffusion patterning system (*3-6, 19, 20, 22, 40, 41*).

Studies of the Nodal/Lefty system have provided genetic evidence for a reaction-diffusion patterning system: Nodal is a short- to mid-range activator that enhances both its own expression and that of the long-range inhibitor Lefty (*3-6, 19, 20, 22, 40, 41*). Even though the biophysical properties of the Nodal/Lefty system have not been explored, numerous studies and reviews consider Nodal/Lefty a reaction-diffusion patterning system (*3-6, 18-20, 22, 24, 40-58*). For example, Meinhardt has highlighted the Nodal/Lefty system as one of the first biological examples of an activator/inhibitor reaction-diffusion system (*4*), Kondo and Miura have stated that the Nodal/Lefty interaction "[...] *indicates that this system fulfills the fundamental requirements for Turing pattern formation* [...]" (*3*), Hamada and colleagues used reaction-diffusion models to simulate left-right patterning by Nodal/Lefty (*16*), and Horsthemke has stated that "*Nodal and Lefty fulfill Turing's requirement of local self-activation and long-range inhibition.*" (*31*).

Closer analysis of the Nodal/Lefty reaction-diffusion patterning system in developmental contexts shows that it is influenced by additional constraints: Nodal and Lefty expression is biased by prepatterns, and the tissue response is restricted by size and time scales. These constraints likely allow the generation of highly reproducible patterns during embryogenesis rather than the complex *de novo* self-organizing patterns found in some other incarnations of the reaction-diffusion model. For example, during germ-layer formation, Nodal signals act as short- to mid-range inducers of endodermal and mesodermal fates, whereas Lefty signals act as long-range antagonists to prevent Nodal signaling and promote ectoderm formation at a distance. The zebrafish Nodal signals Cyclops (short-range) and Squint (mid-range) are expressed at the blastula margin and induce mesendodermal target genes (*19, 23*). At the blastula margin, Nodal signals also induce their own expression as well as the expression of Lefty1 and Lefty2 (*6*). Lefty signals inhibit mesendoderm induction by blocking Nodal signaling (*59, 60*) (Fig. 1A). Loss of Nodal signaling leads to the transformation of mesendodermal progenitors into ectodermal progenitors, whereas loss of Lefty leads to the transformation of presumptive ectoderm into mesendoderm (*19, 61, 62*). Although Nodal and Lefty display local self-activation and long-range inhibition in this context, the reaction-diffusion system is constrained by maternal transcription factors that activate Nodal expression at the blastula margin (*63*), by the short time period during which cell fates can be allocated (cells only respond to Nodal signaling for a few hours (*64*)), and the short length scale of the embryo ($\sim$500 µm) compared to the range of the signals ($\sim$150 µm) (*19, 23, 65-68*). The regulatory and inductive interactions of Nodal and Lefty can be recapitulated at the animal pole of zebrafish embryos. Clones expressing Nodals and Leftys at the animal pole recapitulate the major aspects of patterning induced by endoge-

nous sources: High- and low-threshold target genes are induced in and around Nodal-expressing clones (*23*), the different ranges of Cyclops, Squint and Lefty proteins are maintained (*6, 23*), cell internalization associated with gastrulation can be induced (*69, 70*), and cross-regulation of Nodals and Leftys is preserved (*6, 62, 71*).

Constraints also exist during Nodal-mediated patterning of the left-right axis (*16*). During embryogenesis, both the left and the right lateral plate mesoderm initially express low levels of Nodal, but cilia-induced flow in the node generates a prepattern that is thought to result in slightly higher expression of Nodal on the left. This initial asymmetry is amplified by Nodal auto-regulation and the induction of Lefty. The long-range activity of Lefty then suppresses Nodal signaling in the right lateral plate mesoderm. Thus, Nodal/Lefty interactions appear to amplify small differences between left and right lateral plate mesoderm using short-range activation and long-range inhibition. In contrast to mesendodermal patterning, in which graded Nodal signaling specifies multiple cell fates, Nodal signaling during during left-right patterning controls the binary decision between left and right (*19*). Similar to mesendodermal patterning, the Nodal/Lefty system during left-right patterning is constrained by prepatterns, the length scale of the system and the rapid assignment of cell fates.

3 Generation and Characterization of Fluorescent Nodal and Lefty Proteins

3.1 Rationale and summary

To visualize Nodal and Lefty signals in living embryos, we generated GFP and Dendra2 fusion proteins (Fig. 2 and figs. S2-S11). A major concern in studies of signaling molecules is whether the position or the size of the fluorescent tag alters the signaling activity, clearance or dispersal characteristics of the protein. We therefore systematically analyzed dozens of constructs to identify fusion proteins that were active and properly processed. Western blots indicated that the fluorescent fusion proteins were processed and present as mature ligands in the extracellular space (fig. S2 and fig. S6). qRT-PCR (fig. S3) and RNA *in situ* hybridization analyses (fig. S4) indicated that tagged Nodals were potent inducers of Nodal target gene expression, whereas tagged Leftys repressed Nodal target genes (figs. S7-S9). To examine the ranges of the fusion proteins, we generated clones of cells expressing the constructs of interest similar to previous studies (*14, 23*). Reflecting the properties of their untagged counterparts, Cyclops and Squint fusions had short- and mid-range activity (fig. S5), respectively, whereas Lefty fusions had long-range inhibitory activity (fig. S10).

3.2 Cloning of fusion constructs

All enhanced GFP (referred to as GFP throughout the text) and Dendra2 fusion constructs were generated by PCR-based methods (*72*) and cloned into the *pCS2(+)* vector. Briefly, fragments encoding fluorescent proteins or Nodal and Lefty domains were amplified individually and spliced together by PCR using overlapping overhangs. The untagged constructs were cloned into the same restriction sites in *pCS2(+)* as the fusion constructs. All constructs contain the consensus Kozak sequence *gccacc* 5' of the start codon.

Cyclops fusions: Sequences encoding fluorescent proteins or the FLAG tag (DYKDDDDK) were inserted two amino acids downstream of the Furin cleavage site (RRGRR) between the pro- and mature domains of Cyclops. To generate Cyclops-FLAG-GFP, the sequence encoding DYKDDDDKLG was inserted between the pro-domain and GFP two amino acids downstream of the Furin cleavage site. The fusion constructs were cloned into the *pCS2(+)* vector via ClaI and EcoRI restriction sites.

Squint fusions: Sequences encoding fluorescent proteins or the FLAG tag were inserted between the pro- and mature domains of Squint 10 amino acids downstream of the Furin cleavage site (RRHRR) with a GSTGTT linker separating the prodomain and the fluorescent protein and a GS linker separating the fluorescent protein from the mature domain. To generate Squint-FLAG-GFP, the sequence encoding GSTGTTDYKDDDDKLG was inserted between the pro-domain and GFP 10 amino acids downstream of the Furin cleavage site. The fusion constructs were inserted into the *pCS2(+)* vector via ClaI and EcoRI restriction sites.

Lefty1 fusions: Sequences encoding fluorescent proteins or the FLAG tag were inserted at the C-terminus of full-length Lefty1. An LG linker was used to separate Lefty1 from the FLAG tag, and an LGDPPVAT linker was used between Lefty1 and the fluorescent proteins GFP and Dendra2. To generate Lefty1-GFP-FLAG, the FLAG tag was fused to the C-terminus of GFP separated by an LG linker. The fusion constructs were inserted into the *pCS2(+)* vector via ClaI and XhoI restriction sites.

Lefty2 fusions: Sequences encoding fluorescent proteins or the FLAG tag were fused to the C-terminus of full-length Lefty2. An LG linker was used to generate Lefty2-FLAG and Lefty2-GFP, and an LGDPPVAT linker was used between Lefty2 and Dendra2. To generate Lefty2-GFP-FLAG, the FLAG tag was fused to the C-terminus of GFP separated by an LG linker. The fusion constructs were inserted into the *pCS2(+)* vector via ClaI and XhoI restriction sites.

Secreted GFP and Dendra2: Sequences encoding fluorescent proteins were fused to the pro-domain of Squint 10 amino acids downstream of the Furin cleavage site (RRHRR) with a GSTGTT linker following the Furin cleavage site. The fusion constructs were inserted into the *pCS2(+)* vector via ClaI and XhoI restriction sites.

Global proteome-wide studies in cell culture suggest that fluorescent proteins in general do not affect the degradation dynamics of fusion partners (*73-75*). Indeed, the secreted Dendra2 control construct reported here had a significantly higher extracellular half-life than the Nodal fusions (see Text S5 "Measurement of Clearance Rate Constants", fig. S13, and Table S3).

Given that the Nodal and Lefty fluorescent fusion proteins have a molecular mass of up to three times higher than the untagged ligands, it can be expected that the tagged ligands are less mobile than the untagged ligands. The Einstein-Stokes equation relates the diffusion coefficient D to the radius r of spherical particles diffusing through liquid with low Reynolds numbers:

$$D = \frac{k_B T}{6 r \pi \eta} \tag{19}$$

where k_B is the Boltzmann constant, T is temperature and η is the viscosity (*11, 76*). With the simplifying assumption that the proteins are perfect spheres and that the volume of the fusion constructs is approximately threefold larger than the volume of the untagged proteins, the radii of the fusion constructs will be ∼1.4-fold larger than those of the untagged proteins. Therefore, using the Einstein-Stokes equation, the diffusion coefficients of the GFP fusion proteins is expected to be only ∼30% smaller than those of the untagged ligands. This lower diffusivity may be reflected in the slightly reduced activity ranges observed for the fusion constructs (fig. S5 and fig. S10). However, it is unlikely that the proteins fold into perfect spheres, and differences in protein conformation and tertiary structure might lead to additional deviations from the ideal behavior described by the Einstein-Stokes equation.

3.3 mRNA synthesis, embryo injections and *in situ* hybridization

Capped mRNAs were synthesized using the mMessage mMachine Kit (Ambion) with SP6 RNA polymerase according to the manufacturer's protocol. Vectors were linearized by digestion with

NotI. Embryos were dechorionated using 1 mg/ml Pronase (Protease type XIV from Streptomyces griseus, Sigma) prior to injection and subsequently cultured in agarose-coated dishes.

For *in situ* hybridization, embryos were fixed overnight at 4°C using 4% formaldehyde in PBS. *In situ* hybridization and anti-sense probe synthesis for *fascin*, *no tail* and *goosecoid* probes (*23, 77*) was carried out according to standard protocols (*78*).

3.4 Preparation of extracellular protein fractions for western blots

If degradative processes generate free extracellular fluorescent species by cleaving fusions between the mature ligand and the fluorescent protein, the measurements of the half-lives would likely be overestimates given that free Dendra2 is cleared relatively slowly (fig. S13 and Table S3). Furthermore, if there were significant amounts of free GFP, the recovery dynamics in the FRAP experiments could be dominated by the smaller and highly diffusive free GFP, thereby increasing the apparent diffusion coefficients of the fusion proteins. To determine whether the Dendra2 and GFP fusion proteins were processed correctly (i.e. without releasing free fluorescent species), extracellularly enriched fractions were purified and analyzed by immunoblotting using anti-Dendra2 and anti-GFP antibodies. As shown in fig. S2 and fig. S6, no significant amounts of free extracellular Dendra2 or GFP were detected, and the majority of the species fused to Dendra2 or GFP was processed correctly. Therefore, the majority of the extracellular signal in the clearance assay and FRAP experiments likely originated from fusion proteins rather than free Dendra2 or GFP.

Embryos at the one- or two-cell stage were injected with the mRNAs encoding GFP or Dendra2 fusion proteins indicated in fig. S2 and fig. S6 with mRNA amounts equimolar to 250 pg Squint-GFP mRNA (Cyclops-GFP/Dendra2: 284 pg, Squint-GFP/Dendra2: 250 pg, Lefty1-GFP/Dendra2: 234 pg, Lefty2-GFP/Dendra2: 236 pg, secreted GFP/Dendra2: 209 pg). mRNA encoding FLAG-tagged and FLAG-GFP-tagged constructs were injected at the one- or two-cell stage at equimolar amounts for each protein species (Cyclops-FLAG: 360 pg, Cyclops-FLAG-GFP: 500 pg; Squint-FLAG: 85 pg, Squint-FLAG-GFP: 125 pg; Lefty1-FLAG: 330 pg, Lefty1-GFP-FLAG: 500 pg; Lefty2-FLAG: 330 pg, Lefty2-GFP-FLAG: 500 pg). Embryos were grown at 28°C and manually de-yolked between sphere and dome stages in embryo medium (250 mg/l Instant Ocean salt, 1 mg/l methylene blue in reverse osmosis water adjusted to pH 7 with $NaHCO_3$) in agarose-coated dishes using forceps. The resulting blastoderm caps were washed three times in embryo medium to remove excess yolk. Approximately twenty caps (60 caps for FLAG-tagged constructs) were transferred into 50 or 100 µl deyolking buffer (*79*) (a quarter of a protease inhibitor cocktail tablet (Complete Mini, Roche) per 2 ml deyolking buffer was used for the FLAG-tagged constructs) and shaken at 1,100 rpm using an Eppendorf shaker cooled to 4°C. Cells were then spun down at 300 g for 30 seconds at 4°C, and 40 or 80 µl of the supernatant was transferred to a new tube that was frozen immediately in liquid nitrogen. Protein samples mixed with Laemmli buffer were denatured by incubation for 10 min at 98°C, resolved by SDS-PAGE using 10-12% polyacrylamide gels and transferred to PVDF membranes (GE Healthcare). Membranes were blocked with 5% (3% for FLAG-tagged constructs) non-fat milk (BioRad) in TBST. The membranes were incubated with primary antibodies in 5% (3% for FLAG-tagged constructs) non-fat milk in TBST at 4°C overnight. Anti-

GFP (Molecular Probes/Invitrogen) and anti-Dendra2 (obtained from Evrogen and antibodies-online Inc.) antibodies were used at a concentration of 1:5,000, anti-FLAG antibody (Sigma) at a concentration of 1:1,000, and monoclonal anti-β-tubulin antibody (Sigma) at a concentration of 1:25,000. Proteins were detected using HRP-coupled secondary antibodies (goat anti-rabbit and donkey anti-mouse (Jackson ImmunoResearch Labs)) at a 1:25,000 (1:5,000 for FLAG epitope detection) dilution. Chemiluminescence was detected using ECL Plus reagent (Amersham) and imaging film (Kodak BioMax Light). The purification protocol yields an enriched extracellular fraction that contains residual amounts of β-tubulin.

3.5 Analysis of fusion protein activity

Quantitative reverse transcription PCR: Quantitative reverse transcription PCR (qRT-PCR) was used to assess the activity of the fusion constructs. Embryos were injected with two different amounts of mRNA per construct (see fig. S3 and fig. S8 for amounts) to assess dose-dependent activation or repression of the Nodal target gene *goosecoid* (*gsc*) (*77, 80, 81*). To correct for the length differences between constructs, equimolar amounts of tagged and untagged constructs were injected. Ten embryos per sample were frozen in liquid nitrogen, and three samples were obtained per construct. Uninjected embryos and embryos injected with Lefty1 and Lefty2 constructs were frozen at 50% epiboly, at the end of blastula stage. Embryos injected with Nodal constructs arrest during epiboly and were frozen when uninjected siblings reached 50% epiboly. Total RNA was extracted using Trizol reagent (Invitrogen). cDNA was generated using the iScript cDNA Synthesis Kit (Bio-Rad). The zebrafish *elongation factor 1-α* (*eF1α*) transcript was used as a normalization control (*82*). qRT-PCR was performed using either the Qiagen QuantiTect SYBR Green PCR Kit or Promega Go-Taq qPCR Master Mix on a Stratagene MX3000p qPCR machine. C_t values were determined using MxPro software. Fold changes in *gsc* relative to *eF1α* levels were calculated using the $\Delta\Delta C_T$ method (*83*).

Primer sequences used:
eF1α forward: agaaggaagccgctgagatgg
eF1α reverse: tccgttcttggagataccagcc
gsc forward: gagacgacaccgaaccattt
gsc reverse: cctctgacgacgacctttc

Whole mount *in situ* hybridization: Embryos were injected with the mRNA amounts indicated in fig. S4 and fig. S9. To correct for the length differences between the constructs, equimolar amounts of tagged and untagged constructs were injected. Uninjected embryos and embryos injected with Lefty1 and Lefty2 constructs were fixed at 50% epiboly, at the end of blastula stage. Embryos injected with Cyclops and Squint constructs were fixed when uninjected siblings reached 50% epiboly. To assess ectopic induction or repression of Nodal target genes, a probe against the Nodal target gene *goosecoid* (*gsc*) (*77, 80, 81*) was used. Using a dissecting microscope, embryos were scored according to the scoring classes shown in fig. S4 and fig. S9, similar to (*84*). Representative embryos were imaged using an Axio Imager.Z1 microscope (Zeiss). Images were cropped according to the diameter of the imaged embryos.

3.6 Analysis of fusion protein activity range

Cyclops and Squint constructs: Donor embryos were co-injected with mRNA amounts equimolar to 250 pg of Squint-GFP mRNA (Cyclops-GFP: 284 pg, Squint-GFP: 250 pg, Lefty1-GFP: 234 pg, Lefty2-GFP: 236 pg) and 0.25 mg/ml 10 kDa biotinylated dextran (Molecular Probes) in a volume of 1 nl at the one-cell stage. Embryos developed at 28°C. At sphere stage, embryos were transferred to modified Danieau's medium (0.2 µm filtered solution of 58 mM NaCl, 0.7 mM KCl, 0.4 mM $MgSO_4$, 0.3 mM $CaCl_2$, 5 mM HEPES pH 7.2, 5% Penicillin/Streptomycin). Approximately 40 to 50 cells from donor embryos were transplanted into the animal pole of wildtype host embryos at sphere stage. Embryos were fixed one hour later and processed for *in situ* hybridization using *fascin* (*77*) or *no tail* (*23*) probes. The presence of biotinylated dextran in donor cells was detected using the Elite Vectastain ABC kit (VECTOR Laboratories) and DAB substrate. Stained embryos were imaged using an Axio Imager.Z1 microscope (Zeiss). The area occupied by donor cells and the area occupied by *fascin* or *no tail* gene expression was quantified in animal pole views using ImageJ (*85*). The activity range was calculated as the ratio of the *fascin*- or *no tail*-positive area divided by the clone area as shown in fig. S5.

Lefty1 and Lefty2 constructs: In order to assess the activity range of the Lefty fusion proteins, clonal sources were generated by injecting mRNAs encoding the Lefty constructs along with biotinylated dextran as an injection tracer in a volume of 100 pl into a single blastomere at the 64- to 128-cell stage. The suppression of the Nodal target gene *fascin* was assessed by *in situ* hybridization using embryos that were fixed at 50% epiboly stages. Embryos were categorized into classes of *fascin* suppression as shown in fig. S10.

3.7 Assessment of fusion proteins

Cyclops fusions: Western blots of extracellular fractions indicate that the Cyclops fusions are processed to mature ligands (fig. S2). Equimolar injections of mRNA encoding Cyclops-FLAG and Cyclops-FLAG-GFP yield similar protein levels (fig. S2). The amount of recovered Cyclops protein on the western blot is lower than the amounts recovered for Squint, Lefty1 and Lefty2, potentially owing to its higher clearance (Table S3) or its punctate membrane-associated localization (fig. S11). The Cyclops fusions with GFP and Dendra2 had activity similar to untagged Cyclops (fig. S3 and fig. S4), and their activity range was slightly reduced (fig. S5).

Squint fusions: The Squint fusions were processed and present as mature ligands in the extracellular space (fig. S2). Equimolar injections of mRNA encoding Squint-FLAG and Squint-FLAG-GFP yields similar protein levels (fig. S2). The Squint fusions had similar activity as untagged Squint (fig. S3 and fig. S4) and an approximately 30% decreased activity range, consistent with their larger size (fig. S5).

Lefty1 fusions: The Lefty1 fusions were present as mature ligands in the extracellular space (fig. S6). Equimolar injections of mRNA encoding Lefty1-FLAG and Lefty1-GFP-FLAG yield

lower Lefty1-GFP-FLAG protein levels compared to Lefty1-FLAG (fig. S6). The Lefty1 fusions were potent long-range repressors of Nodal target gene expression (figs. S7-S10). The decreased activity and activity range of the Lefty1 fusions compared to untagged Lefty1 at equimolar mRNA amounts is likely due to differences in protein levels (fig. S6), since Nodal target gene expression can be suppressed to a similar extent by injecting higher mRNA amounts of the Lefty1 fusions (figs. S7-S9).

Lefty2 fusions: The Lefty2 fusions were present as mature ligands in the extracellular space (fig. S6). Equimolar injections of mRNA encoding Lefty2-FLAG and Lefty2-GFP-FLAG yield lower Lefty2-GFP-FLAG protein levels compared to Lefty2-FLAG (fig. S6). The Lefty2 fusions were very potent repressors of Nodal signaling and had long-range activity (figs. S7-S10). The slightly decreased activity of the Lefty2 fusions compared to untagged Lefty2 at equimolar mRNA amounts is likely due to differences in protein levels (fig. S6), since Nodal target gene expression can be suppressed to a similar extent by injecting higher mRNA amounts of the Lefty2 fusions (figs. S7-S9).

4 Measurement of Distribution Profiles

4.1 Rationale and summary

Previous embryological and genetic studies have shown that Cyclops, Squint, Lefty1 and Lefty2 have very different ranges of activity during mesendoderm induction, despite similar molecular weights: Cyclops has short-range activity, Squint has mid-range activity, and Leftys have long-range inhibitory activity (*6, 23*) (Fig. 1A, fig. S5, and fig. S10). Analogous studies in left-right patterning suggest that Lefty has a longer range than Nodal (*16, 24*). To analyze the *in vivo* distributions of Cyclops-GFP, Squint-GFP, Lefty1-GFP and Lefty2-GFP, we expressed the fusion proteins (figs. S2-S11) from a local source in blastula-stage embryos (Fig. 2). Fluorescence quantification revealed that Cyclops-GFP formed a short-range gradient, Squint-GFP a mid-range gradient, Lefty1-GFP a long-range gradient and Lefty2-GFP a super-long-range shallow gradient (Fig. 2). The distance from the source at which the concentration dropped to 50% of the value at the source boundary was $\sim$20 μm for Cyclops-GFP, $\sim$40 μm for Squint-GFP, $\sim$80 μm for Lefty1-GFP, and $\sim$100 μm for Lefty2-GFP. These distribution profiles are in good agreement with the activity ranges deduced from embryological and genetic studies.

4.2 Experimental setup

In order to characterize the protein distribution profiles of Nodals and Leftys, clonal sources of GFP fusion proteins were generated by transplantation. Such clones recapitulate the major aspects of patterning induced by endogenous sources: High- and low-threshold target genes are induced in and around Nodal-expressing clones (*23*), the different ranges of Cyclops, Squint and Lefty proteins are maintained (*6, 23*), cell internalization associated with gastrulation can be induced (*69, 70*), and cross-regulation of Nodals and Leftys is preserved (*6, 62, 71*).

Donor embryos were injected with mRNA at amounts equimolar to 250 pg of Squint-GFP mRNA at the one-cell stage (Cyclops-GFP: 284 pg, Squint-GFP: 250 pg, Lefty1-GFP: 234 pg, Lefty2-GFP: 236 pg). At sphere stage, approximately 40-50 cells were explanted, left briefly in modified Danieau's medium to allow residual extracellular fluorescent proteins to dissipate, and then transplanted into wildtype host embryos (Fig. 2). Embryos were mounted in 1% low-melting point agarose in glass-bottom Petri dishes (MatTek Corporation) with the animal pole facing the coverslip. The dishes were then filled with embryo medium in order to hydrate the agarose during imaging. Embryos were imaged 30, 60 and 120 min post transplantation using a Pascal confocal microscope (Zeiss) with a 25× objective. Images (z-stacks) were acquired in 5 different confocal slices separated by 5 μm at each time point. Imaging earlier than 30 min post-transplantation was not possible due to the handling times involving transplantation, embryo immobilization and sample mounting.

To test whether ectopic expression of the constructs causes saturation of binding sites on cell surfaces that influence the diffusion properties of Nodals and Leftys, 30 pg of mRNA encoding untagged Squint were injected into the host embryos (similar to the concentration used in the FRAP experiments, see Text S6 "Measurement of Effective Diffusion Coefficients"), and the transplantation and imaging conditions were as described above. No significant difference in the

Squint-GFP gradients was observed in the absence or presence of untagged Squint, indicating that saturation of binding sites does not occur under these conditions (fig. S17).

4.3 Image analysis

Images were analyzed in ImageJ (*85*) as follows: Maximum intensity projections were generated for individual z-stacks comprising five confocal slices, similar to (*12*). To measure the fluorescence intensity as a function of distance from the clone, a rectangular region of interest (ROI) with a height of 36.56 µm (corresponding to 52 pixels) abutting the clone was drawn. The width of the ROI differed depending on the size of the embryo. The average intensity in 0.7 µm strips within the ROI was calculated. To subtract background due to autofluorescence, average intensity profiles were calculated that were extracted from four medial positions each within three ungrafted wildtype embryos, where the z-position and developmental time were matched. These background datasets were truncated at each end to clip off regions where intensities deviate from the baseline due to embryo curvature. The average baseline intensity for background subtraction was then calculated as a single value. The background-subtracted experimental intensity profiles were truncated in the same way as the background data sets. After background subtraction and truncation, an average of 7 µm was binned using a sliding window similar to previous studies (*26, 86-88*). The resulting data was normalized to the value closest to the clonal source boundary, and the normalized data was sampled every 3.5 µm as shown in Fig. 2. Embryos with low signal-to-noise ratios were excluded from the analysis. To facilitate visualization, alternate color maps were chosen, and the minimum and maximum displayed values were adjusted globally for each image.

5 Measurement of Clearance Rate Constants

5.1 Rationale and summary

The clearance kinetics of extracellular signaling molecules can be a major determinant of their distribution: the more quickly a signal is cleared from the extracellular space, the shorter its range (*11-14*). To determine whether the differences between the distributions of Nodal and Lefty signals are due to differences in their clearance kinetics, we measured extracellular half-lives. We developed a pulse-labeling assay to monitor the extracellular clearance of fluorescent fusion proteins (Fig. 3 and fig. S12). Nodal and Lefty signals were fused to the photoconvertible protein Dendra2 (*25, 89*) (figs. S2-S11), uniformly expressed in blastula embryos and photoconverted throughout the entire embryo with a short UV pulse. Observation of changes in the photoconverted extracellular signal over time allowed measurement of extracellular protein half-lives (Fig. 3 and fig. S12). Control experiments indicated that non-uniform photoconversion (fig. S14) and photobleaching (fig. S16) did not alter measurements, and that the extracellular photoconverted Dendra2 signal was significantly above background (fig. S15). Extracellular half-lives between 95 and 218 min were obtained for Nodal- and Lefty-Dendra2 fusion proteins.

Two previous studies have examined the clearance kinetics of Nodal and Lefty signals. Jing et al. used autoradiography to characterize the decay dynamics of radioactively pulse-labeled Cyclops- and Squint-GFP expressed in COS7 tissue culture cells (*90*). Half-lives of two (Cyclops-GFP) and eight hours (Squint-GFP) were identified, but it is unclear whether clearance in a mammalian tissue culture system reflects clearance in zebrafish embryos. Marjoram and Wright introduced tissue grafts expressing Myc-tagged *Xenopus* Lefty and Xnr1 (a *Xenopus* Nodal homolog) into *Xenopus* lateral plate mesoderm, then removed the grafts and used quantitative immunohistochemistry to follow the decrease in Myc signal over time. This analysis revealed half-lives of 45 min for Lefty and 25 min for Xnr1 (*24*), but the observed decrease in signal intensity might be caused by diffusion of labeled protein into deeper layers of the embryo, leading to an apparent shortening of half-lives (see Text S5.6 "Uniform Photoconversion"). Moreover, protein clearance may differ between species (*Xenopus* versus zebrafish) and tissues (lateral plate mesoderm versus blastula), and the inability to distinguish between intra- and extracellular fractions prevents assessment of extracellular clearance. We therefore developed an alternative approach for the measurement of extracellular protein half-lives *in vivo*: Pulse-labeling of photoconvertible fusion proteins allowed clearance kinetics to be examined in live zebrafish embryos.

5.2 Experimental setup

Since secreted proteins predominantly spread through tissues by extracellular movement (*11, 91*), extracellular, not intracellular, clearance is an important determinant of signal range. For example, a signal that is slowly cleared intracellularly but quickly cleared extracellularly will have a shorter range than a signal that is slowly cleared both intra- and extracellularly. To avoid these potential pitfalls, we measured the clearance of photoconverted fusion proteins intracellu-

larly and extracellularly. No signicant differences were found between intra- and extracellular half-lives for Nodal-and Lefty-Dendra2 constructs (Table S3).

To determine intra- and extracellular half-lives, embryos were injected at the one-cell stage with 60 pg of mRNA encoding the Dendra2 fusion constructs along with 0.4-1.9 ng of a 3 kDa Alexa488-dextran conjugate (Invitrogen). The total injection volume was 1 nl. The Alexa488 signal was used during image analysis (see below) to mask cells in order to analyze extracellular or intracellular signal only. Several different tracers were tested, and Alexa488-dextran was selected because it was found to be non-toxic and bright. Injected embryos developed at 28°C and were kept in the dark until mounting between dome stage and 30% epiboly (∼5 hours post fertilization) to prevent inadvertent photoconversion. Mounting was as described previously (see Text S4 "Measurement of Distribution Profiles"), except that embryos were mounted in 1% low melting point agarose in modified Danieau's medium, and Petri dishes were filled with modified Danieau's medium rather than embryo medium. Modified Danieau's medium was used because embryo medium contains methylene blue, which produces background red fluorescence that can obscure relevant signal.

Experiments were performed on an inverted Pascal confocal microscope (Zeiss). Embryos were maintained at 28°C during the experiments using a heated stage. Images of size 512 × 512 pixels were acquired with a 40× objective, while photoconversion was performed using a 10× objective. Immediately after mounting, a "pre-photoconversion" image was taken from a single confocal plane corresponding to a thickness of less than 3.3 µm, at a depth of about 30 µm from the animal pole. The 543 nm laser output was 20% (for imaging of red fluorescence), and the 488 nm laser output was between 0.25 and 1.0% (for imaging green fluorescence). Because Cyclops-Dendra2 signal is often concentrated in bright membrane-associated clusters that are saturated under the gain settings used for the other constructs, lower gain settings were used for acquisition of Cyclops-Dendra2 images in the red channel.

Embryos were photoconverted using a two-minute pulse of UV light from a mercury lamp at 100% output, while constantly manually shifting the focal plane. The 10× objective was used to photoconvert multiple embryos simultaneously. After photoconversion, a multitime imaging macro was used to image each embryo on the dish sequentially over a total period of 300 min post-photoconversion with intervals of either 10 or 20 min between images (see Text S5.6 "Controls for clearance assay"). The imaging conditions for the post-photoconversion images were identical to those described above for the pre-photoconversion images.

Controls demonstrated little drift in x, y or z over the duration of the time lapse experiments. Red fluorescent beads with 1 µm diameter (FluoSpheresNeutrAvidin labeled microspheres (580/605), Invitrogen) were embedded in 1% agarose. Four positions were imaged at 10 min intervals for 300 min, similar to the clearance assay experiments. We did not observe significant shifting of the beads from their original positions during the course of the experiment.

5.3 Image analysis

Custom macros in ImageJ (*85*) were used to measure the change in average photoconverted Dendra2 signal intensity over time. Intensities were measured in three compartments: extracellular space, intracellular space, and in the entire optical slice (extracellular and intracellular

combined, excluding extraembryonic regions). For each time point, the extracellular space was defined by thresholding the Alexa488 signal (which labels cells but not extracellular space) using the Otsu thresholding algorithm (which is based on the minimization of inter-class variance between two histogram classes (*92*)). Intracellular pixels defined by the Alexa488 mask were not considered for calculations of the extracellular signal in the red channel (fig. S13). Calculating the average intensity in a region of interest drawn around the embryo (to exclude extraembryonic space) is thus equivalent to summing the intensities of the extracellular pixels and dividing this sum by the number of extracellular pixels (i.e. the extracellular area A_{ext} in units of pixels). To measure intracellular average intensities, the mask was inverted.

In summary, at each time frame t_n the spatial average $\bar{I}_{ext}$ in the extracellular area A_{ext}, $\bar{I}_{int}$ in the intracellular area A_{int}, and $\bar{I}_{sl}$ in the entire slice A_{sl} was computed by

$$\begin{aligned}
\bar{I}_{ext}(t_n) &= \frac{1}{A_{ext}} \sum_{i,j} I_{ext}(i,j,t_n) \\
\bar{I}_{int}(t_n) &= \frac{1}{A_{int}} \sum_{i,j} I_{int}(i,j,t_n) \\
\bar{I}_{sl}(t_n) &= \frac{1}{A_{sl}} \sum_{i,j} I_{sl}(i,j,t_n)
\end{aligned}$$

where i and j represent the coordinates of pixels that fall inside of A_{ext}, A_{int} and A_{sl}, respectively.

Embryos that died, produced very low levels of photoconverted Dendra2 signal after photoconversion, or whose position shifted significantly during the experiment were excluded from analysis. For Cyclops-Dendra2 experiments, only embryos in which clusters were uniformly distributed and highly abundant immediately post photoconversion were included in the analysis.

5.4 Data fitting

Photoconversion led to a homogenous distribution of the photoconverted signal in the blastoderm (fig. S14). With the assumption that the photoconverted red fluorescent signal was cleared over time with the clearance rate constant k_1, without contributions from *de novo* production or diffusion to the change in signal over time, the change in concentration with respect to time in these experiments is described by the ordinary differential equation (ODE)

$$\frac{dc}{dt} = -k_1 c$$

The solution to this equation is an exponential function with c_0 as a starting value obtained from the initial condition (IC). For all constructs, a single exponentially decaying function with offset y_0

$$c(t) = c_0 e^{-k_1 t} + y_0 \tag{20}$$

was therefore fitted to the experimental data $\bar{I}(t_n)$ from individual embryos by minimizing the sum of squared differences (SSD)

$$SSD = \sum_n \left(\bar{I}(t_n) - c(t_n)\right)^2$$

Table S1. Minimization parameters for clearance assay fitting.

Description	Value
Initial guess for k_1	0
Lower limit for k_1	0
Upper limit for k_1	∞
Initial guess for y_0	Average intensity of first postconversion image $\bar{I}_{\text{post}}(t_0)$
Lower limit for y_0	$F\left(\bar{I}_{\text{pre}} - \bar{N}\right) + \bar{N}$, with
	F: minimum value of $\frac{\bar{B}-\bar{N}}{\bar{B}_{\text{pre}}-\bar{N}}$ (see Table S2)
	$\bar{B}$: average background intensity
	$\bar{B}_{\text{pre}}$: preconversion background average intensity
	$\bar{N}$: average instrument noise
Upper limit y_0	Maximum value of $\bar{I}_{\text{int}}$
Initial guess for c_0	$\bar{I}_{\text{post}}(t_0) - \bar{I}_{\text{pre}}$
Lower limit for c_0	0
Upper limit for c_0	∞

Table S2. F values for all constructs and compartments.

Construct	Extracellular	Slice (embryo)	Intracellular
Cyclops-Dendra2	0.9922	0.9705	0.9258
Squint-Dendra2	0.9597	0.8612	0.8281
Lefty1-Dendra2	0.9562	0.9791	0.9818
Lefty2-Dendra2	0.9461	0.9590	0.9799
Secreted Dendra2	n.d.	n.d.	n.d.

using a constrained optimization algorithm (Nelder-Mead, MATLAB), where the solution of the model c was evaluated at the n discrete time points t_n. See Table S1 for fitting constraints and initial parameter value guesses.

y_0 represents the background intensity. It is not necessarily equivalent to the preconversion value. Reasons that y_0 may deviate from the preconversion value for extracellular fits include secretion of photoconverted protein, the possible existence of a small amount of free photoconverted Dendra2 (fig. S2 and fig. S6), accidental photoconversion prior to acquisition of the pre-photoconversion image, and small fluctuations in background intensity over time. In addition, there seems to be a slight increase in background intensity subsequent to photoconversion (fig. S15). Therefore, for each embryo the upper y_0 limit was conservatively defined as the maximum average intensity from the intracellular fraction. The lower y_0 limit was adjusted to a percentage of the pre-photoconversion value based on fluctuations in background intensities and extraembryonic background (Table S1, Table S2, and fig. S15). Extraembryonic background for Cyclops-Dendra2 imaging conditions was ∼60 a.u. For all other imaging conditions extraembryonic background was ∼70 a.u.

The k_1 values determined for individual embryos were averaged for each construct (see Table

S3 for a summary of extracellular, embryo and intracellular clearance rate constants). Average half-lives $\bar{\tau}$ were calculated from average k_1 values $\bar{k}_1$ using the relationship

$$\bar{\tau} = \frac{\ln(2)}{\bar{k}_1} \tag{21}$$

5.5 Statistical tests

The Wilcoxon-Mann-Whitney test in R (*93*) with a significance cutoff of 0.005 was used to determine whether k_1 values significantly differed between constructs. See fig. S13 for a summary of the statistical analysis.

Table S3. Summary of clearance rate constants k_1.

Construct	Extracellular k_1 (10^{-4}/s)	Slice (embryo) k_1 (10^{-4}/s)	Intracellular k_1 (10^{-4}/s)	n
Cyclops-Dendra2	1.22 ± 0.13	1.43 ± 0.15	1.41 ± 0.14	9
Squint-Dendra2	1.00 ± 0.06	0.81 ± 0.04	0.77 ± 0.05	23
Lefty1-Dendra2	0.53 ± 0.05	0.56 ± 0.17	0.70 ± 0.05	19
Lefty2-Dendra2	0.69 ± 0.07	0.67 ± 0.14	0.93 ± 0.14	27
Secreted Dendra2	0.51 ± 0.05	0.47 ± 0.07	0.91 ± 0.14	22

Values represent the mean ± standard error of n experiments.

5.6 Controls for clearance assay

Uniform photoconversion: Non-uniform photoconversion could be a source of error when determining the half-lives of Dendra2 fusion proteins. For example, diffusion of photoconverted protein out of the imaging plane could be misinterpreted as clearance if photoconversion were biased towards the animal pole. To determine whether photoconversion is uniform along the animal-vegetal axis, embryos were co-injected with 60 pg of mRNA encoding secreted Dendra2 and 1.9 ng of Alexa488-dextran at the one-cell stage and imaged starting between dome stage and 30% epiboly. A z-stack comprised of 10 slices spaced 8 µm apart was taken every 20 min post-photoconversion for a total of 80 min. Photoconversion and imaging conditions were identical to those used in the clearance assay experiments. The average intensity in a small circular ROI (∼35 µm diameter) in the center of each z-slice was determined and plotted as a function of depth for each time point (fig. S14; intensity decreases at deeper imaging planes due to light scattering and absorbance). If photoconversion were biased towards the animal pole, the red intensity profile should change over time, i.e. the (normalized) intensities near the vegetal end should increase due to diffusion. However, minimal differences were observed between the normalized red intensity profiles from early and late times. The same trend was observed for the intracellular Alexa488 signal, which was uniformly distributed throughout the embryo. This suggests that photoconversion was likely uniform or near-uniform along the animal-vegetal axis.

Fluctuations in background intensity: To identify potential changes in background intensity over the five-hour imaging period that would require adjustment of data from the clearance assay experiments, embryos were co-injected with 1.9 ng of Alexa488-dextran and 40 pg of mRNA encoding untagged Cyclops, Squint, Lefty1 or Lefty2. These embryos were then mock photoconverted and imaged identically to the embryos used in the clearance assay described above, and the resulting average intensities in the extracellular space, intracellular space, and entire optical slice were determined (see Text S5.3 "Image analysis"). No significant changes in intensity in any of these compartments during the five hours of imaging were detected (fig. S15). Because background intensities remained relatively constant over time, dynamic background adjustment of the data from the clearance assay experiments was not required.

Photobleaching and inadvertent photoconversion: If continuous time-lapse imaging results in photobleaching, the clearance kinetics of the Dendra2 fusion proteins would be artifactually modulated. Likewise, excitation by the 488 nm laser could cause inadvertent photoconversion of newly synthesized Dendra2 and also lead to artifactual clearance kinetics. Therefore, experiments were performed to determine whether significant photobleaching or inadvertent photoconversion occurred in the clearance assay. For each construct, experiments with imaging intervals of 10 or 20 minutes were performed. If significant photobleaching occurred, the half-lives extracted from the images collected with 20 min intervals should be higher than those obtained from images collected with 10 min intervals, because the signal intensity should decrease less rapidly with less laser exposure. In contrast, if significant inadvertent photoconversion occurred, the half-lives extracted from the images collected with 20 min intervals should be lower than those obtained from images collected with 10 min intervals, because continuous photoconversion would increase the perceived signal intensity and counterbalance clearance. No statistically significant difference was observed between half-lives from data obtained with 10 or 20 min intervals, indicating that detectable photobleaching or inadvertent photoconversion did not occur in the clearance assay (fig. S16). Significance was determined using the Wilcoxon-Mann-Whitney test in R (*93*) with a significance cutoff of 0.005.

6 Measurement of Effective Diffusion Coefficients

6.1 Rationale and summary

The diffusivity of extracellular signaling molecules can be a major determinant of their distribution: the more diffusive a signal is in the extracellular space, the longer its range (*11*). To determine the effective diffusion coefficients (D) of Nodals and Leftys, we developed a FRAP (Fluorescence Recovery After Photobleaching) assay in zebrafish (Fig. 4 and fig. S18). FRAP involves the irreversible bleaching of fluorescent molecules in a region of interest. The dynamics of re-appearance of fluorescence in the bleached region can be used to extract information about the mobility of the fluorescent species (*12, 13, 26, 94-96*). Our FRAP data support a diffusive process for the movement of Nodal and Lefty signals (figs. S23-S25). Previous studies in *Drosophila* embryos and imaginal discs have used one- or two-dimensional models to analyze FRAP data (*12, 13, 26*). The more complex geometry of the zebrafish embryo made it necessary to develop a three-dimensional model for the analysis of our FRAP data (figs. S19-S20). In addition, we also accounted for the effects of production and clearance (fig. S21) as well as time delays between the end of the bleaching and the beginning of the post-bleach imaging (fig. S22). We used this three-dimensional model to measure the effective diffusivity of Cyclops-GFP ($D = 0.7 \pm 0.2\,\mu m^2/s$), Squint-GFP ($D = 3.2 \pm 0.5\,\mu m^2/s$), Lefty1-GFP ($D = 11.1 \pm 0.6\,\mu m^2/s$), and Lefty2-GFP ($D = 18.9 \pm 3.0\,\mu m^2/s$) (Fig. 4, figs. S18-S23, and Table S6). The effective diffusion coefficients determined by FRAP reflect the distribution profiles of these proteins - the longer the range, the higher the effective diffusion coefficient. We also discuss alternative interpretations of FRAP experiments (Text S6.4.3) and potential mechanisms underlying differential diffusivity (Text S6.5).

6.2 Experimental setup

A 1 nl injection mix composed of 30 pg of mRNA encoding the GFP fusion proteins with 0.05% phenol red (Sigma) as an injection tracer was injected at the one-cell stage. For FRAP experiments in which the diffusion coefficient of extracellular recombinant GFP in zebrafish embryos was determined, 100 pl of 0.5 mg/ml recombinant GFP protein (BioVision) were injected along with 0.05% phenol red at two to five different locations into the extracellular space of blastula stage embryos, similar to (*14*). Embryos with uniformly distributed fluorescence were selected between sphere and dome stages and mounted as described above (see Text S4 "Measurement of Distribution Profiles").

FRAP experiments were performed using LSM 510 and LSM 7 LIVE confocal microscopes (Zeiss). Two images separated by 10 s were acquired before photobleaching. These images exhibited a nearly homogeneous spatial distribution of fluorescence. Photobleaching in a square region (typically $147.4\,\mu m \times 147.4\,\mu m$, corresponding to approximately 8×8 cells) was performed through the depth of the blastoderm with 100% laser power and 100% transmission. Bleaching was completed in ~5 min. Imaging conditions used for the pre-bleach and post-bleach images were identical. Typically, recovery of fluorescence was monitored every 10 s for

50 min in one medial optical slice in the middle of the embryo. For some experiments with Cyclops-GFP, the time course was extended to 100 min.

No deleterious effects from constant laser scanning were observed during acquisition of the recovery profile. In addition, consecutive FRAP experiments were performed, in which embryos were allowed to recover total fluorescence after bleaching and then were subjected to up to two more bleach/recovery cycles. No major differences in the diffusion coefficients from these consecutive FRAP experiments were observed, indicating that there are no apparent phototoxic effects affecting diffusive processes.

6.3 Image analysis

Image analysis was performed using custom MATLAB scripts. Each FRAP experiment results in $I = I(i, j, t_n)$, a time series of n images of size 512×512 pixels, where i and j represent the pixel coordinates. All images were centered during acquisition. The radius r_{sl} of the blastoderm in the imaged slice did not change by a significant amount. r_{sl} was measured in the first post-bleach image in each experiment ($\sim$230 µm on average, fig. S19). Immediately post-bleaching, the intensity decreases sharply between the unbleached and bleached region (Fig. 4, fig. S18, and figs. S22-S23). This sharp gradient subsequently relaxes as fluorescent molecules diffuse into the bleached volume (Fig. 4, fig S18, and figs. S22-S23). At each time frame, the spatial average intensity in the area A_{win} inside ($\bar{I}_{win}$), A_{out} outside ($\bar{I}_{out}$), and A_{sl} for the entire slice ($\bar{I}_{sl}$) was computed by

$$\begin{aligned}
\bar{I}_{win}(t_n) &= \frac{1}{A_{win}} \sum_{i,j} I_{win}(i, j, t_n) \\
\bar{I}_{out}(t_n) &= \frac{1}{A_{out}} \sum_{i,j} I_{out}(i, j, t_n) \\
\bar{I}_{sl}(t_n) &= \frac{1}{A_{sl}} \sum_{i,j} I_{sl}(i, j, t_n)
\end{aligned}$$

where i and j represent the coordinates of pixels that fall inside of A_{win}, A_{out} and A_{sl}, respectively.

6.4 Mathematical modeling of FRAP experiments

6.4.1 Factors that affect recovery dynamics

The spatial averages $\bar{I}_{win}$, $\bar{I}_{out}$ and $\bar{I}_{sl}$ include both intra- and extracellular regions of the embryo. The observed changes in these spatial averages are the result of multiple physical phenomena that occur in both regions and at their boundaries, including molecular diffusion, cell movement, cell-packing geometry, binding interactions, and clearance and production. In the following, the factors that affect the recovery dynamics and the interpretation of the experiments are discussed. The influence of reversible and irreversible binding on recovery dynamics is discussed in Text S6.4.3 and Text S6.5.

Cell movement: Movement of unbleached cells into the bleached area might contribute to fluorescence recovery. Based on the maximal distance a cell has traveled in the FRAP experiments (t = 3000 s), its maximal mean-square displacement, γ^2, and its diffusion coefficient, D_{cell}, can be estimated using the relationship $\gamma^2 = tD_{\text{cell}}$ (*76*). Non-dividing cells that stayed within the imaging plane over the entire time-course were manually tracked in embryos expressing cytoplasmic GFP to determine their maximal displacement from the origin. It was found that $D_{\text{cell}} = 0.22 \pm 0.05$ $\mu\text{m}^2/\text{s}$ (n = 12 cells from four embryos). The upper bound of the cellular "diffusion coefficient" is therefore much smaller than that of Cyclops-GFP, which had the smallest diffusion coefficient ($0.7\,\mu\text{m}^2/\text{s}$, see below) of all of the constructs that were tested. In addition, FRAP experiments were performed in embryos uniformly expressing cytoplasmic GFP. The resulting "recovery curves" from these experiments were much flatter and lacked the characteristic initial steep recovery observed for the Nodal- and Lefty-GFP fusions. These experiments demonstrate that the contribution of unbleached cells moving into the bleached region is negligible and only affects the edges of the analysis window.

Clearance: Proteins are removed from the diffusible pool with a clearance rate constant k_1. The half-lives of Nodals and Leftys determined using the clearance assay (see Text S5 "Measurement of Clearance Rate Constants") are long (> 90 min) compared to the length of the FRAP experiment (∼50 min). Although it can therefore be assumed that contributions of clearance to the FRAP recovery curves are small, the reaction term k_1 was included in the reaction-diffusion equations to ensure that any effects of clearance were accounted for in the FRAP analysis. Consistent with the idea that effects from clearance are mostly negligible in the case of Nodal and Lefty signals, it was found that the diffusion coefficients were similar regardless of whether k_1 was set to zero or to the value measured in the clearance assay experiments (Table S6).

Production: In the FRAP experiments, mRNA was injected at the one-cell stage and continues to generate protein during the experiment with a production rate k_2. A potential caveat for the analysis of the FRAP experiments is that new production from injected mRNA modulates the recovery profiles. To analyze the magnitude of this effect, protein production was blocked by applying the translation inhibitor cycloheximide. Embryos were injected at the one-cell stage with 60 pg of mRNA encoding the GFP fusion constructs. This is double the amount used for the regular FRAP experiments to ensure that embryos express sufficient levels of protein before translation is blocked. The embryos were incubated in 50 µg/ml cycloheximide (Sigma) in 1% DMSO starting at the 1,000-cell stage, similar to (*81*). Embryos exhibiting uniform fluorescence were mounted at sphere stage in 1% low melting point agarose and covered in embryo medium containing 50 µg/ml cycloheximide to sustain suppression of protein translation. FRAP experiments with cycloheximide-treated embryos resulted in recovery curves similar in shape to the ones determined in untreated embryos but without a linear increase in fluorescence intensities for the entire slice. This indicates that the chemical block of translation was efficient and that production affects recovery curves. To account for production, the reaction term k_2 was included in the subsequent FRAP data analysis model. We found that the diffusion coefficients determined by this model are robust to variations in the freely-fit k_2 term (see Text S6.4.2 "Modeling of the three-dimensional reaction-diffusion system").

Combined effects of production and clearance: It is generally assumed that fast recovery after photobleaching is due to high diffusivity of fluorescent molecules. Indeed, Lefty1-GFP, Lefty2-GFP, secreted GFP, and extracellularly injected recombinant GFP do not show a strong delay in fluorescence recovery in the middle of the bleached window relative to the recovery in the entire bleached region (fig. S23E-G). In this scenario, it is conceivable that diffusivity is very high and clearance and production rates become the major determinants of fluorescence recovery. To determine whether the recovery kinetics of Lefty2-GFP, secreted GFP, and extracellularly injected recombinant GFP could be explained by production and clearance, the predicted half-lives were compared with the independently measured half-lives (see Text S5 "Measurement of Clearance Rate Constants"). Using Equation 29 in Text S6.4.2, the time point τ at which $c(\tau) = \frac{1}{2}(\frac{k_2}{k_1} - c_0) + c_0$ represents the half-life of the protein in this scenario, where c_0 is the initial post-bleach intensity, the ratio k_2/k_1 is the recovery plateau, k_1 is the clearance rate constant and k_2 is the production rate. If recovery were due to production and clearance instead of diffusion, the half-lives for Lefty2-GFP, secreted GFP, and extracellularly injected recombinant GFP would be less than 250 s, i.e. $\tau \approx 4$ min (fig. S23E-G). These ultra-short half-lives are incompatible with the measured half-lives (see Text S5 "Measurement of Clearance Rate Constants") and with the half-life measurements for GFP in an earlier study (*14*). These considerations indicate that the FRAP measurements in our study are based on diffusion and not dominated by production and clearance.

Embryo geometry: Using the simplest assumption for the FRAP experiments, the embryo was initially modeled as a two-dimensional disc (fig. S19), similar to previous geometry simplifications of the zebrafish blastoderm (*14*). In a three-dimensional representation, this two-dimensional geometry simplification would extend to an infinitely long cylinder (fig. S19). However, recovery profiles for species with large diffusivities in a three-dimensional dome-shaped geometry deviate from those generated in a two-dimensional geometry, because the two-dimensional model fails to account for diffusive flux through the imaging plane (figs. S19-S20). The reaction-diffusion system was therefore modeled in a three-dimensional geometry, similar to previous studies (*97, 98*).

Bleach profile: There are small time delays between the end of bleaching and the start of post-bleach imaging in all FRAP experiments presented here. Consequently, recovery has already begun by the time the first post-bleaching image is acquired (fig. S22). Therefore, fitting the data with a model that assumes an initial condition of zero concentration at all points in the bleach window would result in erroneous diffusion coefficient measurements due to a failure to account for this time shift (*99*). To circumvent this issue, the intensity profiles from the first post-bleaching image were directly used as the initial condition for the simulations.

6.4.2 Modeling of the three-dimensional reaction-diffusion system

Description of the reaction-diffusion system: Given the large number of cells ($\gg 100$), we homogenize the embryonic tissue by averaging spatially over both intra- and extracellular regions similar to previous studies (*12, 13*), allowing for the use of a tractable and computationally efficient continuum model of the experimental system.

Effective diffusion, clearance and production were modeled by the linear partial differential equation (PDE)

$$\frac{\partial c}{\partial t} = D\nabla^2 c + R(c) \tag{22}$$

where c is the concentration, D is the effective diffusion coefficient acting on the divergence of the concentration gradient ($\nabla^2 c = \frac{\partial^2 c}{\partial x^2} + \frac{\partial^2 c}{\partial y^2} + \frac{\partial^2 c}{\partial z^2}$), and $R(c)$ may indicate either production, clearance or a combination of the two. Without evidence for higher-order production or clearance reactions (see Text S5 "Measurement of Clearance Rate Constants"), four simple linear models for $R(c)$ were considered with respect to Equation 22:

$$\frac{\partial c}{\partial t} = D\nabla^2 c \qquad \text{(diffusion only)} \tag{23}$$

$$\frac{\partial c}{\partial t} = D\nabla^2 c - k_1 c \qquad \text{(diffusion and clearance)} \tag{24}$$

$$\frac{\partial c}{\partial t} = D\nabla^2 c + k_2 \qquad \text{(diffusion and production)} \tag{25}$$

$$\frac{\partial c}{\partial t} = D\nabla^2 c - k_1 c + k_2 \qquad \text{(diffusion, clearance, and production)} \tag{26}$$

where k_1 is the clearance rate constant and k_2 is the production rate.

Embryo geometry: The average three-dimensional geometry of the blastoderm was approximated by the complement of two spheres of different radii (fig. S19). The smaller sphere had a radius r_b (corresponding to the radius of the embryo), which is determined from the blastoderm radius in the imaged slice r_{sl} and z_{sl} (the depth of the imaged slice with respect to the animal pole) by

$$r_b = \frac{r_{sl}^2 + z_{sl}^2}{2z_{sl}}$$

The depth of the optical slice (z_{sl}) relative to the animal pole was set to 80 µm, given the average slice radius $r_{sl} \approx 230$ µm and the average radius of the embryo $r_b \approx$ 300-400 µm (*100, 101*). The radius of the second sphere r_{b2} was set to a value 10% larger than r_b, and the sphere centers were displaced by the maximal thickness of the blastoderm z_b (figs. S18-S19):

$$z_b = \sqrt{r_{b2}^2 - r_b^2}$$

The bleached domain in the blastoderm was modeled using the dimensions of the bleached window. The intersection of this domain with the optical slice domain Ω_{sl} (in which $\bar{c}_{sl}$ was calculated) defined the bleached analysis subdomain Ω_{win} (in which $\bar{c}_{win}$ was calculated), and the remaining subdomain Ω_{out} (in which $\bar{c}_{out}$ was calculated) was defined by $\Omega_{out} = \Omega_{sl} \setminus \Omega_{win}$.

The initial intensity $I_0 = I(i, j, t_0)$ after photobleaching for each FRAP experiment was used to create an initial condition for the model. The eight-fold symmetry of the optical slice was utilized to compute the average octant from the image by

$$\bar{I}_0(i,j) \quad = \quad \frac{1}{8}\sum_{k=1}^{8} Q_k$$

where $Q_k = Q_k(i, j)$ are the eight octants in the image plane, and the indices i, j are taken with respect to the k-th octant (fig. S19). Assuming uniform photobleaching through the depth of the blastoderm, $\bar{I}_0$ was taken to be the same through the modeled embryo geometry for the regions that were captured in the FRAP experiment. The values of the initial condition in regions of the domain that fall outside of the acquired image were approximated by taking the average concentration in an annulus extending 100 pixels from the edge of the embryo in the imaged slice towards the center of the image. The resulting initial condition (IC) for the model was obtained by the extension of $\bar{I}_0$ in three dimensions, giving

$$c(x, y, z, t_0) = \bar{I}_0(i, j, t_0)$$

The enveloping layer that covers the blastoderm and the yolk syncitial layer between blastoderm and yolk do not allow flux across their boundaries, and the resulting boundary conditions (BC) on the model were

$$\nabla_{\mathbf{n}} c \Big|_{\partial\Omega} = \mathbf{0}$$

where $\nabla_{\mathbf{n}}$ is the gradient operator scaled by the outward normal vector $\mathbf{n}$, and $\partial\Omega$ is the boundary of the embryo.

This geometry, together with the PDE, IC and BC, leads to an inhomogeneous and time-dependent change in concentration in the optical slice after bleaching. Gradients in concentration evolve not only in the plane of the slice but also through the depth of the blastoderm. This configuration enables the model to capture not only the effects of in-plane diffusion and homogeneous reactions considered in previous analysis techniques for FRAP experiments (reviewed in (*95, 96*), but also the effects of diffusive flux through the slice boundaries.

Numerical simulations: The finite element method (FEM) was used to solve the model. All domains of the modeled embryo geometry were discretized using a tetrahedral meshing scheme, and the mesh was refined using several boundary layer elements at the boundary between the bleached window and the rest of the embryo (see Table S4 for meshing and error parameters). The solution at each time step was determined using a sparse LU factorization algorithm (UMFPACK), and the time stepping was computed using a backward Euler step method (Comsol Multiphysics).

In order to fit diffusion coefficients, the solution of the model $c(x, y, z, t)$ needs to be compared with the measured intensity $I(i, j, k, t_n)$ or its spatial averages $\bar{I}_{win}$, $\bar{I}_{out}$, and $\bar{I}_{sl}$. The spatial averages of c for the regions inside ($\bar{c}_{win}$), outside ($\bar{c}_{out}$), in the analysis slice ($\bar{c}_{sl}$), or for the entire blastoderm ($\bar{c}_b$) were calculated by integrating the solution over the subdomains and dividing by their volume. With the assumption of homogenous clearance and production in, and the no-flux BC on the entire blastoderm volume, the spatial average of the changes in the entire blastoderm ($\bar{c}_b$) is only due to the reactions $R(c)$. For the entire blastoderm domain, the diffusion term from Equation 22 can therefore be dropped to give the ordinary differential equation (ODE)

$$\frac{d\bar{c}_b}{dt} = R(\bar{c}_b)$$

Table S4. FEM parameters for numerical simulations of FRAP experiments.

Description	Value
Relative tolerance for solver	1×10^{-2}
Absolute tolerance for solver	1×10^{-3}
Average mesh element size	$\sim$10 µm
Boundary layer mesh thickness	8 µm
Layers in the boundary layer mesh	8
Number of time steps for simulations	4×10^3
Diffusion coefficient used to generate reference curves	10 $\mu m^2/s$

To generate the mesh, a value of 7 was used for the 'hauto' parameter globally in Comsol Multiphysics, which controls the element size in the generated mesh and sets several mesh parameters automatically.

For the three cases where $R \neq 0$, the analytical solutions are

$$\text{clearance only:} \quad \bar{c}_b(t) = c_0 e^{-k_1 t} \qquad (k_1 \neq 0, k_2 = 0) \tag{27}$$

$$\text{production only:} \quad \bar{c}_b(t) = c_0 + k_2 t \qquad (k_1 = 0, k_2 \neq 0) \tag{28}$$

$$\text{clearance and production:} \quad \bar{c}_b(t) = c_0 e^{-k_1 t} - \frac{k_2}{k_1} e^{-k_1 t} + \frac{k_2}{k_1} \qquad (k_1 \neq 0, k_2 \neq 0) \tag{29}$$

where c_0 is determined in each case using the IC.

The spatial averages of I were measured only in the optical slice, however, and therefore $\bar{c}_{sl}(t)$ needs to be compared with $\bar{I}_{sl}(t_n)$. Since I is computed in a volumetric slice, whose upper and lower boundaries are continuous with the rest of the blastoderm, the geometry imparts a non-zero and unequal diffusive flux through the slice boundaries, which results in an average change in concentration within the slice volume (fig. S20). This average concentration change is computed directly from the volume-averaged solution to Equation 23 with $R(c) = 0$, as seen by applying the divergence theorem:

$$\frac{1}{V_{sl}} \int_{\Omega_{sl}} \nabla^2 c_{df} dV = \frac{1}{V_{sl}} \int_{\partial\Omega_{sl}} \nabla_{\mathbf{n}} c_{df} dS = \frac{1}{V_{sl}} \int_{\Omega_{sl}} \frac{\partial c_{df}}{\partial t} dV = k_{df}(t; D)$$

where V_{sl} is the volume of the slice, c_{df} is the concentration resulting from diffusive flux in the slice, Ω_{sl} is the slice domain, $\partial\Omega_{sl}$ is the boundary of the slice, and k_{df} is a volume-averaged time- and diffusion-dependent "production" term due to diffusive flux.

The resulting model for the volume-averaged concentration change in the slice is

$$\frac{d\bar{c}_{sl}}{dt} = R(\bar{c}_{sl}) + k_{df}(t; D)$$

Given the above solutions for the reaction ODEs (Equations 27, 28 and 29), it can be seen that the term k_{df} contributes to the rate of change of the solution exactly the volume-averaged solution to the diffusion-only problem $\bar{c}_{df}(t)$. Subtracting $\bar{c}_{df}(t)$ from $\bar{c}_{sl}$ therefore gives the change in concentration in the optical slice due purely to the reactions.

Non-dimensionalization and scaling: Dimensional analysis of the model results in scaling of a one-parameter family of curves, allowing the solution for any D to be determined given one solution. From Equation 23, the following dimensionless variables were defined:

$$t = T_0\tilde{t}, x = X_0\tilde{x}, c = C_0\tilde{c}$$

The scalings of each variable were established by forming groups with the following parameters:

$$X_0 = r_b, C_0 = c_0, T_0 = \frac{r_b^2}{D}$$

Substituting these groups into Equation 23 and rearranging results in the corresponding dimensionless PDE, BC and IC

$$\begin{aligned} \frac{\partial \tilde{c}}{\partial \tilde{t}} &= \tilde{\nabla}^2\tilde{c} && (\text{in } \tilde{\Omega}) \\ \tilde{\nabla}_{\mathbf{n}}\tilde{c} &= \mathbf{0} && (\text{on } \partial\tilde{\Omega}) \\ \tilde{c} &= \tilde{c}_0 && (\text{at } \tilde{t} = 0) \end{aligned}$$

where $\tilde{c}_0$ is taken from I_0 as described above and normalized to the final time point in the data, and both the IC and BC are independent of the length and time scales of the problem.

The resulting solution $\tilde{c} = \tilde{c}\left(\tilde{x}, \tilde{y}, \tilde{z}, \tilde{t}\right)$ can then be rescaled back into the dimensional solution c for any choice of D and the specific r_b measured for each embryo, importantly noting that the time scales with $\frac{r_b^2}{D}$ (fig. S21). This is done by substituting back in the dimensional variables using the dimensionless groups.

This scaling was utilized to efficiently fit the effective diffusion coefficient without simulation for each choice of D. For each FRAP experiment, a scaling solution was found by FEM using a logarithmic distribution of a sufficiently large number of discrete time steps (4,000). This spacing allows the comparison of the scaled solution c with the measured intensities I by piecewise-linear interpolation of the scaled solution at the time points given by the data.

Combining the numerical "diffusion only" solution with the reactions: The solution in the entire blastoderm $\bar{c}_b$ only differs from the solution in the optical slice $\bar{c}_{sl}$ by the contribution due to the diffusive flux $\bar{c}_{df}$. The solution $\bar{c}_{sl}$ is thus assembled by adding $\bar{c}_b$ and $\bar{c}_{df}$ (fig. S20 and fig. S21), requiring solely the computation of the "diffusion only" model (Equation 23) using FEM, which is then added to the solution for the choice of reaction parameters. Using this approach, the experimental results $\bar{I}_{sl}$, $\bar{I}_{win}$, and $\bar{I}_{out}$ can be directly compared with the simulated results $\bar{c}_{sl}$, $\bar{c}_{win}$, and $\bar{c}_{out}$, respectively.

Data fitting: For each FRAP experiment, the combination of parameters D, k_1 and k_2 was found which minimizes the sum of squared differences (SSD) between the simulations of one of the four reactions models (Equations 23, 24, 25, and 26) and the experimental data. Given the analytical solutions for the reactions (Equations 27, 28, and 29), the diffusive flux only needs to be computed for a given choice of D. The minimization of the SSD over the three possible parameters D, k_1 and k_2 is thus reduced computationally to the solution of a single FEM problem and the computation necessary to perform the minimization steps.

Table S5. Minimization parameters for FRAP data fitting.

Description	Value
Termination tolerance for SSD minimization	1×10^{-6}
Termination tolerance on the function value	1×10^{-6}
Lower bound for D during SSD minimization	1×10^{-3} $\mu m^2/s$
Upper bound for D during SSD minimization	$100\,\mu m^2/s$
Initial guess for D during SSD minimization	$0\,\mu m^2/s$
Lower bound for k_2 during SSD minimization	0 units/s
Upper bound for k_2 during SSD minimization	∞
Initial guess for k_2 during SSD minimization	0 units/s
Lower limit for the equalization factor EQ	0.1
Upper limit for the equalization factor EQ	3.0

To maximize our confidence and to exploit all the available data, the least-squares minimization problem was defined by summing the residuals inside the window with those in the entire optical slice, such that

$$SSD = \sum_n \left(\bar{I}_{win}(t_n) - \bar{c}_{win}(t_n)\right)^2 + \sum_n \left(\bar{I}_{sl}(t_n) - \bar{c}_{sl}(t_n)\right)^2$$

The minimization was performed numerically using a constrained optimization algorithm (Nelder-Mead, MATLAB), which converges on a minimum for a given range of parameters values. Given the approximated uniqueness of the solution to the model (see below), the minimum found by this approach is the global minimum within the bounds of the parameter space up to the propagated determinate and indeterminate error. See Table S5 for fitting constraints and initial parameter value guesses and Table S6 for results from three-dimensional simulations.

Uniqueness of the solution: For the linear reaction and diffusion models considered, the spatial solution at every time point is uniquely determined to within the error bounds of the algorithm for the numerical solution. Given the linearity of the model, linear superposition of the solutions demonstrates the uniqueness of any solution for a particular choice of parameters. Consider two solutions c_1 and c_2, each having a unique set of parameters. Then $c_3 = c_1 - c_2$ is also a solution, and if the two solutions are unique everywhere in space, then their difference is non-zero at every time point. Likewise, since any two solutions having the same parameters must be identical, their difference is zero. Substituting $c_3 = 0$ into the PDE, BC, and IC, it can be seen that there is no initial or boundary data, thus satisfying the PDE trivially for all parameters choices. Likewise, if $c_3 \neq 0$, the PDE, BC, and IC results in a non-zero solution, which can only be satisfied for c_1 and c_2 that have different parameter sets.

Accounting for the immobile fraction and changes in the volume fraction: In most previously reported FRAP experiments, there is a fraction of fluorescent molecules that does not recover after photobleaching. This fraction is referred to as the *immobile fraction* and in

the experiments presented here could be due to bleaching of fluorescence inside cells that only recovers slowly (on a longer time scale than the experiment), or due to long-term occupancy of binding partners that prevent fluorescent molecules from re-populating the area. The presence of such an immobile fraction would lead to a recovery plateau in the experiments that is lower than what is predicted by the homogenous continuum model presented here. Furthermore, the experimental recovery plateau might be different from the simulations due to changes in the extracellular volume fraction ϕ_{ext}. In the present experiments, ϕ_{ext} is on the order of $\sim$0.15 as estimated by the extracellular area fraction for the optical slice, but for any given embryo ϕ_{ext} can increase or decrease over time. Hypothetically, assuming a constant number of molecules in the extracellular space, a decrease in ϕ_{ext} would thus lead to an increased fluorescence intensity, whereas an increase in ϕ_{ext} would lead to a decreased fluorescence intensity. Given the maximal observed change in ϕ_{ext}, the upper boundary is assumed to be $\Delta\phi_{\text{ext}} < 300\%$. The immobile fraction and any changes in the volume fraction (ϕ_{ext}) are accounted for by minimizing the difference between the simulated curve and the experimental data at each iteration with the equalization factor EQ, with $EQ_{\max} = 3$ as the upper limit of the change in ϕ_{ext}, and $EQ_{\min} = 0.1$ as the lower limit for the immobile fraction (Table S5).

Goodness of fit: R^2 values were calculated from the minimizing SSD ($SSD_{\min}$) to assess the goodness of the fits by

$$R^2 = 1 - \frac{SSD_{\min}}{\sum_n \left(\bar{I}_{win}(t_n) - \frac{1}{n} \sum_n \bar{I}_{win}(t_n) \right)^2}$$

6.4.3 Fast diffusion and slow immobilization

We considered alternative interpretations of the FRAP data. It is generally assumed that slow recovery after photobleaching is due to low diffusivity of signaling molecules. However, it is

Table S6. FRAP results from three-dimensional simulations.

Protein	D "diffusion only" ($\mu m^2/s$)	D "diffusion and production" ($\mu m^2/s$)	D "diffusion, production and clearance" ($\mu m^2/s$)	n
Cyclops-GFP	0.7 ± 0.1	0.9 ± 0.1	0.7 ± 0.2	22
Squint-GFP	3.8 ± 0.7	3.8 ± 0.7	3.2 ± 0.5	30
Lefty1-GFP	6.5 ± 0.3	11.6 ± 0.6	11.1 ± 0.6	21
Lefty2-GFP	25.9 ± 9.8	30.0 ± 8.4	18.9 ± 3.0	5
Secreted GFP	33.7 ± 16.8	36.7 ± 16.5	33.9 ± 15.5	5
Recombinant GFP	44.0 ± 8.5	44.0 ± 8.5	37.6 ± 6.9	10

For the model "diffusion, production and clearance", the clearance rate constants (k_1) measured using the clearance assay were used. The k_1 for secreted Dendra2 was used for secreted and recombinant GFP. Recombinant GFP was injected into the extracellular space. Values represent the mean ± standard error of n experiments.

conceivable that FRAP curves could be dominated by slow binding reactions ("trapping model"). In such a "trapping model", also referred to as "diffusion-uncoupled recovery" (reviewed in (*96*)), diffusion across the bleached window is fast but binding reactions are slow. In this model, diffusion initially rapidly equilibrates the concentration gradients in the bleached window followed by slow binding and trapping of the molecules. In this scenario, the observed intensity increase is due to the slow accumulation of bound fluorescent species. In other words, the increase in fluorescence does not reflect diffusion and should thus be spatially uniform in the bleached window. For example, Lander and colleagues have recently argued that the recovery of Dpp-GFP in FRAP experiments is diffusion-uncoupled (*17*). They suggest that the fraction of mobile Dpp-GFP in the wing disc is very low ($< 3\%$) and therefore too dim to contribute to the observed fluorescence recoveries. Instead, the fraction responsible for recovery is thought to be immobilized Dpp-GFP that has slowly accumulated to detectable levels inside cells. In this model, low levels of mobile Dpp-GFP immediately move into the bleach window and fill it uniformly shortly after photobleaching. The fast diffusion of Dpp-GFP ($D \approx 20\,\mu\text{m}^2/\text{s}$) would not be detected, and the observed fluorescence recovery would be due to the slow accumulation of immobilized Dpp-GFP reflecting binding and degradation kinetics. Lander and colleagues argue that the small diffusion coefficient ($D \approx 0.1\,\mu\text{m}^2/\text{s}$) deduced from FRAP data in previous studies (*12, 13*) therefore does not reflect the mobility of Dpp-GFP but rather binding and degradation kinetics.

To determine whether our FRAP recovery curves may be dominated by fast diffusion and slow binding kinetics, we performed simulations by considering the following reaction:

$$C + R \underset{k_{\text{off}}}{\overset{k_{\text{on}}}{\rightleftharpoons}} \overline{CR}$$

where the diffusible signaling molecule C and the immobile binding molecule R are transformed to the immobilized complex $\overline{CR}$ with the on-rate constant k_{on}. The immobilized complex $\overline{CR}$ can dissociate back into C and R with an off-rate k_{off}. The equations describing the full system including diffusion, binding, unbinding, clearance and production are thus

$$\frac{\partial C}{\partial t} = D\nabla^2 C - k_{\text{on}} CR + k_{\text{off}}\overline{CR} - k_{\text{Clear}} C + k_{\text{Prod}} \tag{30}$$

$$\frac{\partial R}{\partial t} = -k_{\text{on}} CR + k_{\text{off}}\overline{CR} \tag{31}$$

$$\frac{\partial \overline{CR}}{\partial t} = k_{\text{on}} CR - k_{\text{off}}\overline{CR} - k_{\text{Clear}}\overline{CR} \tag{32}$$

with a clearance rate constant k_{Clear} acting on both free C and bound $\overline{CR}$, and a production rate k_{Prod} that continuously generates more of the signaling molecule C.

FRAP experiments were modeled in two dimensions using a circular domain with radius $r_{\text{sl}} = 300\,\mu\text{m}$ and a bleach window with $h_{\text{win}} = 147.4\,\mu\text{m}$. A smaller analysis window with $h_{\text{small}} = 100\,\mu\text{m}$ was nested within the bleach window, similar to the analysis windows used to analyze the FRAP experiments. The initial concentration C outside of the bleach window was set to 0.05 nM and the concentration within the bleach and smaller nested windows to 0 nM at $t = 0$. Note that these concentrations were chosen for convenience, but that these are

not important for the simulation conclusions and do not have to be on the same order *in vivo*. The initial concentration of the bound complex $\overline{CR}$ outside of the bleach window was set to 0.95 nM to reflect that most signaling molecules are bound in this model, and the concentration within the bleach and smaller nested windows was set to 0 nM at $t = 0$ In order to make the concentration of R not limiting for binding, R was set to 1000 nM at $t = 0$. FRAP experiments were simulated for 3000 s and spatial averages of C, $\overline{CR}$ or $C + \overline{CR}$ calculated in the bleach and smaller nested windows.

We then measured the average intensity during recovery in our experimental data in a smaller window within the bleach window and compared it to the recovery measured in the entire window (fig. S23). In contrast to what would be expected if recovery was diffusion-uncoupled (fig. S24), recovery in the small window was delayed compared to recovery in the large window for Nodal-GFP fusions. Our results are consistent with diffusion-coupled recovery, in which molecules must first move through the edge of the bleached window before reaching the middle, causing a delay in recovery in the center of the window (fig. S25; see Text S6.5 "Potential mechanisms underlying differential effective diffusivity" below for further discussion).

Another possibility is that recovery dynamics are dominated by fast diffusion and irreversible binding. To test whether irreversible binding could explain our FRAP data, we performed simulations with a modification of the system described by Equations 30, 31 and 32 with $k_{\text{off}} = 0$. This prevents the dissociation of the complex $\overline{CR}$ into C and R and therefore permanently immobilizes the ligand. In this case, free signaling molecules are permanently immobilized, and the recovery curve almost exclusively reflects the spatially homogenous production and degradation kinetics. This behavior is not consistent with our FRAP measurements (fig. S23). Therefore, fast diffusion in combination with fast irreversible binding is incompatible with the recovery curves that we observe in our FRAP experiments.

6.5 Potential mechanisms underlying differential effective diffusivity

Our FRAP experiments reveal that Nodals have lower effective diffusion coefficients than Leftys. However, Nodals and Leftys have similar molecular weights (fig. S2 and fig. S6) and based on the Einstein-Stokes equation (Equation 19) would therefore be expected to have similar diffusion properties. We speculate that the differences in diffusivities are caused by differential binding interactions with molecules in the extracellular space. For example, Nodals may bind extracellular molecules or receptors localized to cell surfaces. Far from cell surfaces, in the absence of such binding partners, Nodals may diffuse freely on very short length- and time-scales with a high diffusion coefficient. However, continuous binding and unbinding near the cell surface could lead to a global retardation in mobility resulting in slow *effective* diffusion compared to Leftys, which may not bind with such high affinity. In contrast to the interactions discussed above in Text S6.4.3, these interactions have to be reversible and fast relative to diffusion. Below, we review the definition of "effective diffusion" and simulate the effects of reversible binding on fluorescence recovery curves. We find that our FRAP data can be explained by models in which fast reversible binding combined with effects from the tissue architecture leads to a decrease in global diffusivity.

It has been shown mathematically (*102*) and experimentally (*103*) that reversible binding can influence the effective diffusivity of a molecule. The concept of effective diffusivity incorpo-

rating reversible binding reactions (*102*) is outlined in the following. Consider the reaction of species c forming the complex c_{bound} with a forward reaction rate of k_{on} and a reverse reaction rate of k_{off}

$$c \underset{k_{\text{off}}}{\overset{k_{\text{on}}}{\rightleftharpoons}} c_{\text{bound}}$$

Using the law of mass action, the change in concentration of the complex c_{bound} can be determined as

$$\frac{dc_{\text{bound}}}{dt} = k_{\text{on}}c - k_{\text{off}}c_{\text{bound}} \tag{33}$$

Including diffusive processes, the change in the concentration of species c can be described as

$$\frac{\partial c}{\partial t} = D\nabla^2 c - k_{\text{on}}c + k_{\text{off}}c_{\text{bound}} \tag{34}$$

Solving Equation 33 for c_{bound}, the following equation is obtained

$$c_{\text{bound}} = \frac{1}{k_{\text{off}}}\left(k_{\text{on}}c - \frac{dc_{\text{bound}}}{dt}\right)$$

and by inserting this expression into Equation 34 therefore

$$\frac{\partial c}{\partial t} = D\nabla^2 c - k_{\text{on}}c + k_{\text{off}}c_{\text{bound}} = D\nabla^2 c - \frac{dc_{\text{bound}}}{dt} \tag{35}$$

If $k_{on}c \gg \frac{dc_{\text{bound}}}{dt}$, binding is almost instantaneous and therefore

$$c_{\text{bound}} = \frac{1}{k_{\text{off}}}\left(k_{\text{on}}c - \frac{dc_{\text{bound}}}{dt}\right) \approx \frac{k_{\text{on}}}{k_{\text{off}}}c = \kappa c \tag{36}$$

where κ is the dissociation constant. In other words, the concentration of the complex c_{bound} is directly proportional to the concentration of the free species c. This is the case if the binding reaction is fast compared to diffusion, yielding a local equilibrium between c and c_{bound}. Inserting the time derivative of Equation 36 into Equation 35, the change in concentration over time by diffusion and reaction (i.e. fast reversible binding) can be described as

$$\frac{\partial c}{\partial t} = D\nabla^2 c - \kappa\frac{dc}{dt} = \frac{D}{\kappa + 1}\nabla^2 c = D_{\text{eff}}\nabla^2 c \tag{37}$$

with D_{eff} as the reaction-dependent effective diffusion coefficient.

To further illustrate that molecules with similar free, molecular diffusion coefficients can have different effective diffusion coefficients, we performed simulations that include free diffusion and reversible binding reactions. FRAP experiments were modeled based on Equations 30, 31 and 32 as described in Text S6.4.3, but with fast reversible binding kinetics compared to diffusion. The on-rate constant k_{on} was set to 0.001/(nM s), similar to the on-rate constants that have been measured for BMP molecules (*104*). Diffusion models assuming a high free diffusion coefficient in combination with fast reversible binding kinetics yield a smaller effective diffusion coefficient and reflect our experimental observations (fig. S23 and fig. S25). In these homogenized models,

most of the ligand would be bound at any given time point. Our data is therefore consistent with reversible binding reactions that transform local free diffusion to global effective diffusion.

It has been shown mathematically (*103, 105, 106*) and experimentally (*107*) that the tissue architecture (e.g. presence of cells, small extracellular volume fraction) can further decrease the effective diffusivity of a molecule, since molecules have to travel around cells and potentially through transient cavities in cellular membranes. The exact fold difference between geometrically hindered and unhindered diffusion varies in the literature based on the geometry used for simulations, but conservative estimates indicate an approximately two- to three-fold decrease in diffusivity in the presence of cells compared to unhindered diffusion in aqueous solution (*103, 106*). Importantly, effective diffusion coefficients have been measured experimentally for fluorescent dextran molecules (*107*). These experiments show that, on average, effective diffusivities in cellular environments (such as the densely packed brain) may be reduced by four-fold compared to diffusion in aqueous solution. Indeed, in local measurements on short length- (femtoliter) and time-scales (seconds) using Fluorescence Correlation Spectroscopy (FCS), Yu et al. (*14*) found a diffusion coefficient for extracellular GFP in zebrafish embryos that is similar to the diffusion coefficient of GFP in water but approximately two times greater than the one measured with FRAP in our study ($D_{\mathrm{FCS}} = 86\,\mu\mathrm{m}^2/\mathrm{s}$ (*14*), $D_{\mathrm{FRAP}} = 34\,\mu\mathrm{m}^2/\mathrm{s}$). These measurements suggest that extracellular FCS measurements predominantly detect freely diffusing molecules whereas FRAP measurements capture longer-range movements in the context of a tissue, where effective diffusivity is influenced by cell packing, cell movement, viscous effects at cell surfaces as well as potential binding effects exerted by extracellular molecules. As Grimm et al. (*88*) have argued: "[...] *the temporal window of observation can drastically influence an experimentally determined diffusion coefficient because the effective movement of a probe can include a mixture of mechanistically distinct transport events. On short time scales, such as a few seconds, measurements will reflect the movement of proteins within a cellular compartment. Over the course of minutes, measurements will include the effective diffusion within a compartment together with shuttling of molecules between neighbouring compartments. On the order of hours, molecular transport results from a number of events, including diffusion inside compartments* [...] *Moreover, a given time scale is intrinsically linked to a corresponding spatial scale, where short time scales correspond to short spatial scales and long time scales correspond to large spatial scales.*".

As a preliminary test of this scenario, we performed FCS measurements and found similarly high diffusion coefficients for Nodal- and Lefty-GFP fusion proteins ($D \approx 40\,\mu\mathrm{m}^2/\mathrm{s}$; Müller, Yu, Schier and Brand, unpublished results). These results and considerations of effective diffusion support the idea that FCS and FRAP measure different aspects of signal dispersal. FCS measures fluorescence fluctuations in very small volumes that likely reflect local unhindered diffusion within a small extracellular pool. Conversely, FRAP assays allow the measurement of the global *effective* diffusivity over large volumes in a field covering multiple cell lengths. FRAP is therefore better suited than FCS to measure effective diffusion over the long temporal and spatial scales that are relevant for gradient formation and signal dispersal in embryonic tissues. Our simulations show that the differences in diffusion coefficients measured by FRAP and FCS can be explained by tortuosity and reversible binding (fig. S25).

7 Modeling of the Distribution Profiles

7.1 Rationale and summary

The quantitative biophysical analyses in the previous sections showed that Nodal and Lefty signals have different diffusivities (Fig. 4 and fig. S18), whereas their clearance rate constants are relatively similar (Fig. 3, figs. S12-S13, and Table S3). In contrast to previous studies (*12, 13, 26, 88*) that deduced clearance rate constants from diffusion coefficients and distribution profiles, our independent measurements of diffusion, clearance and distribution enabled us to test the validity of our approaches. We performed mathematical simulations in three-dimensional geometries using the experimentally determined values. The observed and predicted shapes of the distribution profiles were in good agreement, suggesting that the different diffusivities of Nodal and Lefty signals can largely account for their distinct distribution profiles and activity ranges (fig. S26).

7.2 Mathematical modeling

The geometry of the blastoderm was approximated by the complement of two spheres, one of which has a radius of 304 µm, and the second has a radius that is 10% larger than the other (similar to the geometry presented in Text S6 "Measurement of Effective Diffusion Coefficients"). The centers of the two spheres were displaced by $z_b = 96\,\mu\text{m}$, the maximum thickness of the blastoderm (figs. S18-S19). In a small columnar subdomain placed off-center (to mimic actual experiments), a signal source region with continuous boundaries is defined by a non-zero, constant and homogeneous production rate k_2. Outside the source subdomain k_2 is zero (fig. S26). Excluding this difference, the source and surrounding blastoderm (target field) are assumed to otherwise behave similarly. The chemical species of interest diffuses with a diffusion coefficient D and is cleared with a clearance rate constant k_1. In the target field, there is no *de novo* production, but molecules diffuse and are cleared uniformly with the same dynamics as in the source. The model is thus governed by the PDE

$$\frac{\partial c}{\partial t} = D\nabla^2 c - k_1 c + \delta_s k_2$$

with

$$\delta_s = \begin{cases} 1 & \text{in the source} \\ 0 & \text{otherwise} \end{cases}$$

The initial condition (IC) is chosen to be zero and homogeneous in the entire blastoderm, approximating the moment at which the source is activated (by transplantation in the experiment) and production, clearance, and diffusion begin

$$c(x, y, z, t_0) = 0$$

The enveloping layer that covers the blastoderm and the yolk syncitial layer between blastoderm and yolk do not allow flux across the boundaries of the blastoderm domain $\partial\Omega$, and the resulting

boundary conditions (BC) on the model are

$$\nabla_{\mathbf{n}} c\Big|_{\partial\Omega} = \mathbf{0}$$

Numerical solution of reaction and diffusion in embryo geometry: The model was solved in the described geometry using the Finite Element Method (FEM) using Comsol Multiphysics operated under the control of MATLAB scripts. All domains were discretized using a tetrahedral meshing scheme (see Table S7 for meshing and error parameters). The spatial solution at each time step was determined using UMFPACK, and the transient solution was determined using the backward Euler step method.

The distribution profile data $\bar{I}(x_n)$ was compared with the model $\bar{c}(x)$ by performing steps analogous to those taken during image analysis, as follows: The solution resulting from the FEM was evaluated at the nodes of 5 regular planar grids of dimensions 512×512 pixels, having DX steps between each node in both the x- and y-directions, and located at 5 µm intervals centered about the distance from the animal pole to the middle of the z-stack. DX was chosen to be sufficiently small such that there was no difference larger than the absolute (element-wise) tolerance of the FEM solution at any point in space between the solution evaluated on this grid, and the same solution evaluated on a grid of higher resolution. The grid was constructed such that the nodes were placed exactly at the boundaries of the source and the boundary of the embryo. The maximum intensity projection of the 5 gridded slices was computed, and the profiles were extracted by taking only the values of the solution located on the line of pixels at $y = 0$ (centered in the source in the y-direction). These curves were normalized to the value at the source boundary, and then were interpolated piecewise-linearly onto a one-dimensional grid whose node locations matches the data points of $\bar{I}(x_n)$. The resulting solution $\bar{c}(x_n)$ at each time allows for comparison directly with the data, as well as accurately accounting for the diffusive effects conferred by the real blastoderm geometry.

7.3 Data fitting

Parameter space search: Since k_2 is the only term that has units of concentration, all curves scale relative to it and the absolute values of k_2 are not important. All space-dependent concentrations were therefore normalized to the value at the source boundary. A logarithmically spaced parameter grid of 50×50 values for D and k_1 was screened (Table S7). To identify the best D and k_1 that describe the observed distribution profiles $\bar{I}(x_n)$, either D or k_1 were fixed to the values in the parameter space closest to the experimentally determined values, and the parameter space was searched for the value of the other parameter that minimized the sum of squared differences (SSD) between the simulations $\bar{c}(x_n)$ and the experimental data sets $\bar{I}(x_n)$ using

$$SSD = \sum_n \left(\bar{I}(x_n) - \bar{c}(x_n)\right)^2$$

as shown in fig. S26.

To determine whether simulations using both our experimentally determined D and k_1 values generate gradients that are similar to those we observed *in vivo*, both D and k_1 were fixed

Table S7. FEM parameters for numerical simulations of distribution profiles.

Description	Value
Distance from origin to center of source	80 µm
Distance from animal pole to center of z-stack	50 µm
Slice radius	167 µm
Source radius	40 µm
Slice thickness	20 µm
Relative tolerance for spatial solver	1×10^{-6}
Absolute tolerance for spatial solver	1×10^{-7}
Average mesh element size	∼10 µm
Maximum element size at the source boundary	20 µm
Grid spatial resolution DX	100
Lower bound for D in parameter grid	0.1 $\mu m^2/s$
Upper bound for D in parameter grid	50 $\mu m^2/s$
Lower bound for k_1 in parameter grid	1×10^{-5}/s
Upper bound for k_1 in parameter grid	5×10^{-4}/s

To generate the mesh, a value of 7 was used for 'hauto' globally in Comsol Multiphysics, which controls the element size in the generated mesh and sets several mesh parameters automatically.

to the experimentally determined values and the resulting curve overlaid onto the experimentally measured gradient data (fig. S26). Curves generated in this way fall within the error of the measured gradient data, supporting the idea that the distribution shapes are governed by diffusion and clearance.

Goodness of fit: To assess the goodness of the fits, R^2 values were calculated from the minimizing SSD ($SSD_{\min}$) by

$$R^2 = 1 - \frac{SSD_{\min}}{\sum_n \left(\bar{I}(x_n) - \frac{1}{n} \sum_n \bar{I}(x_n) \right)^2}$$

8 Comparison of the Nodal/Lefty System to Other Reaction-Diffusion Systems

Summary

Diffusion-driven instabilities form the basis of reaction-diffusion systems (*1*). It has been shown mathematically that a higher diffusivity of the inhibitor compared to the activator is a necessary condition for pattern formation (*32*). However, clearance of activator and inhibitor can also affect the pattern formation probability (see Text S1 "Influence of Clearance and Diffusion on Pattern Formation in Reaction-Diffusion Systems"). The ratios of diffusion coefficients and clearance rates ($d = D/k_1$) between activators and inhibitors ($\Re = d_{\text{inhibitor}}/d_{\text{activator}}$ (*27*)) provide a convenient measure to compare different patterning systems. Based on mathematical modeling, it has been suggested that the inhibitor in reaction-diffusion systems must have at least a six-fold higher normalized diffusivity than the activator in order for pattern formation to occur (*27*). In the following, we summarize reaction-diffusion modeling studies and compare the predicted $\Re$ values to our $\Re_{\text{Lefty/Nodal}}$. All models have values $\Re \gg 6$. Intriguingly, the experimentally determined $\Re_{\text{Lefty/Nodal}}$ is approximately 14.

In the following, we describe previous biological and chemical studies of reaction-diffusion models. In Table S8, we list diffusion coefficients and k_1 values used in these studies, as well as the average values we determined experimentally for Nodals and Leftys. In each system, the difference between $d_{\text{activator}}$ and $d_{\text{inhibitor}}$ is caused by either differences in diffusivity or differences in clearance. Note that in all systems except for the zebrafish Nodal/Lefty patterning system (this study), the parameter values have not been experimentally determined.

***Hydra* patterning:** The freshwater polyp *Hydra* is a classical model system for spontaneous pattern formation due to its capability to regenerate and to form an organism even after dissociation into single cells. Pattern formation in *Hydra* was modeled by Meinhardt and Gierer in 1972, assuming an inhibitor that is 15 times more diffusive than the activator (*2*). The greater than 10-fold difference in activator and inhibitor ranges originally postulated was later experimentally confirmed in *Hydra* aggregates (*108*), but diffusion and clearance have not been directly measured.

Mouse left-right patterning: In the reaction-diffusion models for left-right patterning, the Nodal/Lefty system amplifies a small bias in differential gene expression between the left and right sides of the embryo. In this system, the inhibitor Lefty has been modeled as two times more diffusive and five times more rapidly cleared than the activator Nodal (*16*).

Patterning of zebrafish stripes: Zebrafish stripe formation was modeled as a reaction-diffusion system with an activator and an inhibitor of unknown identity. In this system, differential diffusivity is the major contributor to differences between $d_{\text{inhibitor}}$ and $d_{\text{activator}}$ (*29*). A recent study has suggested contact-dependent cell depolarization and repulsive movement of

pigment cells as a mechanism to achieve the short-range interaction, but the details remain to be determined (*109*).

Patterning of angelfish stripes: The continually changing patterns of stripes on angelfish skin were modeled as a reaction-diffusion system with an activator and an inhibitor of unknown identity. In this system, differential diffusivity contributes to differences between $d_{\text{inhibitor}}$ and $d_{\text{activator}}$ more than differential clearance (*28*).

Patterning of mouse hair follicle spacing: Wnt was suggested to function as a short-range activator and Dkk as a long-range feedback inhibitor to pattern the spacing of murine hair follicles (*8*). In this system, differential diffusivity contributes to differences between $d_{\text{inhibitor}}$ and $d_{\text{activator}}$ slightly more than differential clearance.

Limb skeletal patterning: Vertebrate limb skeletogenesis is one of the longest-standing candidates for patterning by a reaction-diffusion mechanism. In a study of limb bud precartilage condensation size and spacing, a value of $\Re_{\text{inhibitor/activator}} = 9$ best reproduces the experimental measurements (*38*).

Chlorite/iodide malonic acid system: The chemical iodide-chlorite-malonic acid system can generate Turing patterns (*30*). In this system, a ∼15-fold higher diffusivity of inhibitor over activator was postulated ($\Re_{\text{inhibitor/activator}} = 15$, assuming that iodide and chlorite have approximately similar reaction-independent half-lives). Pattern formation is thought to be achieved by the introduction of a matrix that binds to and hinders the diffusion of the activator, but not the inhibitor. It is tempting to speculate that interactions with the extracellular matrix also generate the differences in the diffusivities of Nodal and Lefty signals during embryogenesis.

Table S8. Parameter values used in reaction-diffusion models.

System	Units	D_a	D_i	k_a	k_i	$\Re$	Reference
Hydra patterning	dimensionless	0.03	0.45	0.0035	0.0045	12	(*2*)
Mouse left-right patterning	dimensionless	20	40	0.5	0.1	10	(*16*)
Patterning of zebrafish stripes	dimensionless	0.01	0.2	1.2	1.0	24	(*29*)
Patterning of angelfish stripes	dimensionless	0.007	0.1	0.03	0.06	7	(*28*)
Patterning of mouse hair follicle spacing	arbitrary	0.005	0.2	0.005	0.015	13	(*8*)
Limb skeletal patterning	D: pixels/iteration k: dimensionless	30	120	0.4615	n.a.	9	(*38*)
Chlorite/iodide malonic acid system	D: $\mu m^2/s$	50	750	n.a.	n.a.	15	(*30*)
Zebrafish Nodal/Lefty patterning system*	D: $\mu m^2/s$ k: 1/s	2	15	0.00011	0.00006	14	this work

With the exception of zebrafish Nodal and Lefty signals, none of the diffusion coefficients and clearance rates were experimentally measured.
The subscripts a and i indicate activator and inhibitor, respectively.
D represents the diffusion coefficient, and k represents the clearance rate constant.
*D_a: mean of Cyclops and Squint D values; D_i: mean of Lefty1 and Lefty2 D values; k_a: mean of Cyclops and Squint k_1 values; k_i: mean of Lefty1 and Lefty2 k_1 values.

9 List of Frequently Used Abbreviations and Variables

Name	Description
Abbreviations	
BC	Boundary condition
FCS	Fluorescence correlation spectroscopy
FEM	Finite element method
FRAP	Fluorescence recovery after photobleaching
IC	Initial condition
ODE	Ordinary differential equation
PDE	Partial differential equation
ROI	Region of interest
SSD	Sum of squared differences
Variables	
A	Area
c	Concentration
D	Diffusion coefficient
EQ	Equalization factor
I	Intensity
κ	Dissociation constant
k_1	Clearance rate constant
k_2	Production rate
Ω	Domain
$\partial\Omega$	Domain boundary
Φ	Volume or area fraction
r	Radius
τ	Half-life
V	Volume
z	Depth
Variable subscripts	
b	Blastoderm
df	Diffusive flux
ext	Extracellular
int	Intracellular
out	Outside of bleached window
$post$	After photoconversion or bleaching
pre	Before photoconversion or bleaching
sl	Entire optical slice
win	Inside of bleached window

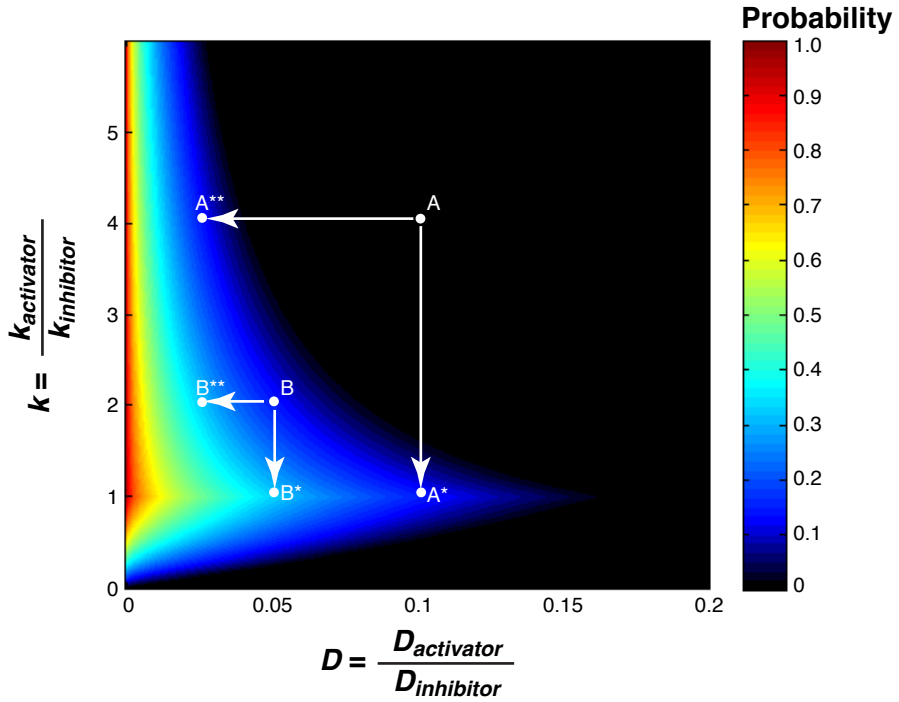

Figure S1. Influence of relative clearance and diffusivity on pattern formation. Parameter space exploration in the Meinhardt-Gierer model (see Text S1 for details). The ability of the Meinhardt-Gierer reaction-diffusion system to form patterns was tested by evaluating the four conditions in Equations 15-18 (Text S1) over a range of values for *D*, *k* and σ (0-1) using linearly spaced sampling with 1,000 values for each parameter. The parameter space was collapsed along σ by calculating the fraction of parameter combinations that satisfied all four conditions. This fraction reflects the probability that pattern formation occurs for the given values of *D* and *k*. The relative diffusivities and clearance of activators and inhibitors affect the probability that a reaction-diffusion system will generate patterns. The probability of patterning increases as *k* approaches 1 and as *D* approaches 0. For example, no patterning will occur at position A; however, decreasing either *D* (resulting in A**) or *k* (resulting in A*) by a factor of four generates systems capable of forming patterns with identical probabilities. Similarly, the probability of patterning can be increased to the same extent for a system that is already capable of pattern formation (B) by decreasing *D* (resulting in B**) or *k* (resulting in B*) by a factor of two. Note that this is one of many reaction-diffusion systems, and the domains in parameter space in which patterns are obtained depend on the equations that describe the reactions (Text S1).

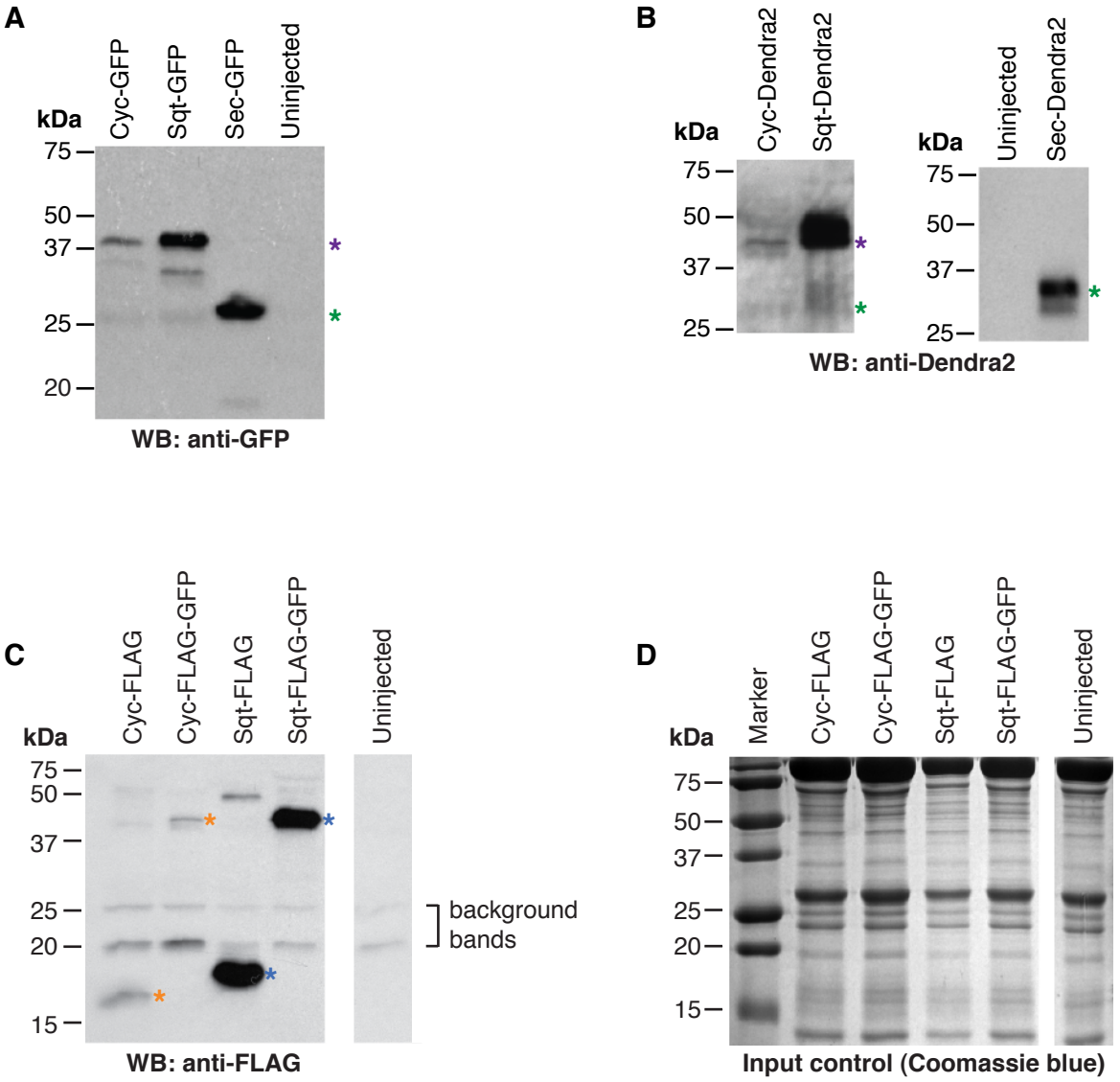

Figure S2. Processing of tagged Nodal signals. (**A-B**) Detection of extracellular fusion proteins by western blot. Embryos were injected with amounts of mRNA encoding Cyclops- (Cyc), Squint- (Sqt), or secreted (Sec) GFP or Dendra2 fusion proteins equimolar to 250 pg Squint-GFP at the one- to two-cell stage (Cyclops-GFP/Dendra2: 284 pg, Squint-GFP/Dendra2: 250 pg, Secreted GFP/Dendra2: 209 pg) and deyolked and dissociated at late blastula stages (Text S3). The extracellularly enriched fraction was probed for the presence of GFP or Dendra2 by immunoblotting with anti-GFP or anti-Dendra2 antibodies. For each blot the position of marker bands of known molecular weight (kDa) is indicated. Asterisks denote the location of the mature processed Nodal fusion proteins (purple) as well as the free fluorescent proteins (green). (**C**) Embryos at the one- to two-cell stage were injected with mRNA encoding FLAG-tagged and FLAG-GFP constructs at equimolar amounts for each protein species (Cyclops-FLAG: 360 pg, Cyclops-FLAG-GFP: 500 pg, Squint-FLAG: 85 pg, Squint-FLAG-GFP: 125 pg). The mature Cyclops fusions are indicated with orange asterisks; the mature Squint fusions are indicated with blue asterisks. The FLAG-GFP-tagged proteins are present at similar levels as the FLAG-tagged proteins. (**D**) Input control for (C). Total protein was stained with Coomassie blue.

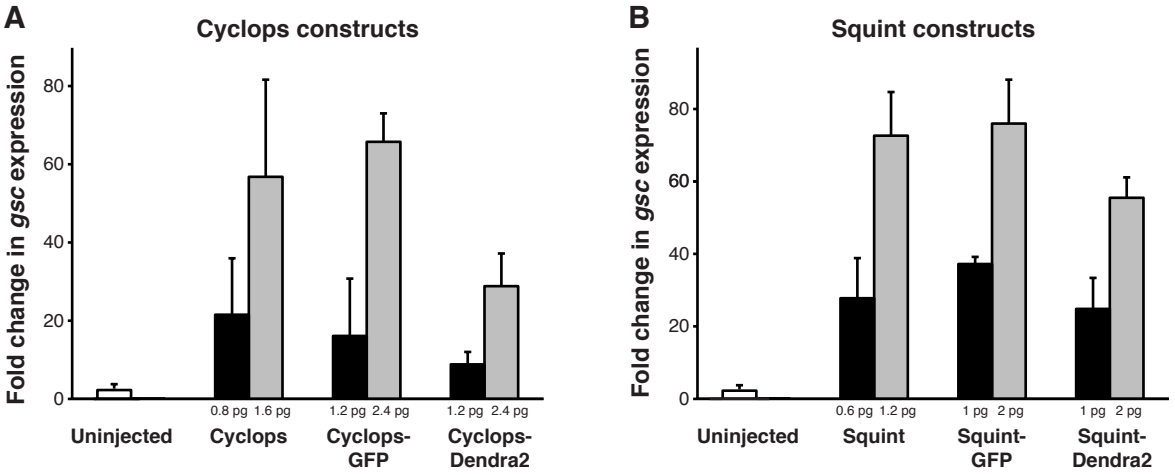

Figure S3. Quantitative reverse transcription PCR (qRT-PCR) to assess Nodal fusion construct activity. Embryos at the one-cell stage were injected with two different amounts of mRNA encoding the indicated constructs and collected when uninjected siblings reached 50% epiboly (Text S3). Fold increase in expression of the Nodal target gene *goosecoid* (*gsc*) compared to uninjected embryos was determined by qRT-PCR and is shown for embryos injected with mRNA encoding tagged or untagged versions of Cyclops (**A**) or Squint (**B**). Black and gray bars, respectively, represent results from embryos injected with equimolar amounts of mRNA. The zebrafish elongation factor *eF1*α was used as a normalization control. Error bars indicate standard deviation.

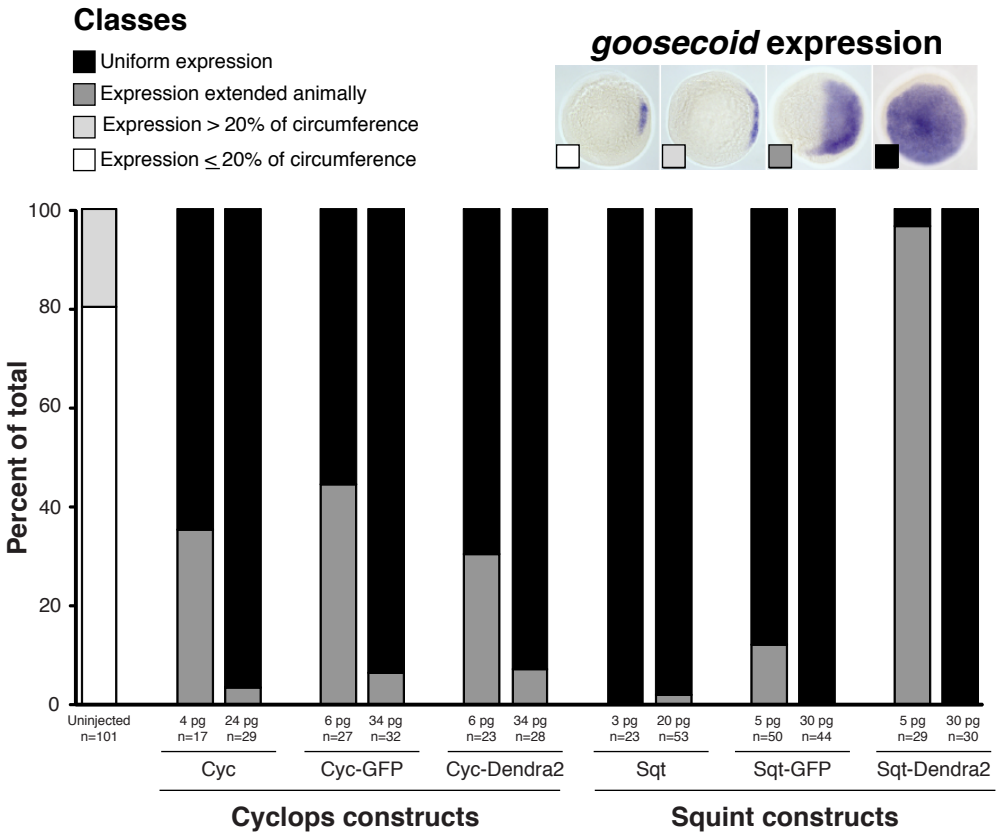

Figure S4. *In situ* hybridization to assess Nodal fusion construct activity. Embryos at the one-cell stage were injected with different amounts of mRNA encoding the indicated constructs equimolar to the untagged constructs and fixed when uninjected sibling embryos reached 50% epiboly (Text S3). Different amounts of mRNA were injected in order to assess dose-dependent activation of the Nodal target gene *goosecoid* (*gsc*) using *in situ* hybridization. Nodal-GFP and -Dendra2 fusion proteins are biologically active. Embryos were scored according to the indicated classes. n indicates the number of embryos analyzed.

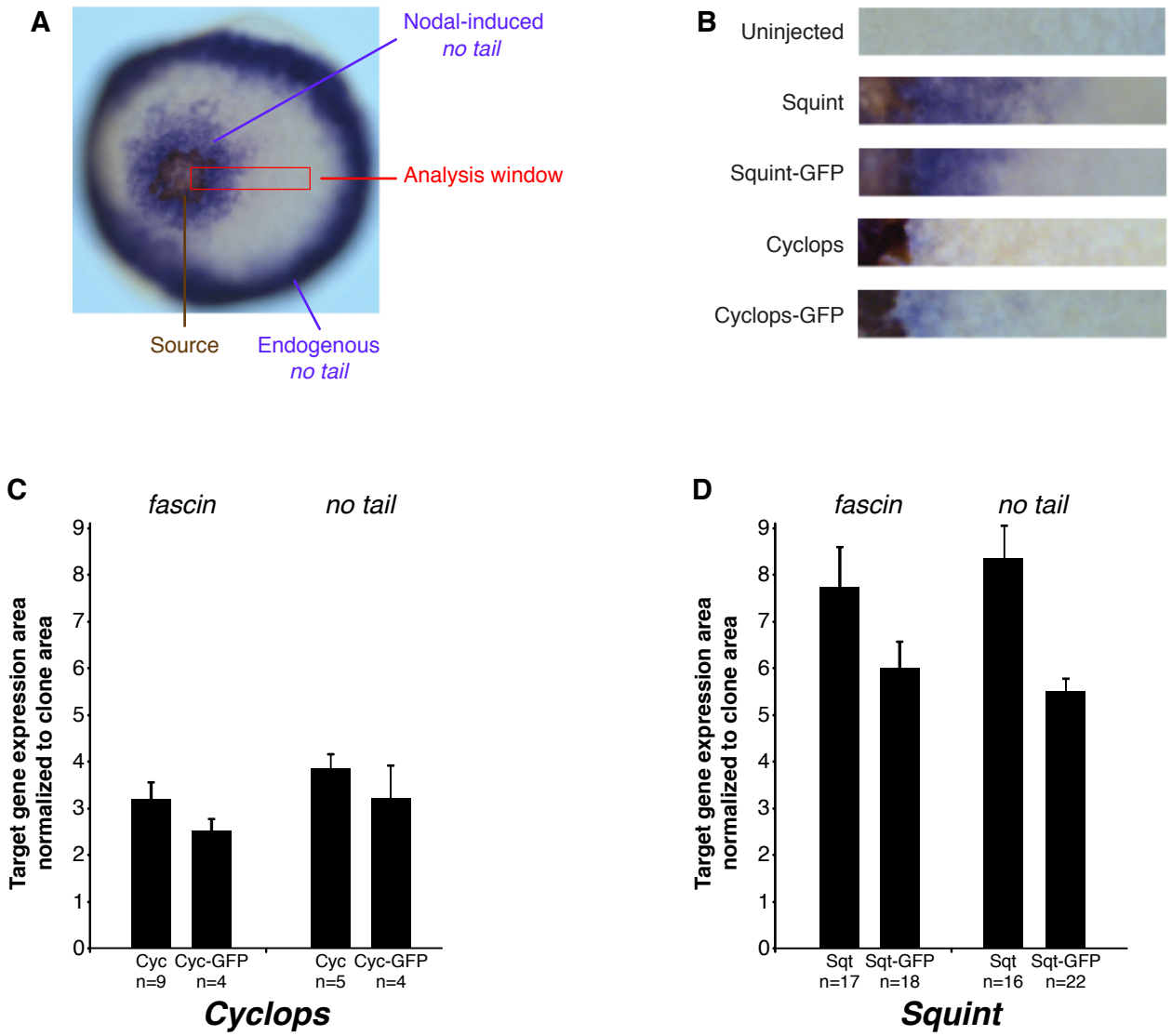

Figure S5. Tagged and untagged Nodal signals have similar activity ranges. To assess the range of Nodal constructs, donor embryos were injected with equimolar amounts of mRNA encoding tagged and untagged constructs (Cyclops: 204 pg; Cyclops-GFP: 284 pg; Squint: 175 pg; Squint-GFP: 250 pg) (Text S3). At late blastula stages, approximately 40 cells (brown, marked by the presence of the injection tracer biotinylated dextran) were transplanted into the animal pole of wildtype hosts. Embryos were fixed one hour after transplantation and processed for *in situ* hybridization using probes against the Nodal target genes *fascin* or *no tail* (blue). (**A**) Representative embryo used to assess the range of Nodal constructs. Blue: *no tail* expression, brown: transplanted cells, red: analysis window. (**B**) Overview of activity ranges. (**C-D**) Quantification of the activity range of Nodal constructs. *In situ* hybridization was used to determine the area around the clone in which the Nodal target genes *fascin* and *no tail* were expressed. The induced area was divided by the area of the clone (as assessed by staining for the injection tracer biotinylated dextran) to normalize for differences in clone size between embryos. Error bars represent standard error. n indicates the number of embryos analyzed.

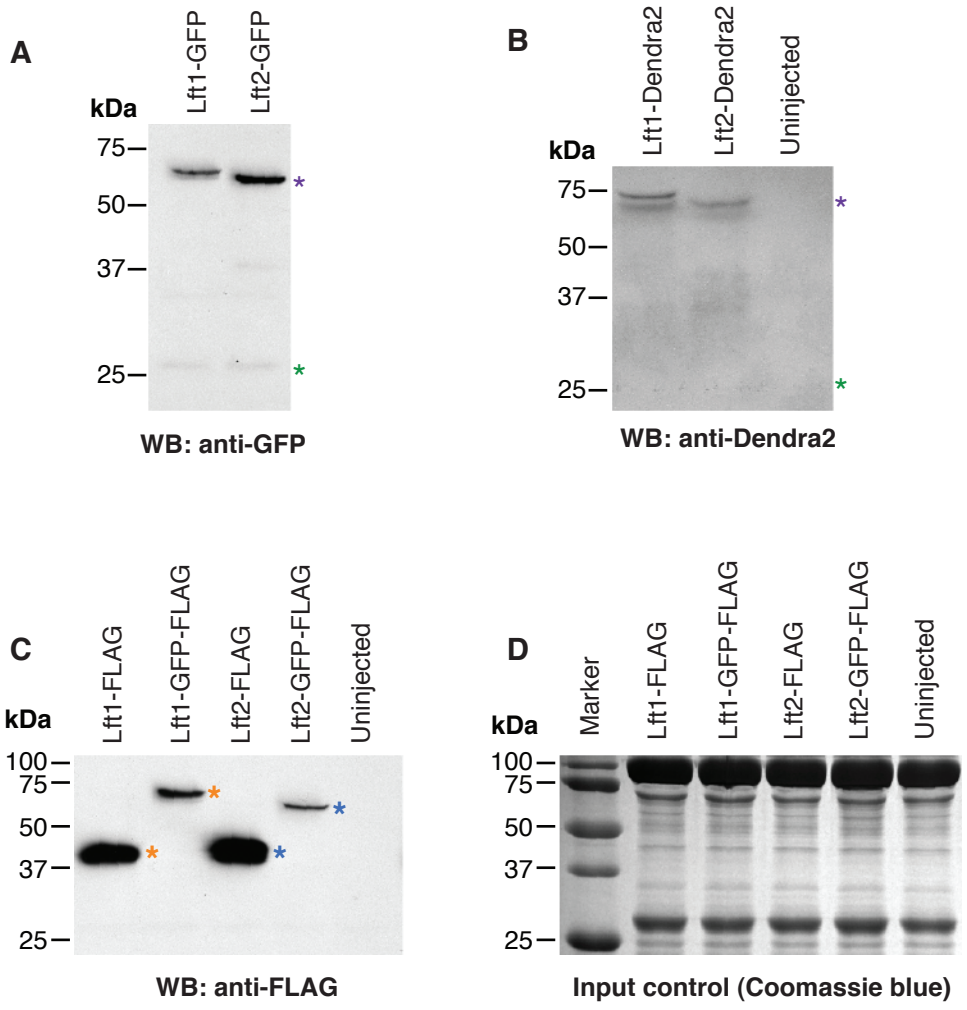

Figure S6. Detection of extracellular Lefty fusion proteins by western blot. (**A-B**) Embryos were injected with amounts of mRNA encoding GFP or Dendra2 fusion proteins equimolar to 250 pg Squint-GFP at the one- to two-cell stage (Lefty1-GFP/Dendra2: 234 pg, Lefty2-GFP/Dendra2: 236 pg) and deyolked and dissociated at late blastula stages (Text S3). The extracellularly enriched fraction was probed for the presence of GFP or Dendra2 by immunoblotting with anti-GFP or anti-Dendra2 antibodies. For each blot the position of marker bands of known molecular weight (kDa) is indicated. Asterisks denote the location of the mature processed Lefty fusion proteins (purple) as well as the free fluorescent proteins (green). (**C**) Embryos at the one- to two-cell stage were injected with mRNA encoding FLAG-tagged and FLAG-GFP constructs at equimolar amounts for each protein species (Lefty1-FLAG: 330 pg, Lefty1-GFP-FLAG: 500 pg, Lefty2-FLAG: 330 pg, Lefty2-GFP-FLAG: 500 pg). The Lefty1 fusions are indicated with orange asterisks; the Lefty2 fusions are indicated with blue asterisks. The FLAG-GFP-tagged proteins are present at lower levels compared to the FLAG-tagged proteins. (**D**) Input control for (C). Total protein was stained with Coomassie blue.

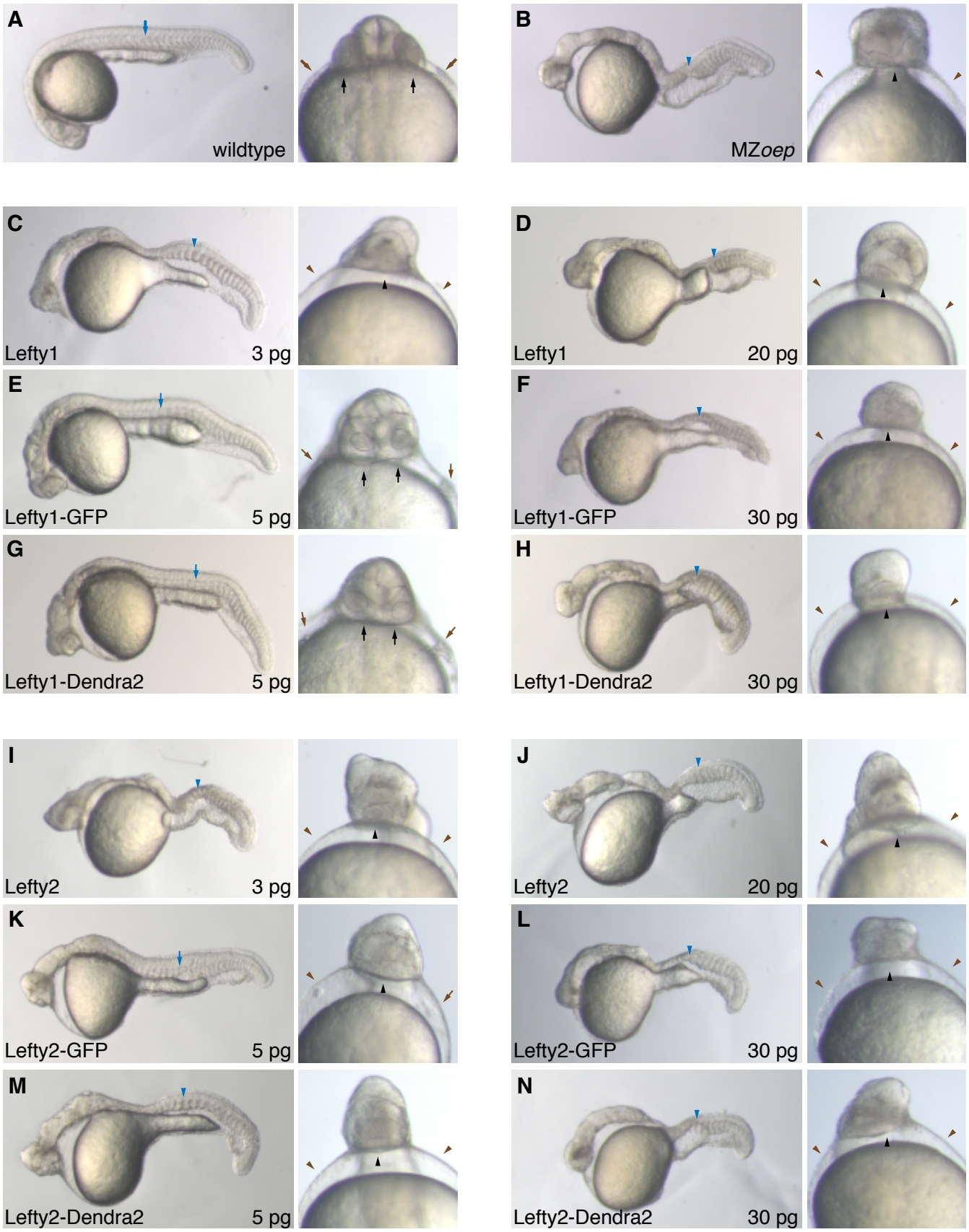

Figure S7. Overexpression of Lefty fusion proteins phenocopies Nodal loss of function. Embryos at the one-cell stage were injected with equimolar amounts of the indicated amounts of mRNA encoding tagged or untagged Lefty constructs and imaged 24 - 27 hours post-fertilization. Loss of Nodal signaling results in failure to generate head and trunk mesendoderm, leading to cyclopia and the lack of a notochord and hatching gland. (**A**) Uninjected wildtype embryo, lateral view on the left, ventral view of head on the right. Blue arrow: notochord. Black arrows: eyes. Brown arrows: hatching gland cells. (**B**) Maternal-zygotic (MZ*oep*) mutant for the Nodal co-receptor *oep* (*one-eyed pinhead*). All Nodal signaling is abolished in MZ*oep* embryos, which exhibit cyclopia (black arrowhead) and loss of notochord (blue arrowhead) and hatching gland (brown arrowheads). (**C-H**) Overexpression of Lefty1 constructs. (**I-N**) Overexpression of Lefty2 constructs. (E, G, K) Note partial reduction of notochord (thin blue arrow) and hatching gland (thin brown arrow). Also note close proximity of eyes in (E) and (G), consistent with partial loss of Nodal function.

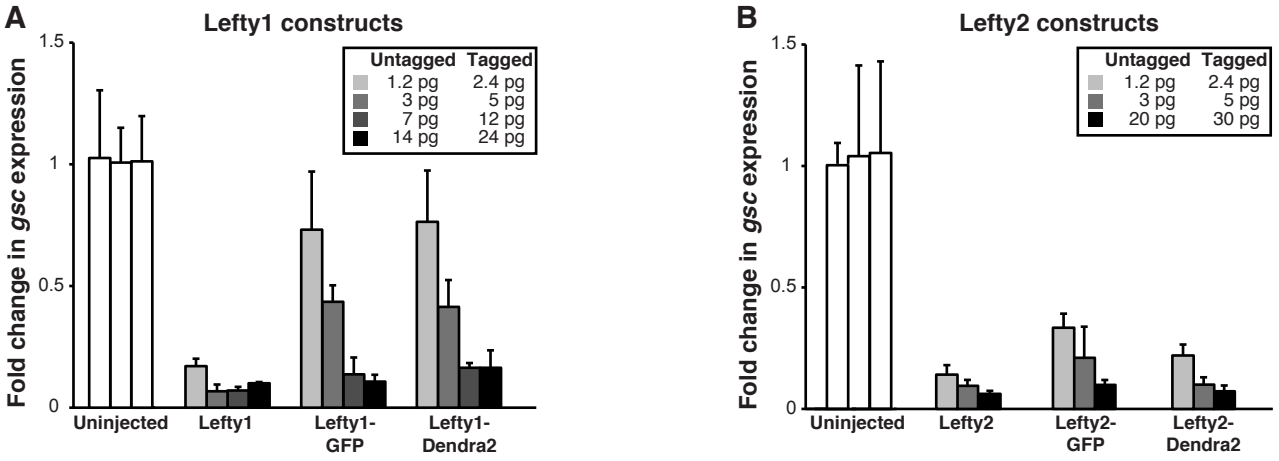

Figure S8. Quantitative reverse transcription PCR (qRT-PCR) to assess Lefty fusion construct activity. Embryos at the one- to two-cell stage were injected with different amounts of mRNA encoding the indicated constructs and collected at 50% epiboly (Text S3). Fold decrease in expression of the Nodal target gene *goosecoid* (*gsc*) compared to uninjected embryos was determined by qRT-PCR. Different mRNA amounts were used to assess dose-dependent repression. The zebrafish elongation factor *eF1*α was used as a normalization control. Fold decrease in *gsc* expression in embryos injected with mRNA encoding tagged or untagged versions of Lefty1 (**A**) and Lefty2 (**B**) compared to uninjected embryos is shown. Error bars indicate standard deviation.

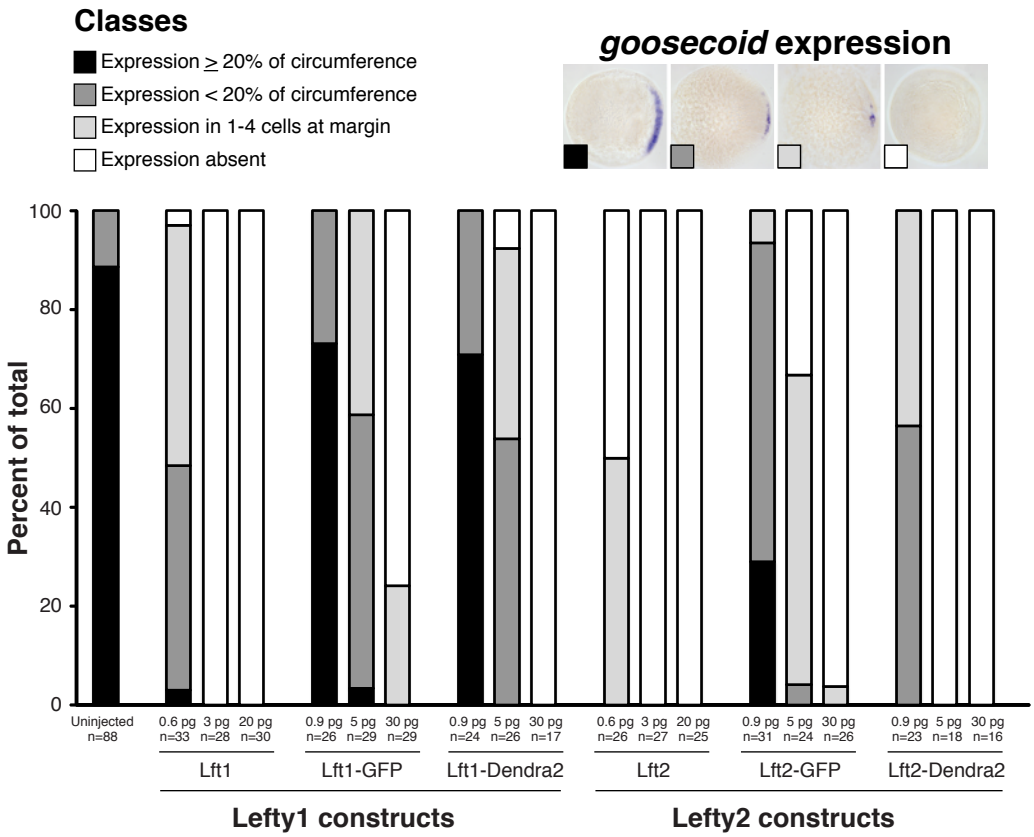

Figure S9. *In situ* hybridization to assess Lefty fusion construct activity. Embryos at the one-cell stage were injected with different amounts of mRNA encoding the indicated constructs equimolar to the untagged constructs and fixed at 50% epiboly (Text S3). Different amounts of mRNA were injected in order to assess dose-dependent repression of the Nodal target gene *goosecoid* (*gsc*) using *in situ* hybridization. Lefty-GFP and -Dendra2 fusion proteins are biologically active. Embryos were scored according to the indicated classes. n indicates the number of embryos analyzed.

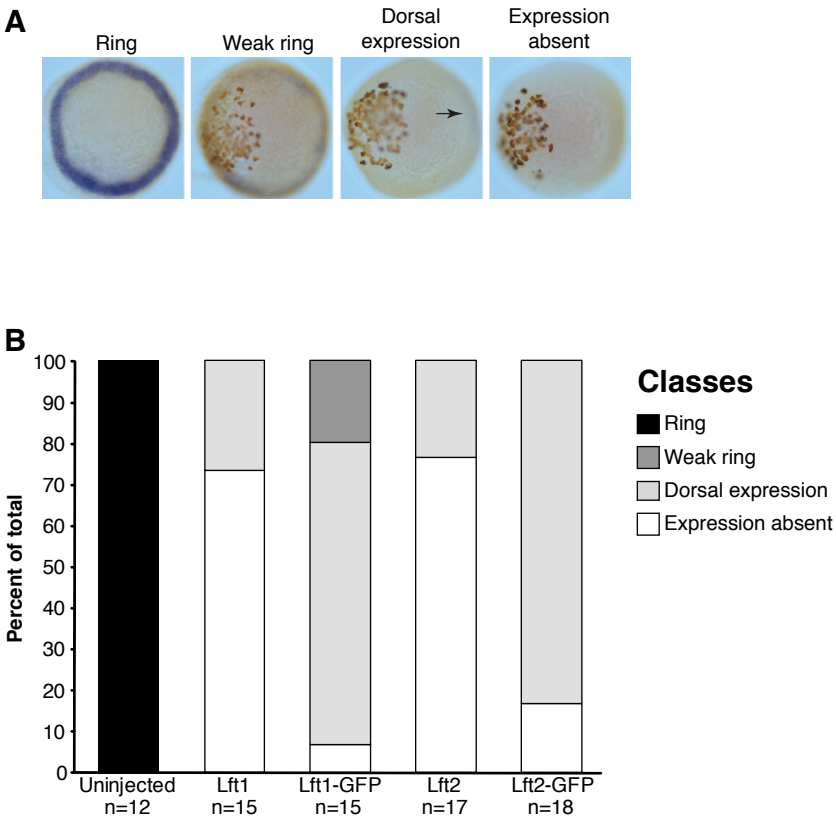

Figure S10. Tagged and untagged Lefty proteins have similar activity ranges. To assess the range of Lefty constructs, single cells in embryos at the 64- to 128-cell stage were injected with equimolar amounts of mRNA (Lefty1 and Lefty2: 6 pg; Lefty1-GFP and Lefty2-GFP: 9 pg). Biotin-dextran (brown) was used as an injection tracer. Embryos were fixed at 50% epiboly (Text S3). Activity range was assessed by *in situ* hybridization against the Nodal target gene *fascin* (blue). *fascin* is normally expressed in a ring at the blastula margin (**A**, left panel). In embryos containing clones that secrete tagged or untagged Lefty proteins, the ring of *fascin* expression is reduced or absent. (**B**) Quantification of the activity range of Lefty constructs. Embryos were scored according to the classes shown in (A). Arrow indicates faint dorsal expression. Blue: *fascin* expression, brown: cells expressing Lefty constructs (as assessed by staining for the injection tracer biotinylated dextran).

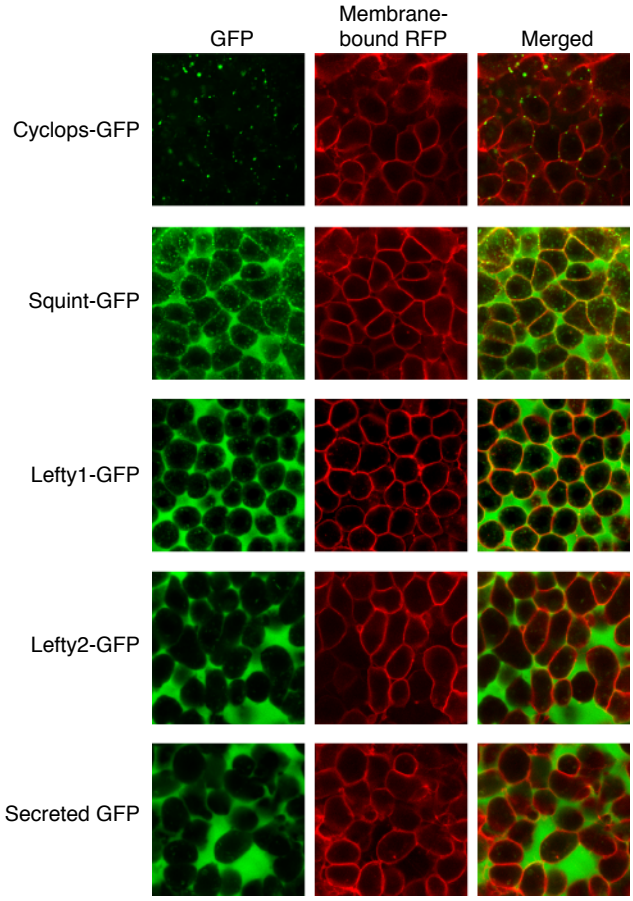

Figure S11. Localization of uniformly expressed Nodal- and Lefty-GFP fusion proteins. Embryos at the one-cell stage were co-injected with 30 pg of mRNA encoding the indicated fusion construct and 30-50 pg of mRNA encoding membrane-bound RFP to outline cellular membranes. Embryos were imaged between sphere stage and 30% epiboly. Cyclops-GFP exhibits weak diffuse extracellular localization as well as bright membrane-associated clusters. Membrane-associated clusters are less frequently found in embryos expressing Squint-GFP. Lefty1- and Lefty2-GFP are almost exclusively extracellular. The localization of Nodal- and Lefty-Dendra2 fusion constructs is similar to that of the corresponding GFP fusions (not shown).

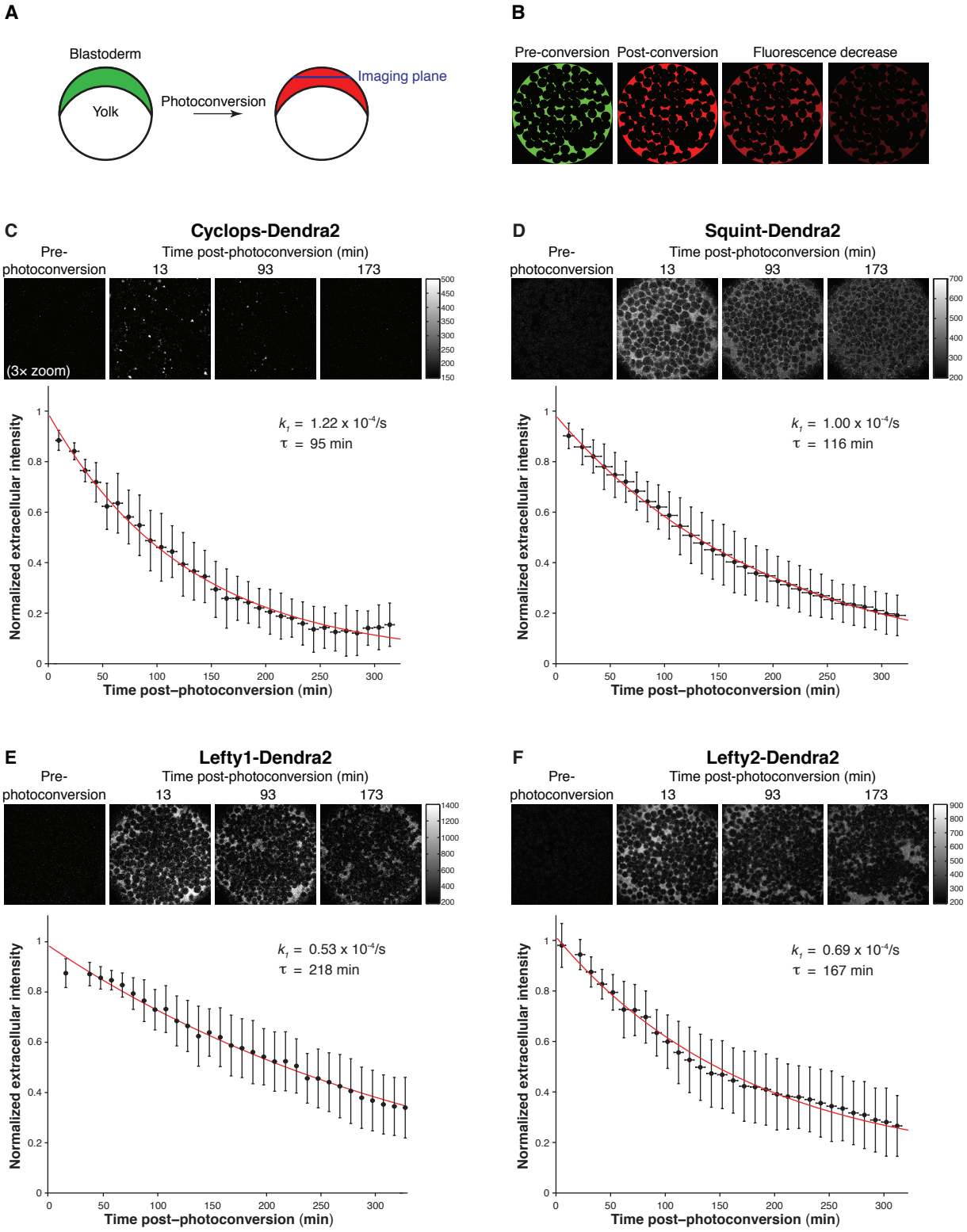

Figure S12. Measurement of extracellular clearance rate coefficients (k_1). (**A**) Clearance assay experimental overview. Uniformly expressed Dendra2 fusion proteins were photoconverted using a UV pulse. (**B**) Images were obtained every 10 or 20 minutes following photoconversion for a total of five hours. The intensity decrease in the extracellular space over time was used to determine the clearance rate coefficient of the extracellular fusion protein (Text S5). (**C-F**) Embryos were co-injected at the one-cell stage with 0.4-1.9 ng Alexa488-dextran and 60 pg of mRNA encoding Cyclops-Dendra2 (C), Squint-Dendra2 (D), Lefty1-Dendra2 (E), or Lefty2-Dendra2 (F). Ubiqitously expressed Dendra2 fusion proteins were photoconverted at late blastula stages. The average extracellular photoconverted Dendra2 intensity was monitored over time (the Alexa488 signal was used to mask intracellular regions). Clearance rate coefficients (k_1) and half-lives ($\tau = \ln(2)/k_1$) were determined by fitting exponential functions to data from individual embryos from both 10 and 20 min interval experiments. The normalized average intensity from 10 min interval experiments (black) is shown fitted with exponential functions (red). Error bars indicate standard deviation. For 10 min interval experiments, Cyclops-Dendra2: n=6, Squint-Dendra2: n=11, Lefty1-Dendra2: n=7, and Lefty2-Dendra2: n=13. Cyclops-Dendra2 images are shown at 3× magnification to enhance visibility of punctate signal.

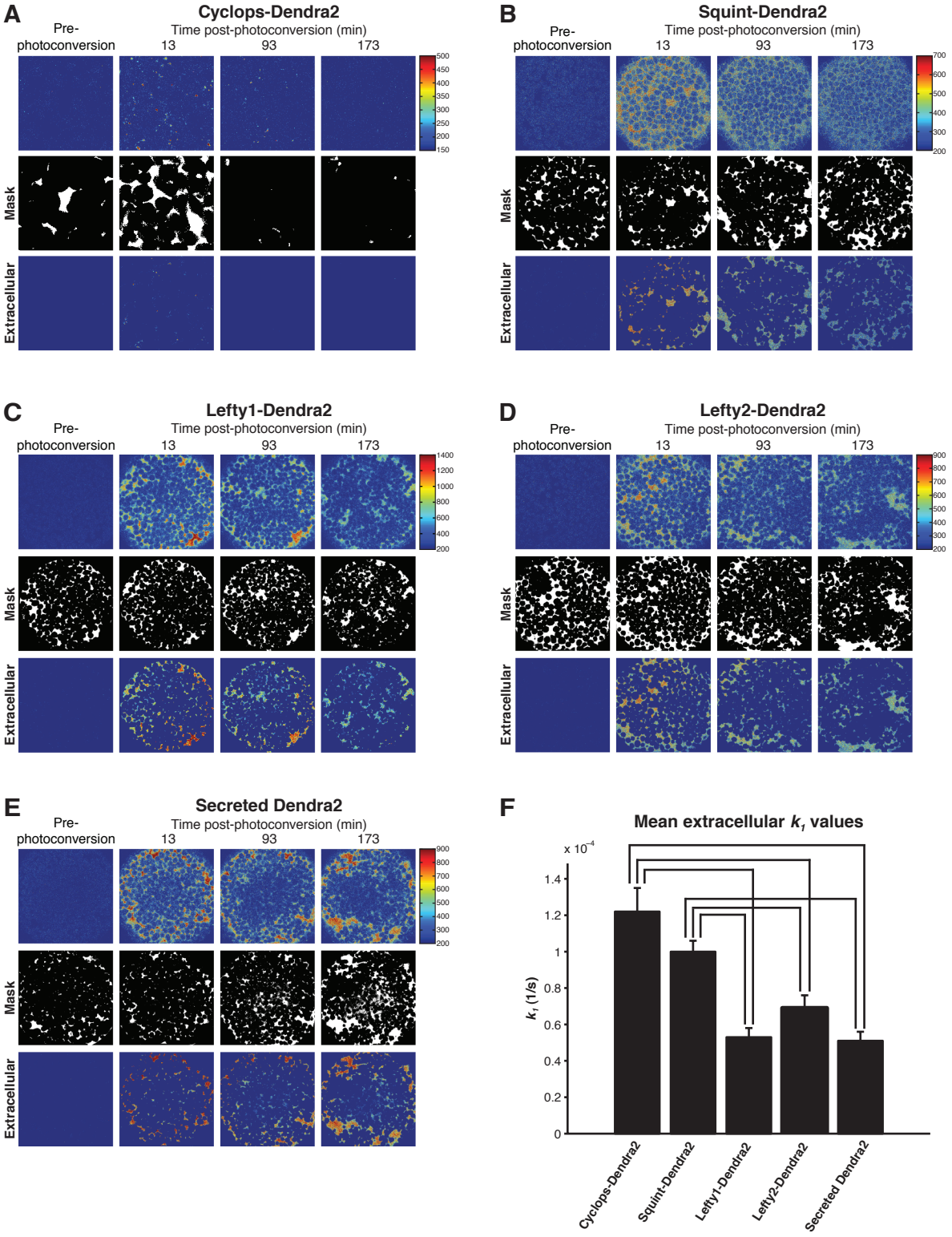

Figure S13. Masking intracellular signal in the clearance assay. (**A-E**) Embryos were co-injected at the one-cell stage with 0.4-1.9 ng Alexa488-dextran and 60 pg of mRNA encoding Cyclops-Dendra2 (A), Squint-Dendra2 (B), Lefty1-Dendra2 (C), Lefty2-Dendra2 (D), or secreted Dendra2 (E). Uniformly expressed fusion proteins were photoconverted using a UV pulse at late blastula stages, and one medial optical slice was imaged once every 10 or 20 min. The majority of the Alexa488-dextran remains inside cells. Using a thresholding algorithm and Alexa488 signal (Text S5), masks were generated to define extracellular space (middle panel, white). This mask was then applied to the images from the red channel (top panel) in order to generate images in which only the extracellular red photoconverted Dendra2 signal is considered (bottom panel). (**F**) Summary of average extracellular clearance rate coefficient (k_1) values. Extracellular red fluorescence after photoconversion was monitored over time in individual embryos expressing the indicated Dendra2 fusion constructs. For each embryo, the resulting data set was fitted with an exponential function (Text S5), and the clearance rate coefficient (k_1) was determined. Average k_1 values from 10 and 20 min interval experiments (fig. S16) are shown for each construct. Average k_1 values that are significantly different between different experimental groups (p-value < 0.005, Wilcoxon-Mann-Whitney test) are indicated by black lines. Higher k_1 values indicate higher protein clearance. Error bars indicate standard error. Cyclops-Dendra2: n=9; Squint-Dendra2: n=23; Lefty1-Dendra2: n =19; Lefty2-Dendra2: n=27; secreted Dendra2: n=22.

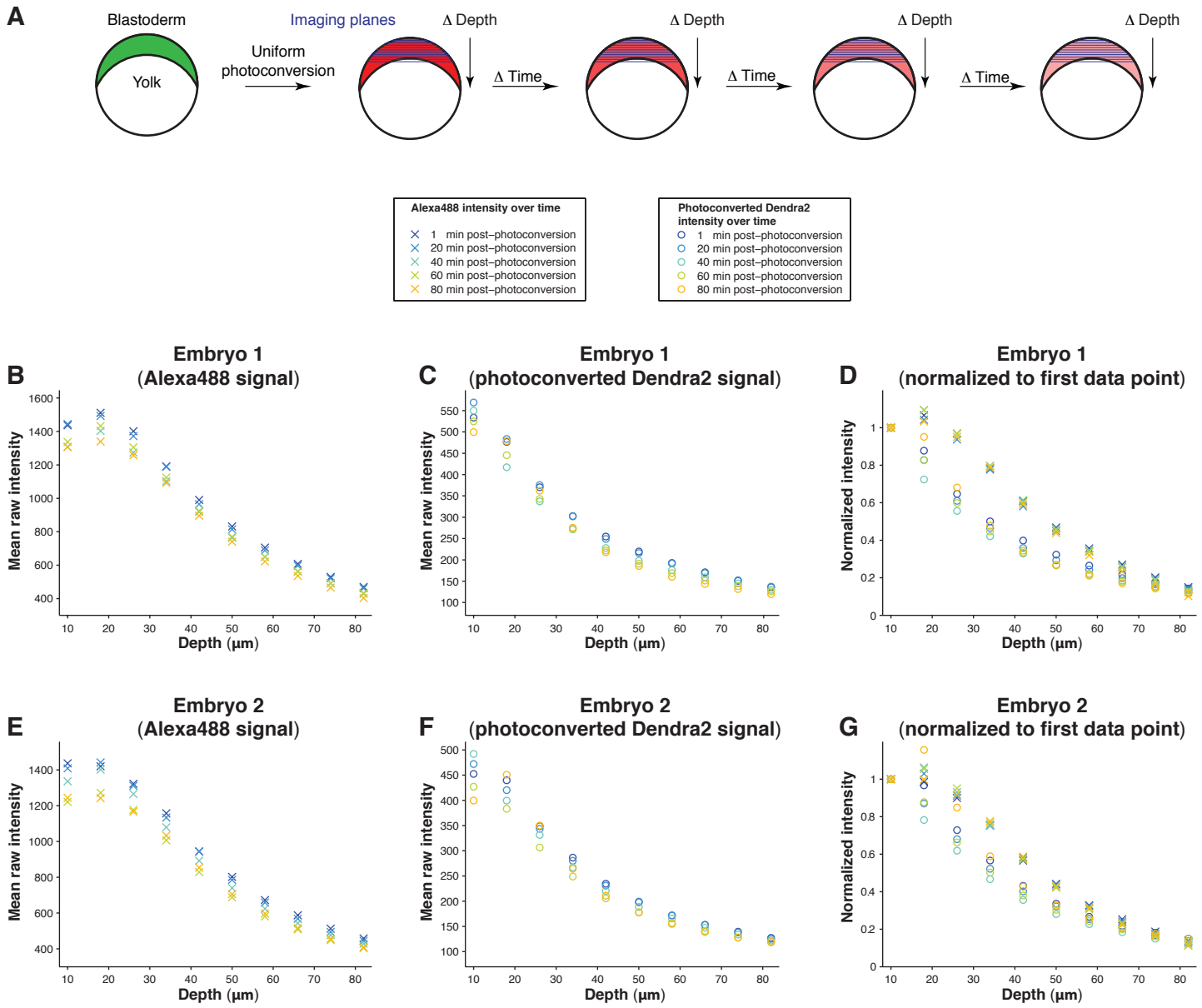

Figure S14. Assessing uniformity of photoconversion. If photoconversion in the clearance assay were non-uniform, the measurements of clearance rate coefficients could be flawed due to diffusive flux. Therefore, the uniformity of photoconversion along the animal-vegetal axis was determined by measuring mean intensity at different depths in embryos containing photoconverted secreted Dendra2 over time. If protein near the animal pole were more likely to be photoconverted than protein near the vegetal pole, the observed normalized signal intensity near the vegetal pole would increase over time due to diffusion of photoconverted protein from the animal pole towards the vegetal pole. (**A**) Experimental overview. Embryos were co-injected with 1.9 ng Alexa488-dextran and 60 pg mRNA encoding secreted Dendra2. Fusion proteins were photoconverted in the same manner as in the clearance assay experiments. Z-stacks comprised of 10 slices spaced by a depth of 8 μm were taken every 20 min for a total of 80 min post-photoconversion, and the mean intensity in a 35 μm diameter circular ROI centered in each slice was determined. If photoconversion were uniform, the signal should be homogeneously distributed throughout the embryo. Light scattering causes average intensity to drop as a function of depth. (**B, E**) Mean raw Alexa488 signal intensity as a function of depth in the embryo (animal pole = 0 μm). Colors indicate time post-photoconversion. Results for two embryos are shown. (**C, F**) Mean raw photoconverted red Dendra2 signal intensity as a function of depth in the embryo. (**D, G**) Normalized mean Alexa488 and photoconverted red Dendra2 signal intensity as a function of depth in the embryo. For each time point, data was normalized by dividing all time points by the average intensity in the first (most shallow) z-slice, after background subtraction of average extraembryonic intensity (70 a.u. for photoconverted Dendra2 imaging conditions and 300 a.u. for Alexa488 imaging conditions). If photoconversion were nonuniform, the normalized intensity near the vegetal pole would increase over time as photoconverted protein diffused vegetally. However, no increases in normalized vegetal signal over time were observed, suggesting that photoconversion was uniform.

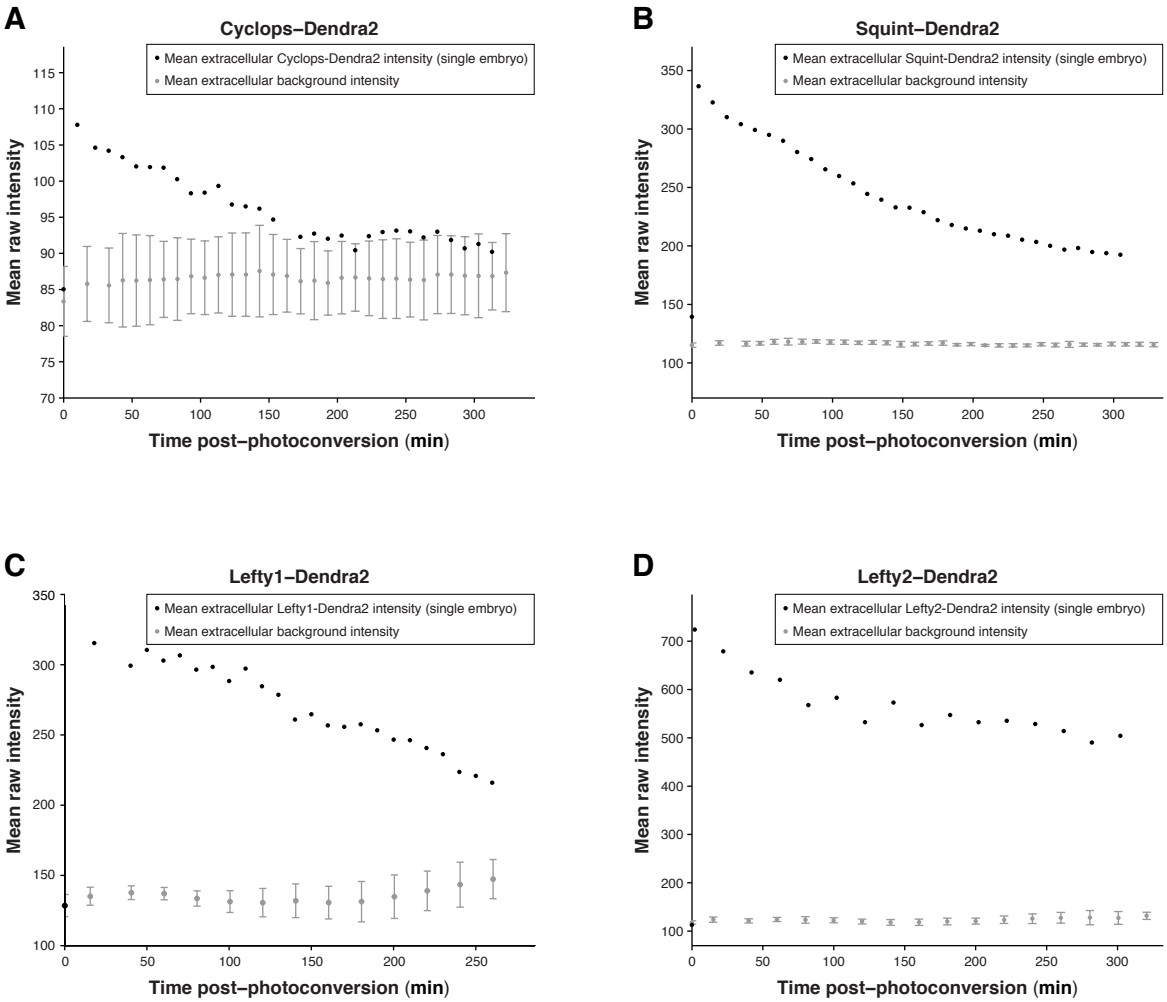

Figure S15. Assessing background intensity changes in clearance assay experiments. To determine whether changes in background intensity (e.g. due to autofluorescence and bleed-through of the green Alexa488 signal into the red channel) affect clearance measurements, 1.9 ng Alexa488-dextran were co-injected with mRNA encoding untagged Cyclops (**A**), Squint (**B**), Lefty1 (**C**) and Lefty2 (**D**) into embryos at the one-cell stage, followed by mock clearance assay. The raw mean background intensity (gray) is shown for the extracellular compartments, along with data from representative individual embryos expressing Dendra2 fusions (black). Error bars indicate standard deviation of background intensity. For all constructs, changes in background intensity were negligible (the changes in the mean raw background intensity over time are comparable to error bars at each time point). For background data, Cyclops: n=7, Squint: n=8, Lefty1: n=4, and Lefty2: n=3.

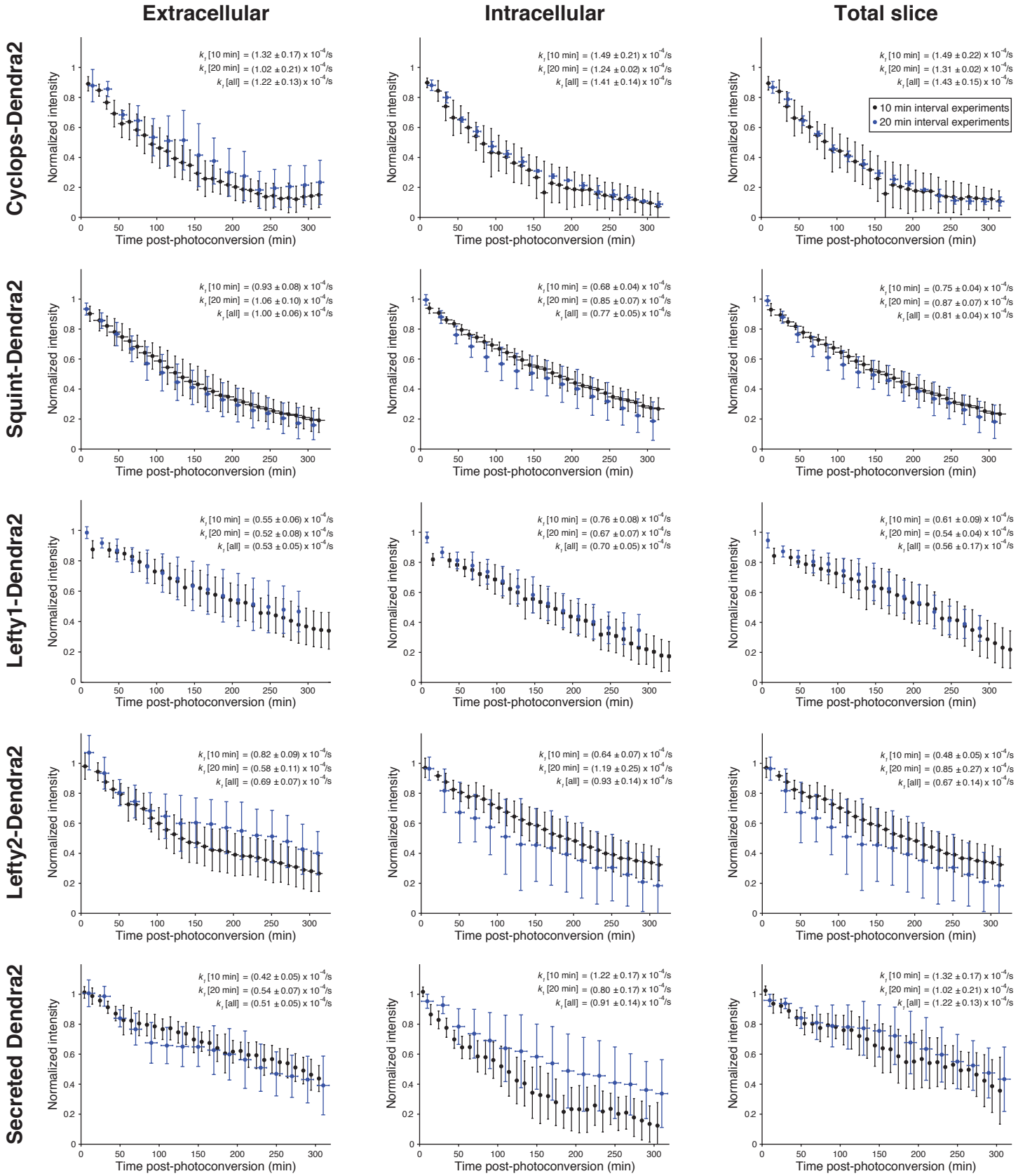

Figure S16. Assessment of photobleaching and inadvertent photoconversion. In the clearance assay, embryos are imaged multiple times over the course of five hours. To determine whether significant photobleaching occurs, or whether imaging using the 488 nm laser causes inadvertent photoconversion of Dendra2 fusion proteins, experiments were performed in which the interval between images was either 10 or 20 min. Significant photobleaching or inadvertent photoconversion would cause discrepancies in clearance kinetics observed in these two experiments. The normalized average intensity for 10 min (black) and 20 min (blue) interval data for each construct is shown. No significant differences were observed between the 10 and 20 min interval data for any construct, or for any compartment (i.e. extracellular (first column), intracellular (second column), and total optical slice (third column); all p-values were much higher than 0.005 using the Wilcoxon-Mann-Whitney test to determine whether k_1 values differed significantly between 10 and 20 min interval experiments). Average clearance rate coefficients (k_1) and standard error values are shown for 10 min (k_1 [10 min]) and 20 min (k_1 [20 min]) interval experiments separately, as well as for 10 and 20 min interval experiments combined (k_1 [all]). Error bars indicate standard deviation. For 10 min interval experiments, Cyclops-Dendra2: n=6, Squint-Dendra2: n=11, Lefty1-Dendra2: n=7, Lefty2-Dendra2: n=13, and secreted-Dendra2: n=6. For 20 min interval experiments, Cyclops-Dendra2: n=3, Squint-Dendra2: n=12, Lefty1-Dendra2: n=12, Lefty2-Dendra2: n=14, and secreted-Dendra2: n=16.

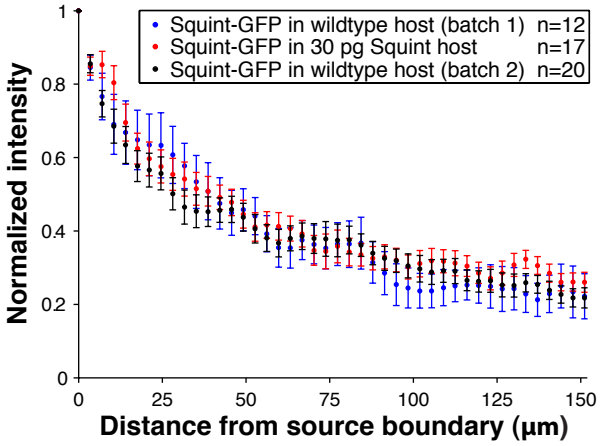

Figure S17. Overexpression of Squint does not alter Squint-GFP dispersal. If Nodal binding sites are saturated, the diffusivity of the molecules may be overestimated in FRAP experiments. In this scenario, overexpression of untagged Squint should saturate binding sites and thus increase the diffusivity and extend the range of Squint-GFP. To test this idea, we overexpressed 30 pg of untagged Squint (similar to levels of Squint-GFP used in FRAP experiments) and then analyzed the distribution of Squint-GFP generated from a local source. Importantly, co-expression did not result in a change in Squint-GFP distribution, arguing against the idea of saturation. Data points represent averages, and error bars indicate standard error of n experiments.

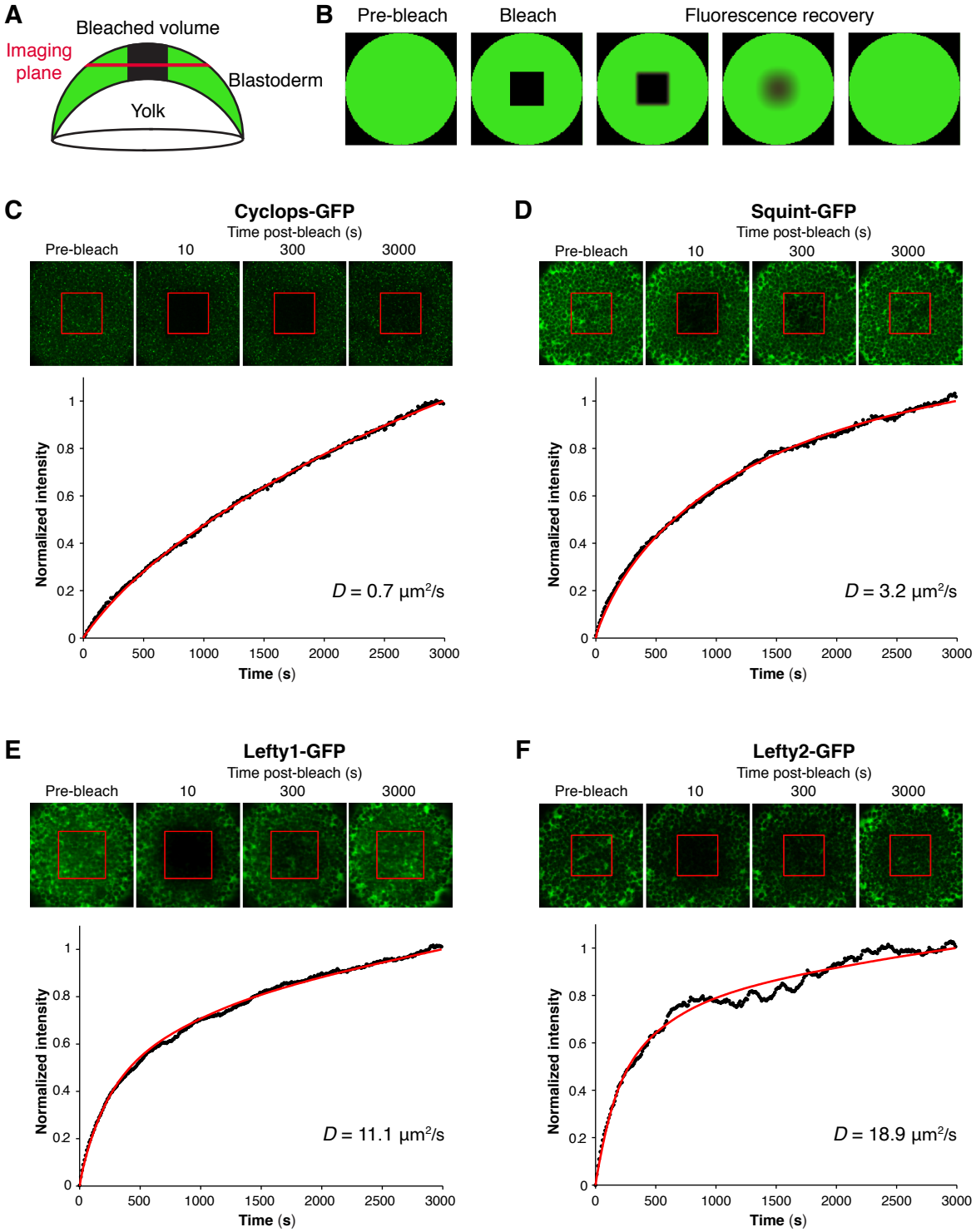

Figure S18. Measurement of effective diffusion coefficients. (A-B) FRAP experimental overview. A cuboidal volume was bleached into embryos uniformly expressing secreted fluorescent fusion proteins (A). Medial optical slices were imaged every 10 s following bleaching. The average intensity in the bleached region recovers over time (B) and can be used to calculate the diffusion coefficient of the fluorescent species. (**C-F**) Embryos were injected at the one-cell stage with 30 pg of mRNA encoding Cyclops-GFP (C), Squint-GFP (D), Lefty1-GFP (E) or Lefty2-GFP (F). Uniformly expressed Nodal- or Lefty-GFP fusion proteins were locally photobleached at blastula stages. Optical slices were acquired every 10 s after the bleach for a total of 50 min. The effective diffusion coefficient, *D*, was determined by fitting the resulting recovery profile (black) with simulated recovery curves (red) that were numerically generated using a model that includes diffusion, production and clearance in a three-dimensional embryo-like geometry (Text S6). Results for individual embryos are shown normalized to the final time point, and average diffusion coefficients are listed here and in Table S6.

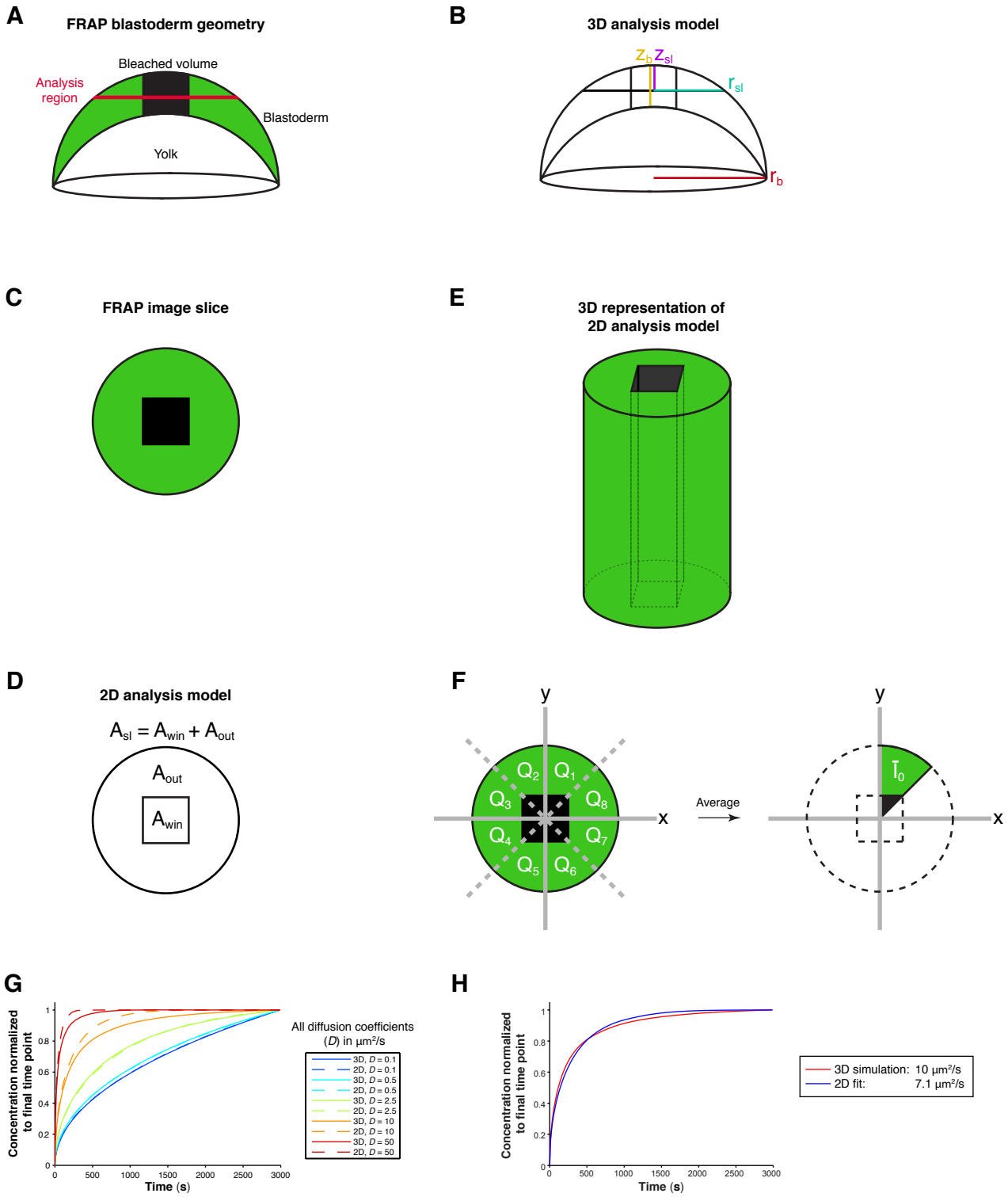

Figure S19. FRAP geometries. (**A**) Average embryo geometry during FRAP experiments. Embryos were injected with mRNA encoding GFP fusion constructs at the one-cell stage, generating embryos that uniformly express the GFP fusions (green). FRAP experiments were performed at late blastula stages, when the blastoderm forms a dome on top of the yolk. A cuboidal volume was bleached into the center of the embryo (black), and recovery of fluorescence was observed in a medial optical section (red). This geometry was used for three-dimensional simulations of FRAP experiments (3D analysis model) with the geometric parameters indicated in (**B**). (**C**) Medial optical section acquired during FRAP experiments (two-dimensional view of the red line in (A)). The bleached window is indicated in black. This geometry was used for two-dimensional simulations of FRAP experiments (2D analysis model) as shown in (**D**).The analysis areas inside the bleach window (A_{win}), outside the bleach window (A_{out}) and the entire slice (A_{sl}) used to calculate spatial intensity averages are indicated. (**E**) Three-dimensional extension of the two-dimensional model shown in (C) and (D). The slice would extend to infinity above and below the depicted cylinder geometry. (**F**) Averaging of the eight octants (Q_1-Q_8) for the first image taken after photobleaching defines the initial condition $\bar{I}_0$ in the imaging plane used for three-dimensional simulations of FRAP experiments. (**G**) Simulated FRAP recovery curves in two- and three-dimensional model geometries. FRAP experiments were simulated using the 3D or 2D analysis models for a range of diffusion coefficients, D, from 0.1 to 50 μm²/s without clearance or production. For the initial condition, the concentration in the bleached region was set to a value of zero and to a value of one everywhere else. The resulting recovery curves in the bleached window were normalized to the concentration at the final time point t = 3000 s. Note that the recovery profiles in two- and three-dimensional geometries are similar for small values of D, but different for higher diffusivities. (**H**) The 3D analysis model was used to generate a recovery curve given a diffusion coefficient of 10 μm²/s (red). This simulated curve was then fitted using the 2D model (blue). Consistent with (G), the 2D fit results in a lower diffusion coefficient, highlighting the differences between the 2D and 3D approaches and the importance of using the appropriate geometry when fitting FRAP data.

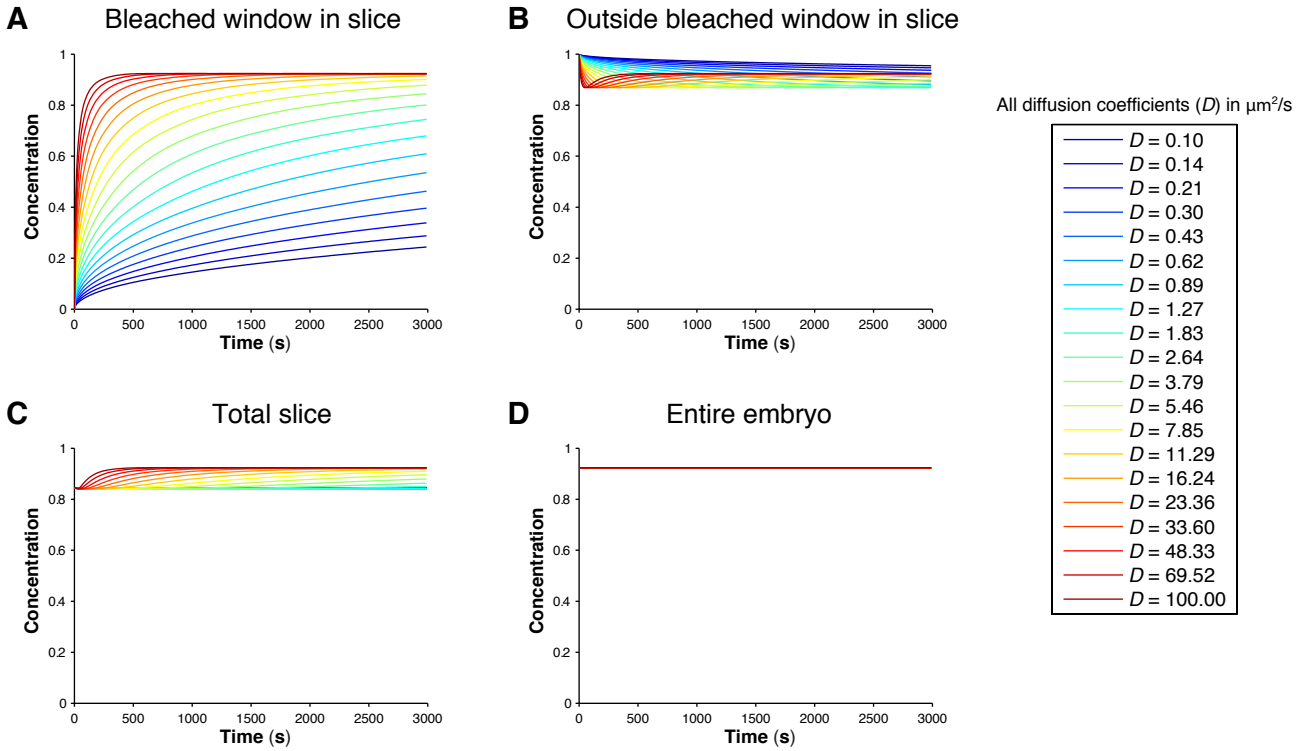

Figure S20. Diffusive flux in the three-dimensional embryo geometry. FRAP experiments were simulated using the 3D analysis models for a range of 20 diffusion coefficients, *D*, logarithmically spaced between 0.1 and 100 μm^2/s without clearance or production. For the initial condition, the concentration in the "bleached volume" was assigned a value of zero and a value of one everywhere else. The average concentration was calculated for each time point in the bleached window (**A**), in the region outside of the window (**B**), in the analysis slice (**C**), and in the total embryo (**D**). Note that in a two-dimensional geometry, the concentration in the analysis slice (C) should be constant due to no-flux boundary conditions, whereas diffusive flux through the slice has a significant contribution in the three-dimensional model for certain diffusion coefficients. The concentration in the entire three-dimensional model (D) is constant and conserved due to no-flux boundary conditions.

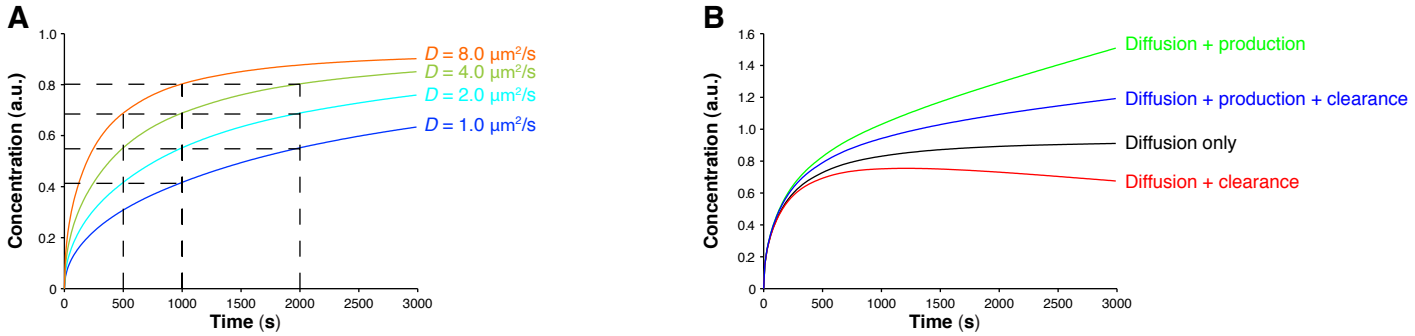

Figure S21. Simulation of FRAP recovery curves with diffusion, clearance and production. All simulations were performed using the three-dimensional analysis model. For the initial condition, the concentration in the bleached volume was set to a value of zero, and a value of one was assigned everywhere else. The average concentration was calculated for each time point in the bleached window. (**A**) Scaling of recovery curves with diffusion time in the "diffusion only" model. Note that the recovery curves scale with diffusion coefficient and time. For example, it takes a recovery curve with a diffusion coefficient of $D_1 = 1.0$ μm²/s twice as long to reach the same concentration as a recovery curve with $D_2 = 2D_1 = 2.0$ μm²/s and four times as long as a recovery curve with $D_2 = 4D_1 = 4.0$ μm²/s. This relationship was used to simulate FRAP experiments in a non-dimensionalized model using a single reference diffusion coefficient to generate a one-parameter family of curves. (**B**) Constructing recovery curves with diffusion, clearance and production. It was assumed that all reactions (clearance and production) are linear and occur everywhere in the embryo. Therefore, contributions from diffusion, clearance and production are linearly superimposed on the recovery profile. To generate recovery curves with the appropriate reactions model, a family of curves was first generated based on diffusion only by numerical simulation as described in (A). The resulting recovery curve was scaled to a diffusion coefficient of choice (in this case $D = 10$ μm²/s), and then clearance (in this case $k_1 = 0.0001$/s) or production terms (in this case $k_2 = 0.0002$ a.u./s) were added using the analytical solutions described in Text S6.

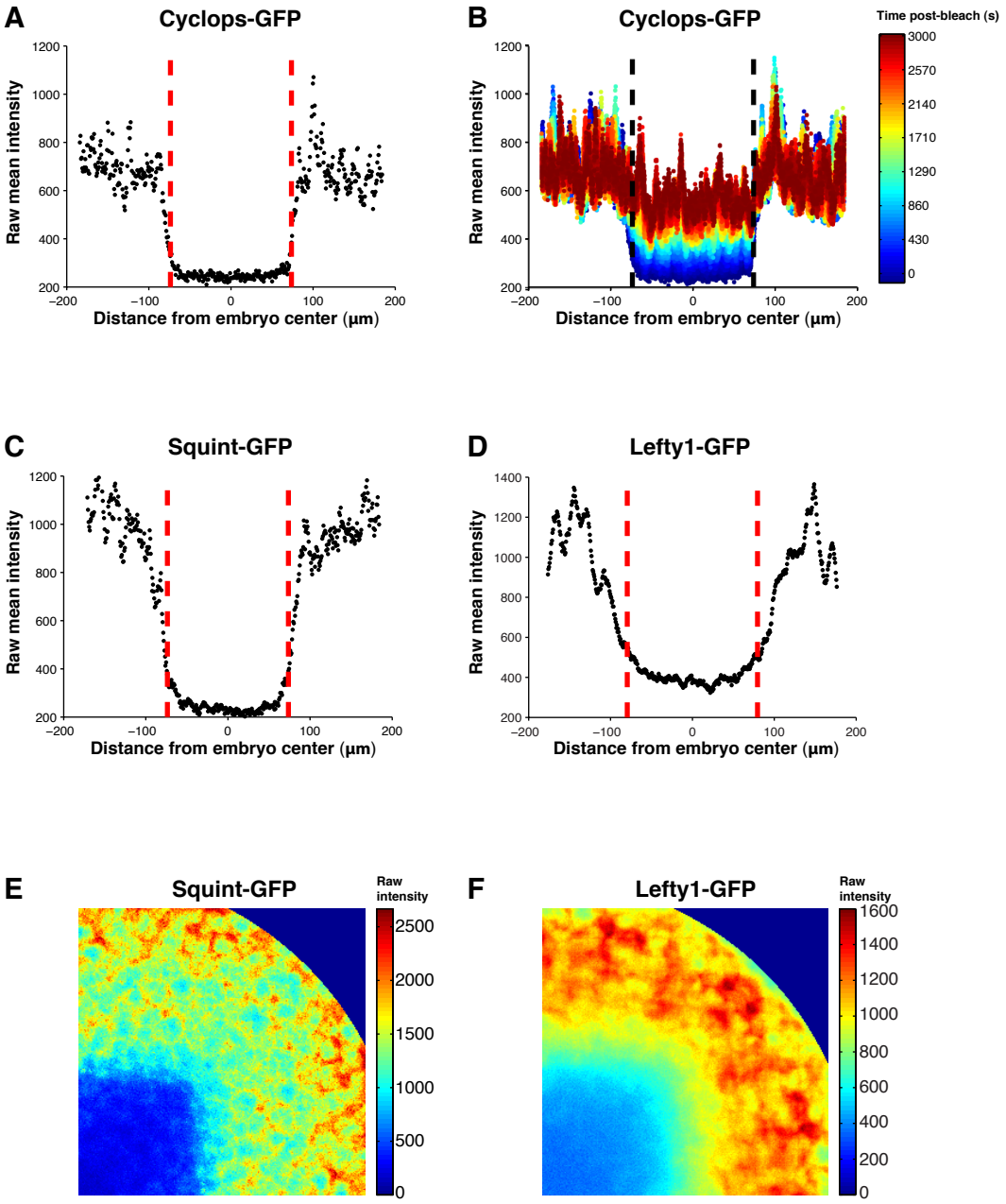

Figure S22. Intensity profiles post-photobleaching in FRAP experiments. A cuboidal volume was bleached into blastula-stage embryos injected with 30 pg of mRNA encoding GFP fusion constructs at the one-cell stage. (**A-D**) The horizontal bleach profile in the optical medial slice was determined immediately after the completion of photobleaching. Note that the bleach profile is sharp for Cyclops-GFP but is more relaxed for Squint-GFP and Lefty-GFP constructs indicating increasingly higher diffusivities. (B) Time-dependent evolution of the horizontal bleach profile for an embryo expressing Cyclops-GFP. Early times are indicated as shades of blue and later times by shades of red. (**E-F**) False-color representation of the averaged image acquired immediately after photobleaching for Squint-GFP and Lefty1-GFP, respectively. The raw intensities of the eight octants (Q_1-Q_8) comprising the imaged slice were averaged pixel-wise, and the resulting averaged octant is displayed as a quadrant with two mirror images to illustrate the relatively uniform bleach profile. Note that these averaged images were used to define the initial condition for the simulations to fit the FRAP experiments as described in Text S6.

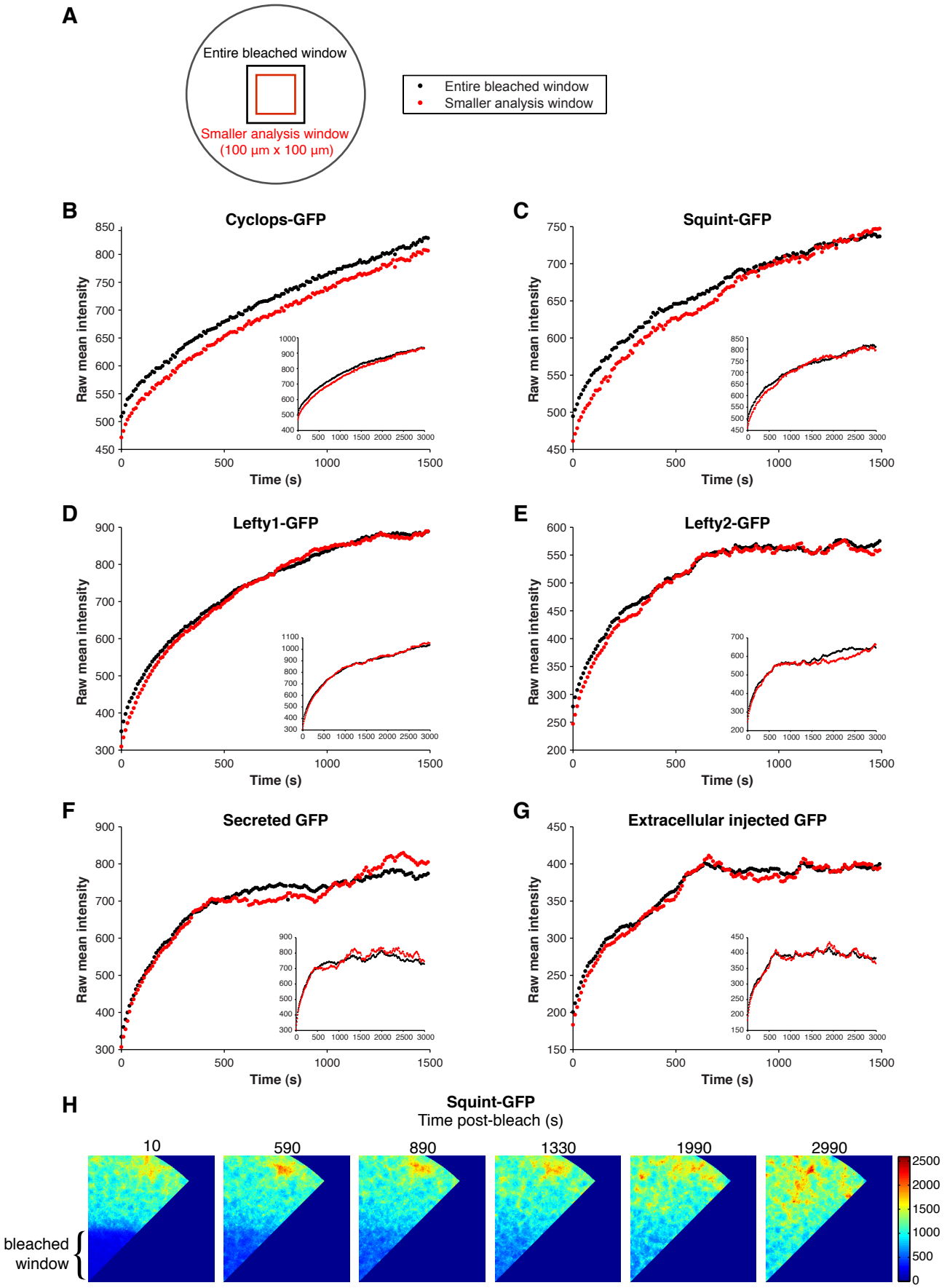

Figure S23. Diffusion-dominated recovery in FRAP experiments. The average intensity in the bleached window (black) or in a smaller window (red) nested within the bleached window (**A**) was quantified for FRAP data from single embryos (**B-G**). The first 1500 s of recovery are shown. Inset: entire 3000 s recovery. Note that recovery in a smaller analysis window of the bleached region is slower than the recovery in the bigger bleached window for the majority of Cyclops-GFP and Squint-GFP embryos analyzed. These results indicate that the FRAP recovery curves are dominated by diffusion and not by binding or other uniform reactions, which would lead to a uniform recovery independent of the analysis window dimensions (Text S6; fig. S24). The recovery delay for the Lefty1-GFP, Lefty2-GFP, and extracellular GFP experiments is less apparent, presumably due to higher diffusivities (consistent with simulations of effective diffusion in fig. S25) and the limited time-resolution of the FRAP assay. (**H**) Signal recovery occurs from the surrounding unbleached regions. Snapshots of octant-averaged images after photobleaching are shown for Squint-GFP. Note that the fluorescence in the bleached window recovers first in regions adjacent to the unbleached domain.

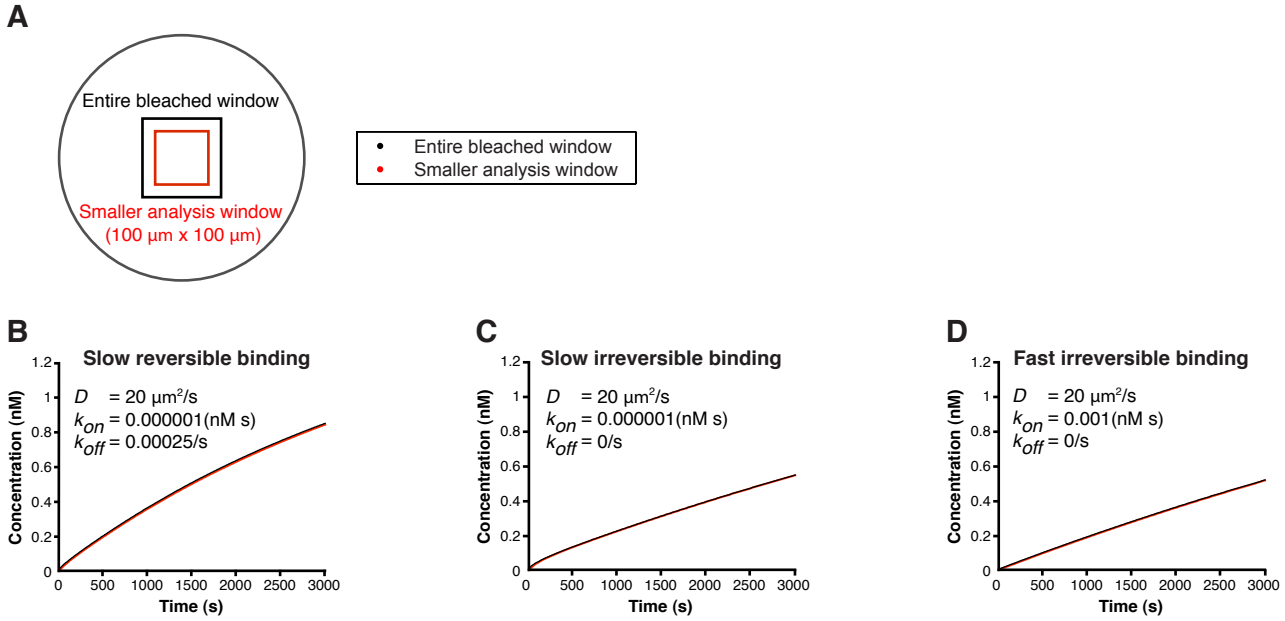

Figure S24. Examples of diffusion-uncoupled recovery curves. See Text S6.4.3 for details. Diffusion-uncoupled recovery after photobleaching occurs when diffusion is fast compared to binding kinetics. In this scenario, diffusion rapidly equilibrates the concentration in the bleached window, and the subsequent concentration increase is due to spatially uniform accumulation of bound molecules. The recovery curves would therefore not yield direct information about diffusivity but rather about binding and degradation kinetics. Diffusion-uncoupled recovery can also occur with fast diffusion and fast irreversible binding. In this case, any free molecules are rapidly trapped and the recovery curves almost exclusively reflect the spatially homogenous increase due to production and degradation. To determine whether our FRAP data could be dominated by a diffusion-uncoupled process, we simulated FRAP experiments with fast diffusion and slow binding kinetics as well as experiments with fast diffusion and fast irreversible binding. (**A**) FRAP experiments were simulated using a two-dimensional embryo model, and recovery was analyzed in the entire bleached window (black) and in a smaller window (red) nested within. Simulated recovery curves when binding is slow and reversible (**B**), slow and irreversible (**C**), and fast and irreversible (**D**). All recovery curves lack the initial delay that we observe in our FRAP experiments (fig. S23), suggesting that fast diffusion combined with slow reversible binding, slow irreversible binding, or fast irreversible binding does not occur in our experiments. Parameter values used for all simulations: $D = 20\ \mu m^2/s$, $k_{Clear} = 0.0001/s$, $k_{Prod} = 0.0002$ nM/s. The initial concentration of the diffusible ligand was set to 0 in the entire bleached window and to 0.05 nM everywhere else, whereas the initial concentration of the bound complex was set to 0.95 nM to reflect that in these models most ligand molecules would be bound. The initial concentration of the free binding partner was set to 1000 nM. The spatial averages of the sum of the diffusible species and the bound complex are shown.

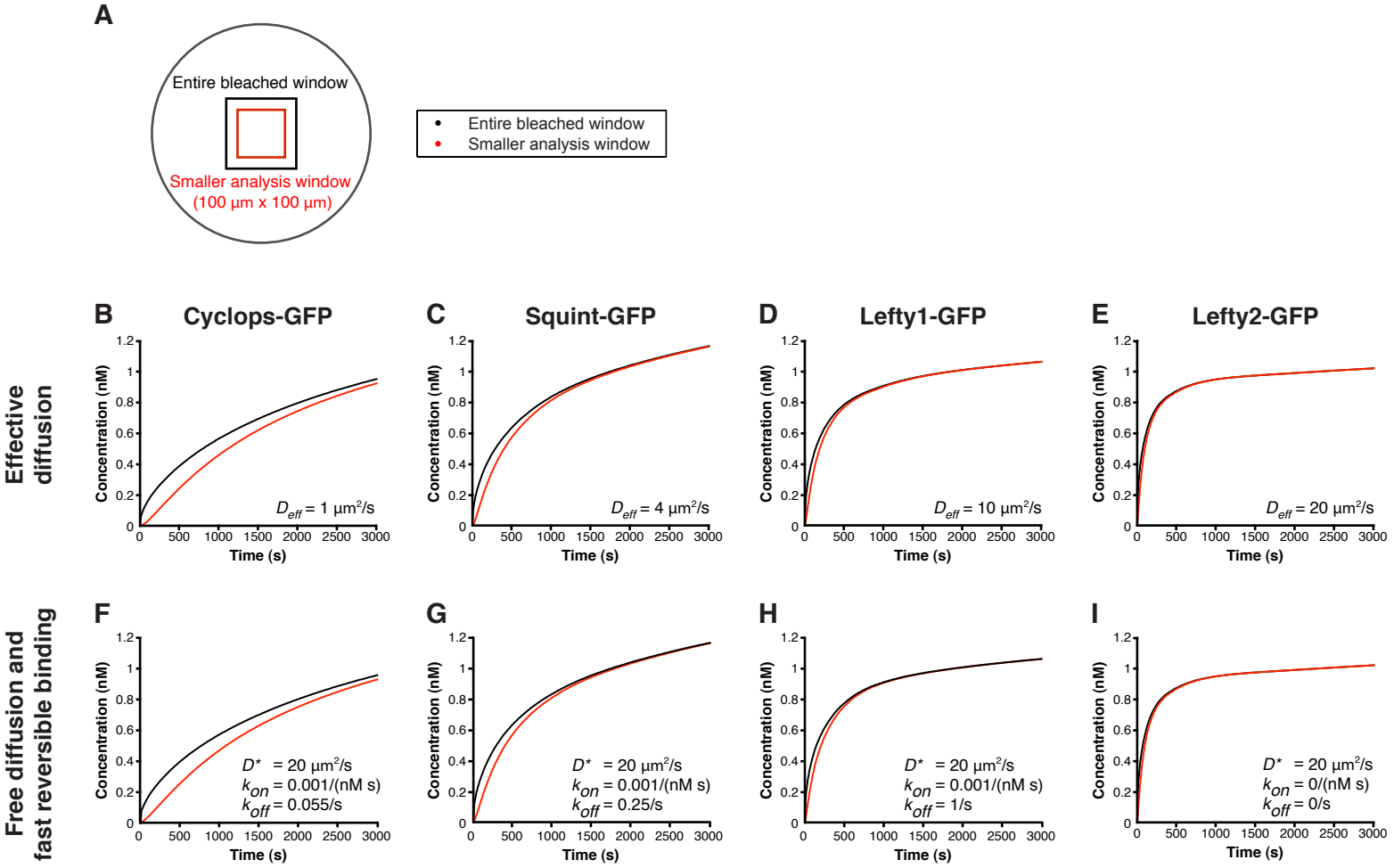

Figure S25. Potential mechanism underlying differential effective diffusivity. See Text S6.5 for details. A potential mechanism underlying differential effective diffusivity is reversible binding to immobile extracellular molecules. Nodals and Leftys may have equally high free diffusivities, but Nodals may have a higher affinity for extracellular binding partners than Leftys. In this model, fast binding and unbinding would differentially hinder free diffusion and yield smaller effective diffusion coefficients. To test this model, we simulated FRAP experiments using a two-dimensional embryo model and analyzed recovery in the entire bleached window (black) and in a smaller window (red) nested within (**A**). (**B-E**) Expected recovery curves for Cyclops-GFP (B), Squint-GFP (C), Lefty1-GFP (D), and Lefty2-GFP (E) with the indicated effective diffusion coefficients, D_{eff}, as meaured by FRAP experiments. Recovery in the smaller window is delayed, because molecules must move from the edge of the larger window to the center. The simulations recapitulate our experimental observations (fig. S23). (**F-I**) Expected recovery curves for Cyclops-GFP (F), Squint-GFP (G), Lefty1-GFP (H), and Lefty2-GFP (I) using equally high free diffusion coefficients, D^* = 20 µm²/s, in the presence of fast reversible binding. For the chosen binding kinetics, recovery curves look identical to those produced by small effective diffusion coefficients. Free diffusion combined with fast binding kinetics could therefore explain the different diffusion coefficients of Nodals and Leftys. Production rates and clearance rate constants used for the simulations are as follows: (B, F) k_{Prod} = 0.0002 nM/s, k_{Clear} = 0.000122/s; (C, G) k_{Prod} = 0.0002 nM/s, k_{Clear} = 0.0001/s; (D, H) k_{Prod} = 0.0001 nM/s, k_{Clear} = 0.000053/s; (E, I) k_{Prod} = 0.0001 nM/s, k_{Clear} = 0.000069/s. The clearance rate constants correspond to our experimental measurements. The initial concentration of the diffusible species was set to 0 in the entire bleached window and to 1 nM everywhere else. The initial concentration of the binding partner was set to 1000 nM. The spatial averages of the diffusible species are shown in (B-E), whereas the spatial averages of the sum of the diffusible species and the bound complex are shown in (F-I).

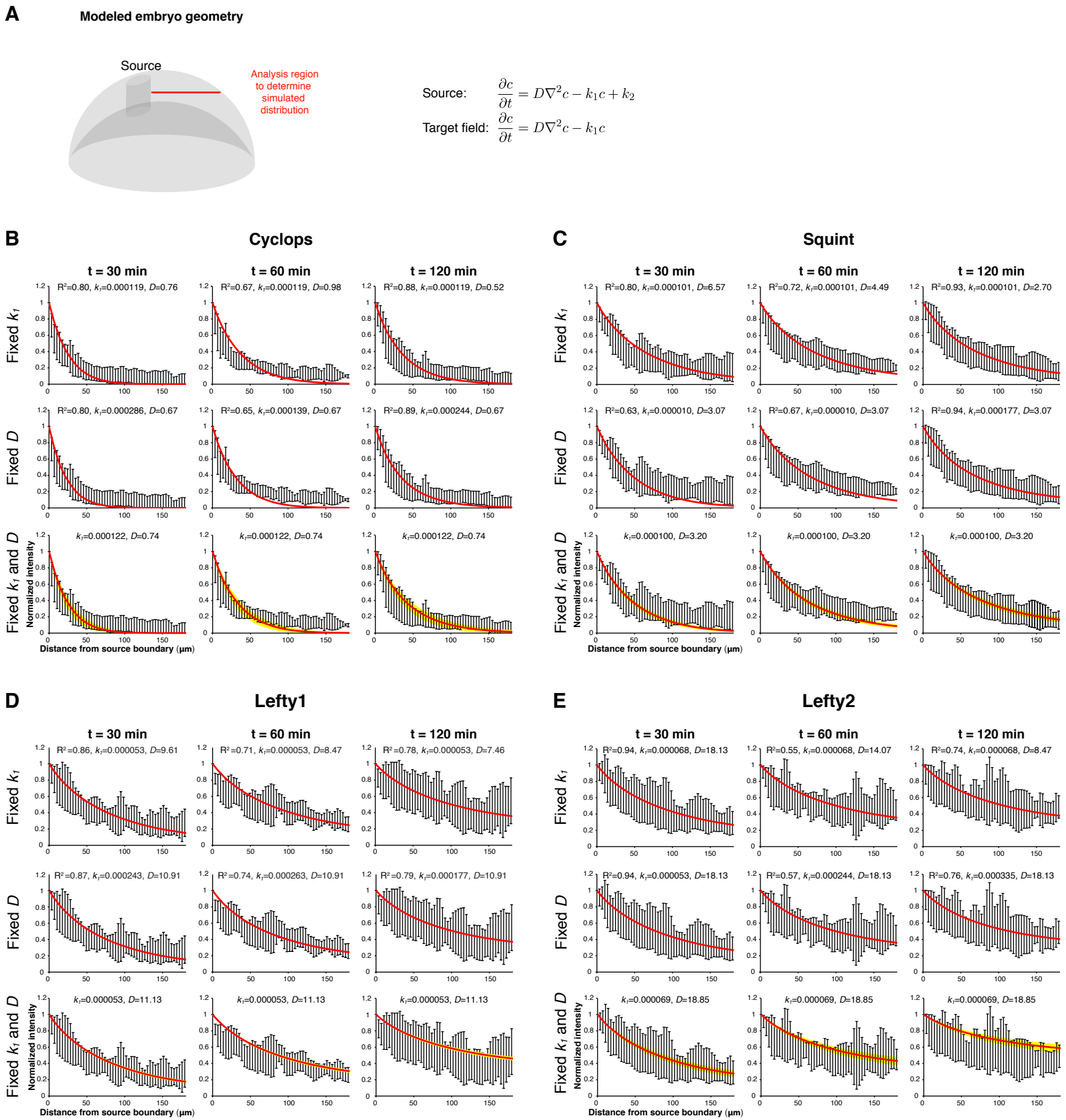

Figure S26. Modeling and simulations of gradient formation. (**A**) A parameter grid was generated in the indicated three-dimensional geometry, and equations in the source and in the target field using a combination of 50 logarithmically spaced diffusion coefficients [D_{min} = 0.1 μm^2/s, D_{max} = 50 μm^2/s] and clearance rate constants [k_{1_min} = 0.00001/s, k_{1_max} = 0.0005/s] to simulate the gradient formation experiments from Fig. 2. (B-E) This parameter space was searched for the best match with the least sum of squared differences between experimental data and simulated gradients using values in the parameter space closest to the experimentally determined diffusion coefficients (fixed D) or clearance rate constants (fixed k_1) for Cyclops (**B**), Squint (**C**), Lefty1 (**D**) and Lefty2 (**E**) constructs. Finally, profiles using the experimentally determined values of both D and k_1 were generated and overlaid onto the experimental data (fixed k_1 and D). Black error bars indicate the standard deviation for the indicated experiments, and red lines show the results of the simulations. R^2 values indicate the goodness of fit. Yellow indicates the range of expected gradients based on D and k_1 measurements: the upper limit was determined by generating a gradient using the mean D plus standard error and the mean k_1 minus standard error, whereas the lower limit was determined using the mean D minus standard error and the mean k_1 plus standard error. All diffusion coefficients, D, are reported in units of μm^2/s, and all clearance rate coefficients (k_1) are reported in units of 1/s.

Movie S1. Squint-Dendra2 clearance assay experiment. An embryo ubiquitously expressing Squint-Dendra2 was imaged immediately prior to photoconversion and every 10 min after photoconversion as described in Text S5. Imaging began between dome and 30% epiboly stages (~5 hours post-fertilization). Left: red fluorescence from photoconverted Squint-Dendra2. Note the high-intensity extracellular fraction that appears immediately post-photoconversion and decays over time. Intracellular intensities also increase after photoconversion, but the majority of the protein appears to be localized extracellularly. In control experiments, we established that the focal plane stays constant and that slight changes in embryo diameter are likely due to tissue morphogenesis. Right: Alexa488-dextran was injected at the one-cell stage in order to label all cells. The Alexa488 signal was used to generate masks that define the extracellular space (fig. S13, Text S5). The average red extracellular intensity was determined in each image, and the time-dependent decay was fitted with an exponential function, yielding a half-life of 99 min for this embryo.